ANISOTROPIC BEHAVIOR OF THIN WALLED MEDICAL TUBES IN NICKEL-TITANIUM SUPERELASTIC SHAPE MEMORY ALLOYS

Estephanie Nobre Dantas Grassi

Communauté
UNIVERSITÉ Grenoble Alpes

THÈSE

Pour obtenir le grade de

DOCTEUR DE LA COMMUNAUTE UNIVERSITE GRENOBLE ALPES

Spécialité : 2MGE : Matériaux, Mécanique, Génie civil, Electrochimie

Arrêté ministériel : 25 mai 2016

Présentée par

Estephanie NOBRE DANTAS GRASSI

Thèse dirigée par **Denis FAVIER,** Professeur, UGA, et
codirigée par **Grégory CHAGNON,** Maitre de Conférences, UGA

préparée au sein du **Laboratoire Techniques de L'Ingénierie Médicale et de la Complexité – Informatique, Mathématiques et Applications**

dans **l'École Doctorale I-MEP2 – Ingénierie – Matériaux, Mécanique, Environnement, Energétique, Procédés, Production.**

COMPORTEMENT ANISOTROPE DE TUBES MÉDICAUX À PAROI MINCE EN ALLIAGE À MEMOIRE DE FORME SUPERELASTIQUE DE NICKEL-TITANE

Anisotropic behaviour of thin walled medical tubes in Nickel-Titanium superelastic shape memory alloys

Thèse soutenue publiquement le **04 Octobre 2018** devant le jury composé de :

M., Gerard, RIO
Professeur, Université Bretagne Sud, Rapporteur
M., Yves, CHEMISKY
Professeur, Université de Bordeaux, Rapporteur
M., Hervé, LOUCHE
Professeur, Université Montpellier, Président de jury
M., Denis, FAVIER
Professeur, Université Grenoble Alpes, Directeur de thèse
M., Grégory, GHAGNON
Maître de conférences HDR, Université Grenoble Alpes, Co-Directeur de thèse

ANISOTROPIC BEHAVIOUR OF THIN WALLED MEDICAL TUBES IN NICKEL-TITANIUM SUPERELASTIC SHAPE MEMORY ALLOYS

Estephanie NOBRE DANTAS GRASSI

January 2, 2019

ACKNOWLEDGMENTS

First I want to thank the Brazilian National Council for Scientific and Technological Development (CNPq) for conceding me the scholarship to develop this thesis through the Ciência sem Fronteiras program. With this rich experience behind me, I hope to help my country see better days.

I wish to express my gratitude to my supervisors Denis Favier and Grégory Chagnon for the opportunity of developing this thesis in the BioMMat team. I have learned a lot with this work and I am very thankful to both of you for your availability, scientific guidance and personal advice.

I wish to thank Yves Chemisky and Gérard Rio for having accepted to be my rapporteurs. Thank you for your careful reading of my manuscript and for your valuable remarks and suggestions. Thanks also to Hervé Louche for accepting the role of president of the defense jury, as well as for your sympathy on the occasions when we have met during these years. I will also extend my gratitude to Professor Carlos de Araújo in Brazil who helped me pave the way to start this thesis.

I would also like to thank my fellow students and colleagues in the TIMC-IMAG laboratory for your warmth and companionship. To Chris, Quentin, Gabriel, François, Guilherme, Thierry, Nathanael, Ana, Ali, Anaïs, Mohammed, Khouloud, Helena, Armida, Ricardo, and others I may have forgotten to mention here. It was a real pleasure to have met you and shared these years with you. I want to say special thanks to Chris, for the countless times you've helped me and Henrique with scientific, bureaucratic, logistic assistance (list not exhaustive!); to Quentin, for your kindness, camaraderie and all my actual knowledge and experience in Savoyard culture; to Ali, for receiving us in your home and showing us your culture with such enthusiasm. Thank you all for your true friendship. Thanks also to Thierry for being so helpful with experimental issues, for introducing me to indoor climbing (I did not discover a talent but I discovered I love it!) and for your kindness. I will have to stop here before this gets too long but I wish you all know I feel lucky to have met you and you are in my best memories of these years.

My immense gratitude goes also to my family for having always supported me in ways I cannot put into words. I'll always remember mom saying "I'll cry when you're gone, but don't you dare let it stop you". I hope you know how thankful I am for having you all.

And last, thank you Henrique. We have shared all the ups and downs of this journey and I'm very, very grateful I had you along the way. I love you. You know how much.

RESUMÉ

Les tubes à paroi mince en alliage à mémoire de forme Nickel-Titane (AMF NiTi) sont largement utilisés dans la fabrication de stents auto-expansibles. Le fonctionnement des stents repose sur la superélasticité (SE), comme de nombreuses autres applications des AMF NiTi dans le domaine biomédical. Le SE est un phénomène cristallographique réversible qui donne aux AMF la capacité de récupérer de grandes déformations par simple déchargement mécanique. En raison de la nature cristallographique du SE, les propriétés mécaniques liées à cet effet devraient être affectées par l'anisotropie inhérente du tube, qui émerge de son processus de fabrication. Cependant, le NiTi est encore souvent considéré comme isotrope dans la conception et l'optimisation de tels dispositifs. L'une des difficultés empêchant l'utilisation de modèles anisotropes est l'absence de caractérisations mécanique de l'anisotropie du tube NiTi. Le présent travail vise à effectuer une telle caractérisation pour un tube superélastique NiTi à paroi mince. Dans une campagne expérimentale, le comportement en traction du tube est analysé à différentes orientations et températures. La technique de corrélation d'image numérique (digital image correlation - DIC) est utilisée pour surveiller la distribution des déformations pendant les essais de traction. Les résultats montrent que toutes les propriétés analysées liées à la SE sont anisotropes. Toutes les dépendances d'orientation sont presque symétriques par rapport à la direction 45° de l'axe du tube. Certaines propriétés dépendent également de la température, dépendance qui est également anisotrope. Une approche thermodynamique basée sur l'énergie libre de Gibbs est utilisée pour analyser ces dépendances d'orientation et de température. Avec cette analyse, il a été possible de relier l'hystérésis mécanique de la SE et les contributions irréversibles présentes dans le système. Enfin, l'influence de l'anisotropie sur la distribution des déformations est analysée. L'accent est mis sur l'analyse du phénomène de localisation de la déformation tout au long du chargement et du déchargement. L'inclinaison de la bande de localisation est caractérisée et évaluée avec une approche de plasticité. L'angle de la bande avant observé avec DIC est prédit en utilisant des données de vitesse de déformation données de vitesse de déformation calculées à partir des courbes contrainte-déformation.

Mots-clés: alliages à mémoire de forme, superélasticité, tube Nickel-Titane, anisotropie, comportement en traction.

ABSTRACT

Thin walled tubes of Nickel-Titanium shape memory alloys (NiTi SMA) are widely used in the fabrication of self-expandable stents. The operation of stents relies on the superelastic effect (SE), as many other applications of NiTi SMA in the biomedical field. The SE is a reversible crystallographic phenomenon that gives SMA the ability to recover large strains through simple unload. Due to the crystallographic nature of the SE, the mechanical properties related to this effect are expected to be affected by the inherent anisotropy of the tube, which emerges from its fabrication process. However, NiTi is still often treated as isotropic in the design and optimization of such devices. One of the difficulties preventing the use of anisotropic models is a lack of mechanical characterizations about the NiTi tube anisotropy. The present work aims to perform such characterization for a thin walled NiTi superelastic tube. In an experimental campaign, the tensile behaviour of the tube is analysed at different orientations and temperatures. Digital Image Correlation (DIC) technique is used to monitor the strain distribution during tensile tests. Results show that all the analysed properties related with SE are anisotropic. All the orientation dependencies are nearly symmetrical with respect to 45° from the tube axis. Some properties are also dependent on temperature, a dependence that is also anisotropic. A thermodynamic approach based on the Gibbs free energy is used to analyse these orientation and temperature dependencies. With this analysis it was possible to relate the SE stress hysteresis and thermodynamic irreversible energy contributions. Finally, the influence of anisotropy on the strain distribution of tensile samples is verified. Focus is given to the analysis of the strain localization phenomenon throughout loading and unloading. The inclination of the localization front band is characterized and evaluated with a plasticity approach. The front angle observed with DIC is predicted using strain rate data calculated from stress-strain curves.

Keywords: shape memory alloys, superelasticity, Nickel-Titanium tube, anisotropy, tensile behaviour.

CONTENTS

LIST OF FIGURES

LIST OF TABLES

GENERAL INTRODUCTION

Shape Memory Alloys (SMA) have a unique thermomechanical behaviour due to a reversible martensitic phase transformation. One of the manifestations of this crystallographic phenomenon is the **superelastic** effect, in which large deformations are recovered by simple mechanical unload. This behaviour greatly differs from that of usual metallic alloys, whose range of reversible strain is 40 times smaller. Among other exceptional properties, this high added functional value justifies the use of SMA in many applications, despite their higher cost.

SMA applications are disseminated in areas as diverse as aeronautics, automotive, robotics and biomedical engineering. In many of these applications focus is given to **Nickel-Titanium** alloys (NiTi). This alloy particularly fulfils the biocompatibility requirements for biomedical applications.

One of the most successful applications of NiTi SMA in the biomedical field are self-expandable stents, which are mainly manufactured from NiTi **thin walled medical tubes**. These tubes are obtained from a succession of thermomechanical operations involving great amounts of cold working. This processing makes the material highly textured, ultimately causing a strong **anisotropic behaviour**.

Nevertheless, the material is still often treated as isotropic in the design and modelling of devices. This choice is either made as a simplification or for unfamiliarity with the orientation dependence of its properties. In certain circumstances, however, such a choice can be an oversimplification and has critical consequences.

The influence of anisotropy can be illustrated in the case of the fabrication process of NiTi self-expandable stents. This device can either be manufactured from tubes with a small diameter or from tubes with a diameter near the final desired dimension of the stent (Favier et al., 2006; Poncin and Proft, 2003), as shown in Fig. 1. In the first manufacturing route, the struts of the stent are cut aligned with the drawing direction of the tube, in a so called "closed configuration". The final dimension is then achieved through a shape setting with multiple steps. In the second manufacturing route the struts of the stent are cut oriented at an orientation θ from the drawing direction, in an "opened configuration". Both manufacturing routes lead to stents with identical geometries. However, due to the anisotropy of the tube, these stents have different thermomechanical behaviours because of the different alignments of the struts immediately after the cutting step. In order to better control the mechanical behaviour of the stent — and of any device manufactured from anisotropic NiTi alloys — the orientation dependence of the material must be understood. Otherwise, progress on design and optimization stays limited.

In SMA, all phenomena related with phase transformation might be affected by

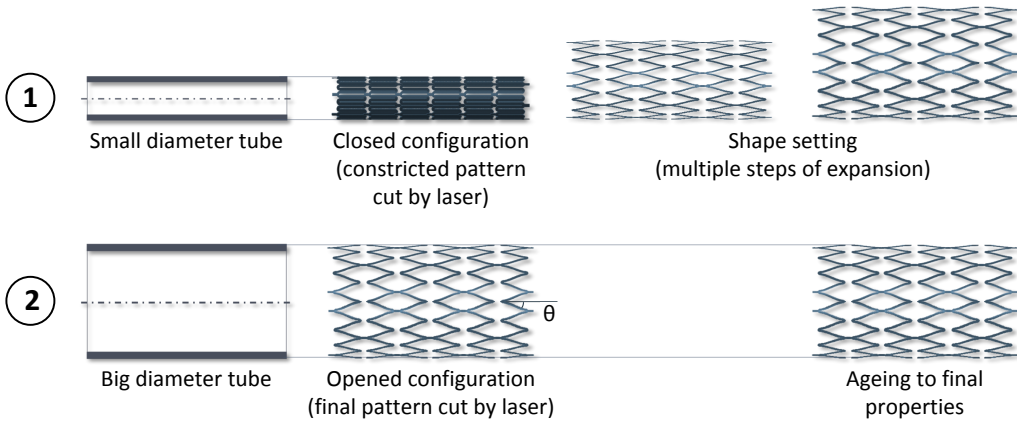

Figure 1: Two possibilities of manufacturing processes of self expandable stents (Adapted from Favier et al., 2006).

the existence of a texture. This includes transformation strain and stress, Clausius-Clapeyron coefficient and mechanical hysteresis, as well as the strain distribution in NiTi SMA, which generally experience localization phenomenon under tension. This knowledge can be implemented in simulations and help to optimize and even tailor the mechanical behaviour of a desired device.

In this context, the general objective of this thesis is to characterize and analyse the anisotropic mechanical behaviour of a NiTi SMA, particularly of medical superelastic NiTi thin walled tubes. To that end, an experimental characterization was carried out. It consisted in producing oriented tensile samples from the flattened tube and monitoring their tensile behaviour using Digital Image Correlation (DIC). Samples at different orientations were tested at different temperatures, so that the temperature dependence (or lack thereof) could be studied. Thus, this manuscript is organized in four main chapters.

Chapter one aims to present a bibliography on NiTi SMA behaviour to prepare the reader for the subsequent chapters. Starting with generalities, it introduces main properties, the superelasticity and the shape memory effect, as well as some NiTi medical applications. Then, the chapter presents a state of the art about experimental observations of anisotropic behaviour and strain localization in NiTi alloys. The final part of this chapter presents the theoretical approaches often used for modelling the thermodynamic behaviour and localization phenomenon in NiTi SMA.

Chapter two explains all the experimental aspects of the work. It presents the details of the experimental campaign and justifies the choices made regarding the sample preparation and experiments.

Chapter three analyses the global tensile behaviour of the oriented samples. It discusses the anisotropy influence on important SMA properties. Through a thermodynamic analysis based on the approach discussed in the first chapter, thermodynamic properties and its dependence on orientation are quantified. The temperature dependence of the anisotropic behaviour is then analysed. This chapter is written in the form of a journal article. Because of that it contains brief descriptions of the experimental campaign and the thermodynamic approach.

Chapter four explores how the tube anisotropy affects the strain localization phenomenon of the NiTi alloy, monitored with DIC technique during tensile test. The ori-

entation dependence of the transformation band angle from the tube drawing direction is analysed. The evolution of the band angle throughout loading and unloading is also examined. A plasticity theory (Hill, 1948, 1952) is then used to predict the orientation dependence of the band angle.

CHAPTER

ONE

BIBLIOGRAPHY ON NiTi SMA BEHAVIOUR

Contents

1.1 Introduction

This chapter aims to give the context for the thesis work and for the analyses that will be performed in subsequent chapters. It presents a state of the art about relevant experimental observations, as well as introduces the theories that will give support to the discussion of results.

The chapter is divided in three main parts:

- Section 1.2 presents thermomechanical aspects of Shape Memory Alloys (SMA), their main properties and phenomenology. Focus is given to the NiTi alloy family, which is widely used on industrial scale, mainly in the fabrication of medical devices. This first part ends with an overview of the most consolidated medical applications of NiTi SMA.

- A state of the art about measurements concerning anisotropy (Section 1.3) and strain localization (Section 1.4). In Section 1.3, both crystallographic and mechanical aspects are discussed. Literature reports are reviewed, firstly for single crystals and then for polycrystalline NiTi alloys. The repercussions on mechanical behaviour are discussed for both cases. Section 1.4 starts presenting the phenomenological conditions for the occurrence of localization in SMA. Experimental observations are then discussed and the section ends with a synthesis of the techniques that have been used to observe and measure the phenomenon.

- An introduction to the theoretical approaches used in the analyses of results of the third and fourth chapters. Starting with the thermodynamics of phase transformation in Section 1.5, the material is considered as a thermodynamic system and the equations for the phase transformation are developed. Lastly, Section 1.6

examines the mechanics of strain localization described by plasticity theory. In particular, the theories for Lüders deformation mode (LDM) and localized necking are discussed, which are the ones generally applied for the analysis of localization in NiTi SMA.

1.2 Shape Memory Alloys

Shape Memory Alloys are a distinct class of active materials that respond to thermo-mechanical stimuli by recovering their shape, even under high applied loads. This phenomenon happens due to a thermoelastic martensitic transformation between two solid metallic phases: austenite and martensite. The microstructure transition that relates both crystallographic phases is a diffusionless phenomenon. It is, therefore, reversible due to its shear distortion nature, where atoms merely move from their original positions through a twinning mechanism.

Austenite, martensite and the thermoelastic martensitic transformation

The phase transformation can be triggered either by thermal or mechanical energy. Thus, the behaviour of SMA is dependent on the relation between temperature, stress and strain. Figure 1.1 shows schematically the crystallographic interactions of austenite and martensite phases in three Cartesian axes expressing temperature, uniaxial tensile stress and strain.

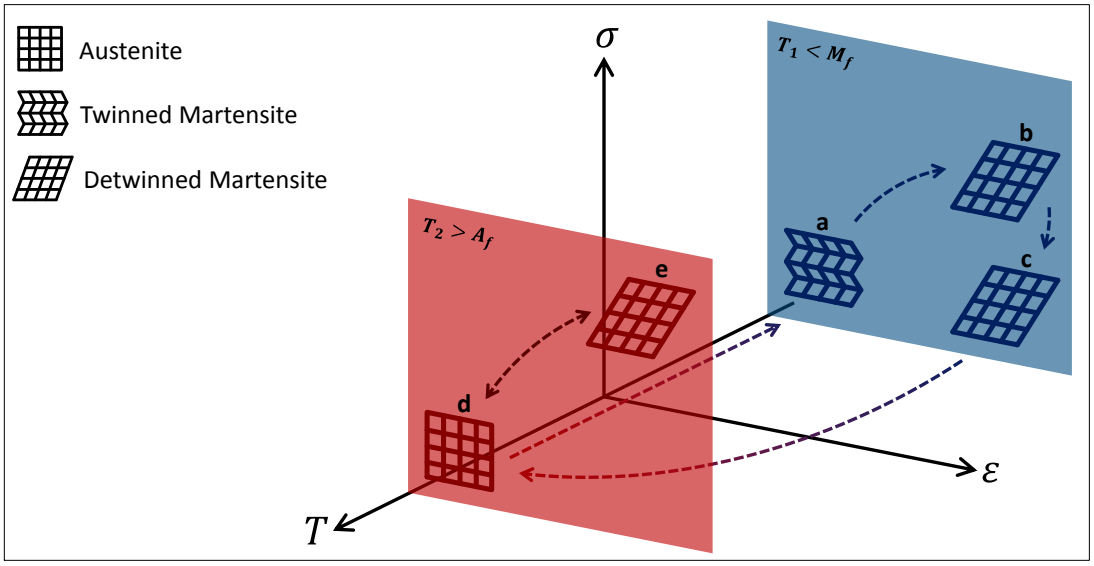

Figure 1.1: Temperature (T) - stress (σ) - strain (ε) space showing the regions where austenite and martensite phases are stable.

When subjected to a temperature variation in the absence of stress, the SMA experiences a thermally induced phase transformation. It occurs between austenite and a twinned martensite phase (also called self-accommodated). This is illustrated in Fig.

1.1 between points d and a, respectively. In this case, no macroscopical shape change is perceived.

When a tensile stress/strain is involved in the transformation, another type of martensite oocurs: a detwinned martensite, aligned with the stress/strain main axis. According to Fig. 1.1, austenite is stable at high temperatures/low stresses. Martensite is stable at low temperatures and at high temperatures/high stresses.

The notion of high and low temperature is relative to the temperature range whose limits mark the start and finish of the thermally induced phase transformation. They are M_s and M_f for start and finish of forward transformation (Austenite → Martensite), and A_s and A_f for start and finish of reverse transformation (Martensite → Austenite). Thus, martensite is stable at temperatures lower than M_f in the absence of stress. Austenite, in turn, is stable when the alloy is both above A_f and at low stresses.

Superelasticity and Shape Memory Effect

It is the shape change associated with the application of a mechanical loading that motivates interest in SMA. Two thermomechanical behaviours are particularly interesting for engineering applications: the Shape Memory Effect (SME) and the Superelasticity (SE).

If the SMA is mechanically loaded in the austenitic state (T > A_f) the **Superelasticity** takes place. In this situation the cubic crystals transform directly into detwinned martensite through a stress induced martensitic transformation (SIMT). Because the material is already above A_f, where austenite is stable under low stress, the simple unloading ensures the total recovery of deformation, with no need for heating. In Figure 1.1 a complete superelastic cycle occurs in the sequence *d-e-d*. Figure 1.2a shows schematically a typical superelastic tensile stress-strain curve.

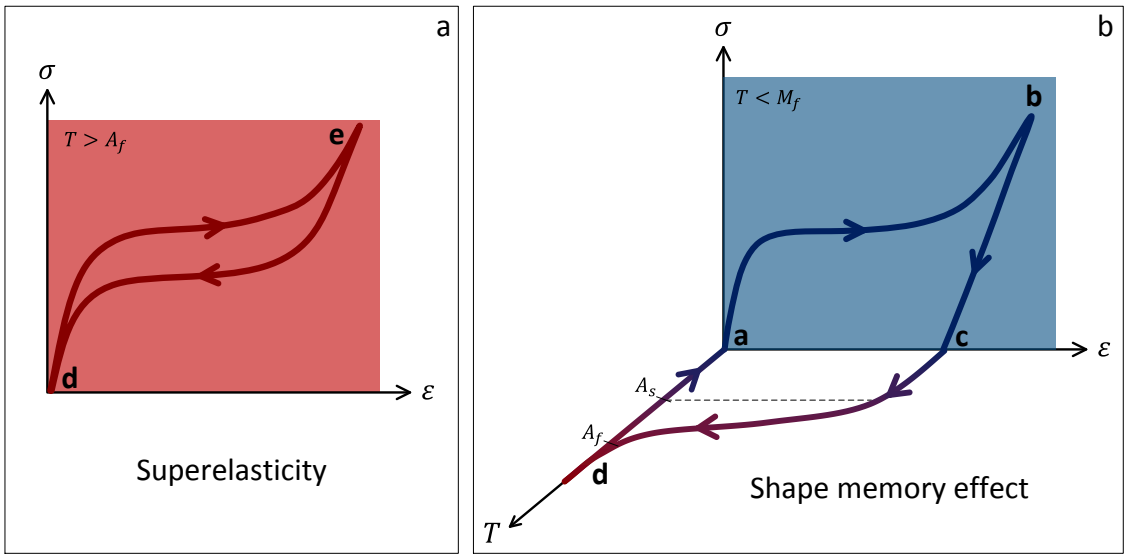

Figure 1.2: Typical thermomechanical tensile behaviour during SMA (a) a superelasticity cycle (also *d-e-d* in Fig. 1.1) and (b) a shape memory effect cycle (also *a-b-c-d-a* in Fig. 1.1).

On the other hand, if the SMA is mechanically loaded in the martensite state the self-accommodated structure becomes oriented (detwinning process, from a to b in Fig.

1.1), which requires lower stress levels compared to the SIMT. When the mechanical load is released, the crystallographic structure preserves the oriented configuration and hence the macroscopic deformation (from b to c in Fig. 1.1). At this point, when the material is heated above A_f, the martensite crystals transform into austenite and the macroscopic deformation is recovered (from c to d in Fig. 1.1). This phenomenon is called **Shape Memory Effect**. A typical SME tensile stress-strain behaviour is illustrated in Figure 1.2b.

Any mechanical loading between M_f and A_f will result in a mixed behaviour between SME and SE. The residual deformation is partially recovered by unloading and partially recovered by subsequent heating above A_f. If deformed at a high enough temperature the alloy experiments slip and some permanent deformation occurs after unloading (Miyazaki et al., 1982; Otsuka and Wayman, 1998).

1.2.1 Thermomechanical characterization

In the absence of mechanical load

From a practical point of view, the most important characteristic of SMA are their phase **transformation temperatures**. They define the regions in the temperature-stress-strain space where the SME and SE take place.

These temperatures are generally defined during a phase transformation in the absence of mechanical loading, through a temperature sweep. The most popular technique used is Differential Scanning Calorimetry (DSC), which measures the heat released and absorbed during the forward and reverse transformations, respectively. Figure 1.3 shows schematically a DSC result.

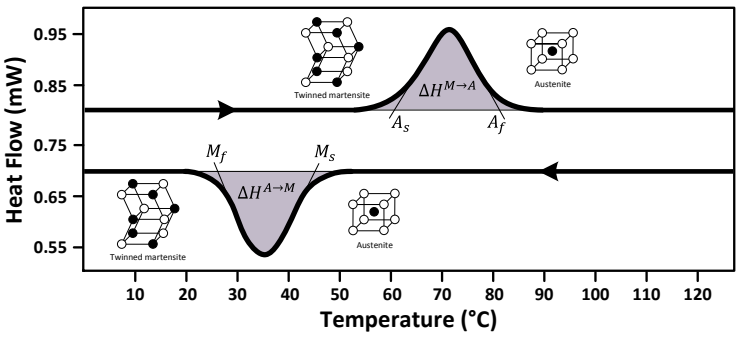

Figure 1.3: Scheme of differential scanning calorimetry (DSC) of a NiTi alloy using tangent lines for the extraction of phase transformation temperatures (adapted from Lagoudas, 2008).

The principle of this technique is that in order to maintain a constant temperature rate during the temperature sweep, the heat flow has to be adjusted during a phase transformation. Hence, heat flow peaks are measured. The area inside the peaks are equivalent to the amount of heat released or absorbed in each transformation, equivalent to the enthalpy variation ΔH between phases. Then, the start and finish transformation temperatures are defined using tangent lines between peaks and baselines.

There are other material properties that present measurable variations during a SMA phase transformation. The electric resistance is one example and is also used to identify transformation temperatures (Brill et al., 1991; Kato and Sasaki, 2013; Miyazaki and Otsuka, 1986). The storage modulus, whose variation can be measured during a Dynamic Mechanical Analysis (DMA), is another example (Alonso, 2015; Zhang et al., 2005).

In the presence of mechanical load

The transformation properties that matter the most for the superelasticity are the phase **transformation stresses**. Analogously to the transformation temperatures, there are four transformation stresses: σ^{M_s} and σ^{M_f} for start and finish of forward transformation (Austenite $\rightarrow$ Martensite); σ^{A_s} and σ^{A_f} for start and finish of reverse transformation (Martensite $\rightarrow$ Austenite).

They are usually determined by tracing tangent lines over the superelastic curve, as demonstrated in Fig. 1.4a. This figure also shows schematically the relation between these transformation stresses and temperature. There is a linear dependence, which is defined by the Clausius-Clapeyron equation (more details in section 1.5).

The **Clausius-Clapeyron coefficient** is another important property for engineering applications of superelastic SMA. Figure 1.4b shows schematically the role played by the Clausius-Clapeyron coefficient $C^{A\rightarrow M}$ on the conditions for SE and SME to happen. The line with positive slope represents the linear relation between σ^{M_s} and temperature. This slope is the Clausius-Clapeyron coefficient for the start of the forward transformation.

As explained by Otsuka and Wayman (1998), the SME takes place below A_s with subsequent heating above A_f. SE occurs without the need of temperature variation, at temperatures above A_f. Between A_s and A_f both SME and SE occur partially. The line with negative slope mark the critical stress for slip, above which permanent deformation occurs. M_d is the critical temperature from which plastic deformation occurs before the SIMT (Miyazaki et al., 1981; Shaw and Kyriakides, 1995).

1.2.2 NiTi alloys

Among the most promising SMA compositions, NiTi is the one presenting the most favourable conditions for engineering applications and industrial scale production. These conditions include high specific actuation density (Lagoudas, 2008) and thermomechanical properties that are stable over time. For that reason the majority of researches concerning SMA behaviour focus on NiTi based alloys.

NiTi balance

The shape memory NiTi alloys only exist near the equiatomic compositions. The **amount of Ni** in the matrix is determinant for the phase transformation temperatures. The more Ni in the composition, the lower the phase transformation temperatures. For example, while the equiatomic alloy (Ti-50at.%Ni) presents an $A_f = 120°C$, a Ti-51at.%Ni alloy presents an $A_f = -40°C$ (Otsuka and Wayman, 1998).

Ni-rich alloys (with Ni composition above 50% at.) are sensitive to ageing treatments (Otsuka and Wayman, 1998), allowing to adjust their thermomechanical properties after manufacturing. The excess of Ni in the stoichiometric composition favours the forma-

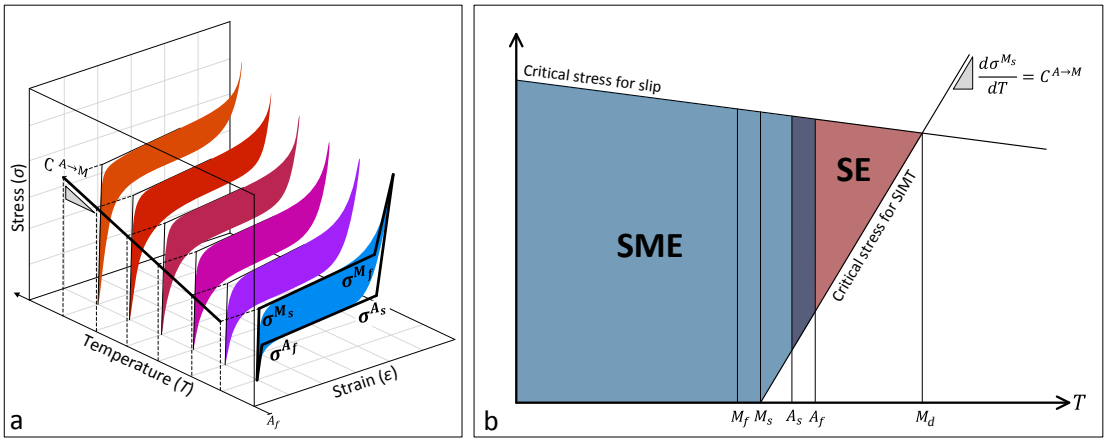

Figure 1.4: (a) Example of extraction of phase transformation stresses from superelastic curve and schematic dependence on temperature of superelastic behaviour. (b) Role played by Clausius-Clapeyron coefficient ($C^{A\rightarrow M}$), transformation temperatures and critical slip stress on the conditions for existence of superelasticity (SE) and shape memory effect (SME) (adapted from Otsuka and Shimizu, 1986).

tion of **Ni-rich precipitates** during heat treatment. The precipitates do not transform, and thus do not contribute to the SMA effects, but they change the NiTi ratio, which consequently affects the transformation temperatures (Dennis and Tu, 2008).

Crystallographic structure and the R-phase

In NiTi alloys the austenite phase is body-centered cubic and is also referred to as B2 phase. Martensite is monoclinic and also referred to as B19'. A triclinic metastable martensite phase also occurs, known as the R-phase. It occurs as an intermediate transformation between Austenite ↔ Martensite transformations. Figure 1.5 shows examples of the presence of R-phase transformation.

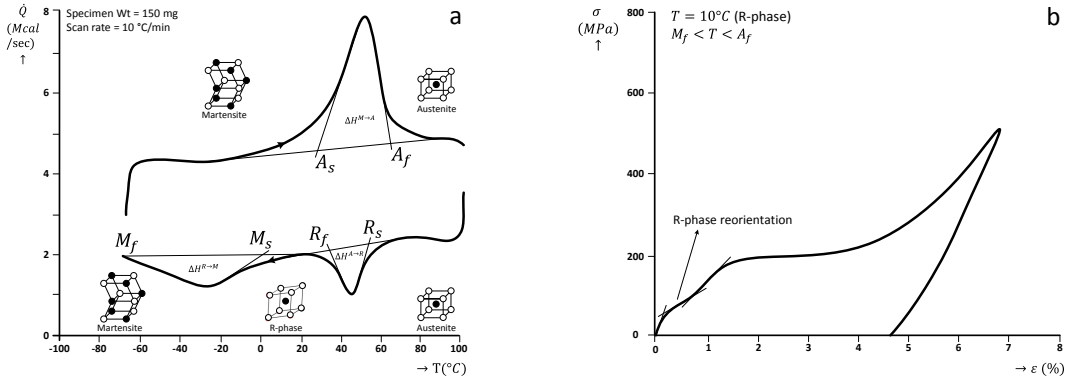

Figure 1.5: (a) DSC thermogram of a NiTi alloy with a very distinguishable R-phase peak during cooling. (b) Mechanical response of the NiTi alloy when the R-phase is the the starting microstructure and its reorientation takes place. (adapted from Shaw and Kyriakides, 1995)

Figure 1.5a shows a DSC result where the R-phase presence is recognizable either by

the small temperature hysteresis, which can be as small as 1.5°C (Duerig et al., 1990), and by the enthalpy variation, which is typically smaller than 6 J/g (Reedlunn et al., 2014; Schlosser, 2008). The direct phase transformation between martensite and austenite in NiTi alloys has temperature hysteresis ranging between 25°C and 40°C (Stoeckel, 1995) and enthalpy variation around from 19-32 J/g (Meschel et al., 2011; Otubo et al., 2008).

Figure 1.5b shows a typical tensile stress-strain curve with the R-phase being the starting microstructure. In this case, R-phase reorientation happens prior to B19' martensite reorientation, causing a macroscopic deformation of about 1% in tension (Duerig et al., 1990; Šittner et al., 2006).

The occurrence of the R-phase is related to certain conditions such as high Ni content, annealing at low temperature immediately after cold work and thermal cycling (Miyazaki and Otsuka, 1986). On the other hand, it generally vanishes after heat treatments at high temperatures (Lagoudas, 2008). The NiTi alloy can experience a certain number of types of transformation involving these three phases. The starting and resulting phases will depend on the alloy transformation temperatures and on its thermomechanical loading history.

Thermomechanical processing: shape setting

The manufacturing process of NiTi superelastic devices very often includes a step called **shape setting**. It consists of a heat treatment under mechanical confinement whose objective is to create a new desired shape (create a coil spring from a wire, for example) or to change the original dimensions.

The shape setting parameters (temperature and time) are chosen so that minimum changes in the original thermomechanical behaviour occur. For effective shape settings in Ni-rich SMA compositions, it has been shown that temperatures should be chosen around 450-550°C with durations of the order of 10 minutes (Liu et al., 2008). Moreover, it has been shown that shape settings only provoke minor differences between as-received and shape set materials. The reported differences in the alloy transient response, transformation strain and unrecovered strain are very small (Benafan et al., 2013).

1.2.3 Suitability for medical applications

NiTi SMA are very suitable for biomedical applications due to their mechanical behaviour and biocompatibility. Compared to classic metals like stainless steel, NiTi SMA mechanical behaviour is a lot closer to human body tissues and organs, which avoids overstraining of the treated zone (see Fig. 1.6).

Its **biocompatibility**, i.e. its capacity to remain non toxic while in direct contact with human tissues, has been proved (Ryhänen et al., 1997, 1998). Although nickel itself is toxic to the human body, titanium is not. In order to avoid Ni toxicity, NiTi alloys are coated with Ti components like TiO_2, which increases corrosion resistance and preserves biocompatibility (Aun et al., 2016a,b; Huang et al., 2014). Other coatings such as TiN or TiCN are also good in improving NiTi corrosion resistance (Lagoudas, 2008). Furthermore, NiTi implants are easily detected by Magnetic Resonance Imaging (MRI), providing clear crisp images which facilitates the device monitoring (Duerig et al., 1999).

However, if NiTi SMA are popular in medical applications it is undoubtedly due to the superelasticity and shape memory effect. The superelasticity is a valuable feature

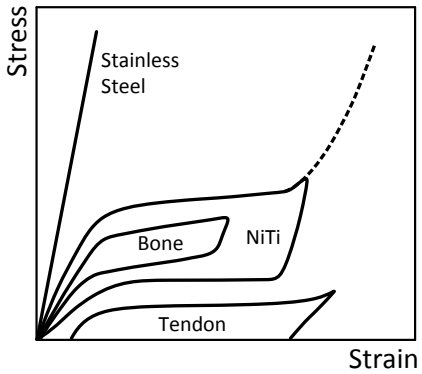

Figure 1.6: Comparison of mechanical behaviour of NiTi, stainless steel and human tissues. (Jani et al., 2014)

during medical treatment because its thermomechanical behaviour approaches that of human tissues. The stress plateau implies the application of a nearly constant force in a large deformation range. This means that the implant will not deform plastically and will be able to maintain its form and strength throughout the treatment. It is also an advantage that the level of force applied during the stress plateau can be designed to match the tissue stiffness, so that the implant will not damage the tissue with excessive strength. The shape memory effect, when employed, is mostly used in the implantation of the device. In this case, the alloy is tailored so that its A_f is slightly above room temperature and below the body temperature.

One of the most successful superelastic implants are the self-expanding **stents** (Fig. 1.7). These structures treat obstructions in the transport of body fluids. They are tubular meshes placed inside cylindrical passages such as the oesophagus, biliary duct and most importantly blood vessels. Stents act as scaffolds, pushing against the internal walls of the conduit or vessel to re-open the obstructed area. They are also implanted with the aid of a catheter, however making use of the superelasticity. They typically expand 3 to 8 times the catheter diameter upon the catheter releasing (Duerig et al., 1999). They are manufactured mainly from tubes cut through laser and are a very good

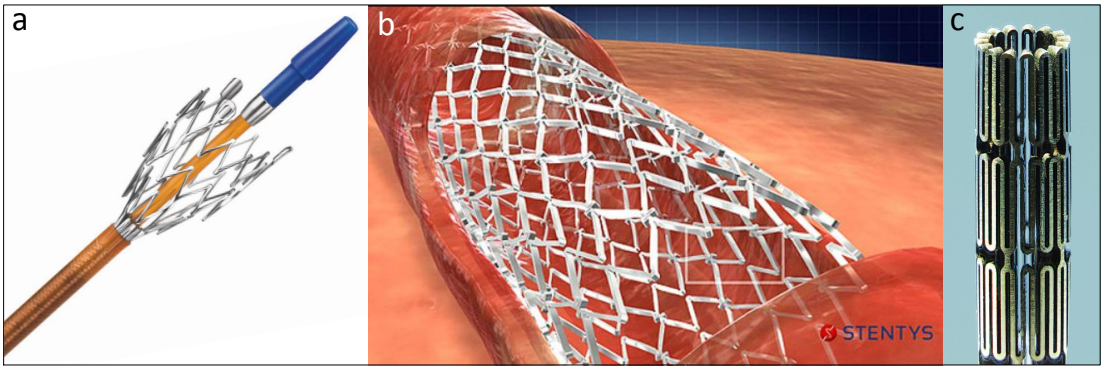

Figure 1.7: Examples of NiTi superelastic stents: (a) U-flex model from Andramed, (b) Stentys model from the homologous company, (c) a small diameter stent cut with Sigma Femtosecond Laser Tube cutting system from Miyachi America Corporation.

example of how medical and engineering applications of SMA can still evolve together with manufacturing technologies.

1.3 Experimental observations of anisotropy in NiTi SMA

Anisotropic materials behave differently when loaded in different directions. In metallic alloys, this condition is primarily caused by crystallographic texture (Sowerby and Johnson, 1975), mainly as result of manufacturing processes in polycrystalline materials. Because of that cause-and-effect relationship, many anisotropy investigations rely on texture analyses. The basics of crystallographic texture and its representation are explained in Appendix A.

The global behaviour of polycrystalline alloys approaches the behaviour of single crystals oriented in the dominant texture. In this manner, the local deformation mechanisms occurring in single crystals is very helpful to the understanding of the behaviour in textured polycrystalline alloys. Taking this into account, this section is divided in two parts: single crystals and polycrystalline NiTi.

1.3.1 Single crystals

Studies concerning the anisotropy of NiTi single crystals generally consist in experimenting in the ⟨100⟩, ⟨110⟩ and ⟨111⟩ cubic crystal family directions. These directions are illustrated in Fig. 1.8. Then, the differences of mechanical behaviour between these orientations are discussed. The discussions are presented regarding both global mechanical behaviour, related with stress-strain curves, and local behaviour, with microscope observations.

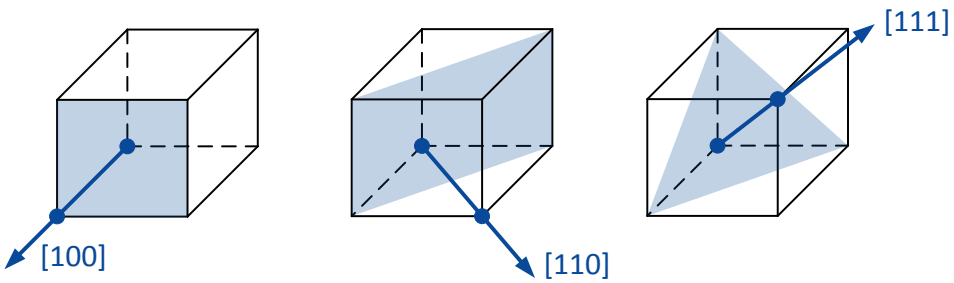

Figure 1.8: Main directions in the cubic crystallographic system.

1.3.1.1 Orientation dependence of global mechanical behaviour

It has been shown that the tensile **stress-strain curves** of NiTi single crystals differ significantly when loaded along its [111], [110] or [100] direction. Under tension, Gall et al. (1999) showed that in a Ti-50.8at.%Ni alloy under tension the [100] orientation has a much smaller recoverable strain compared to [110] and [111] (see Fig. 1.9). In

the [100] direction the transformation starts at a higher stress level and with significant hardening and brittle fracture when excessively loaded. On the other hand, [110] and [111] directions start to transform at lower stress levels and the transformation was accompanied by a distinct stress plateau.

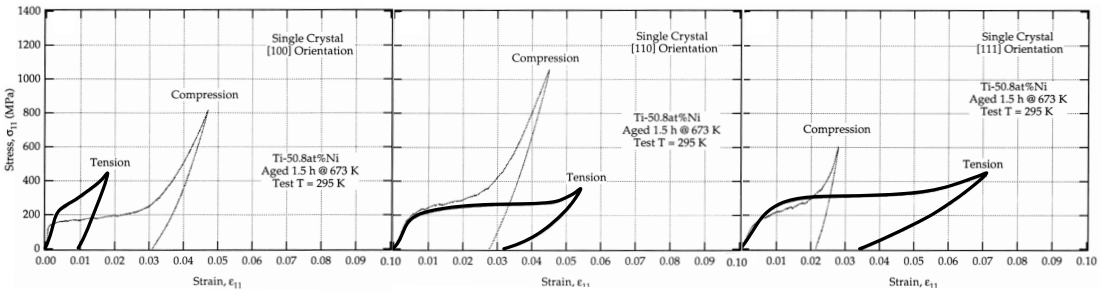

Figure 1.9: Uniaxial behavior of NiTi [100], [110], and [111] NiTi single crystals (From Gall et al., 1999).

Because of their distinct tension behaviour, in the literature the [100] direction is sometimes referred to as "hard" and [111] as "soft". The behaviour of [110] is somewhat between both, but with a behaviour closer to the softer one.

The overall compression behaviour was somewhat opposite to the observed under tension. The crystals oriented at [100] showed low transformation stress level, stress plateau and large recoverable strain. Meanwhile, the crystals at [110] and [111] show more hardening and smaller recoverable strains compared to tension.

1.3.1.2 Orientation dependence of recoverable strain

Miyazaki et al. (1984) was one of the first to show that total recoverable strain is not equal the plateau strain (Lüders strain) in tensile tests of NiTi alloys. Using Fig. 1.10 as example, the authors show that tensile strain totally recovers upon heating if the specimen is strained until the end of stage II.

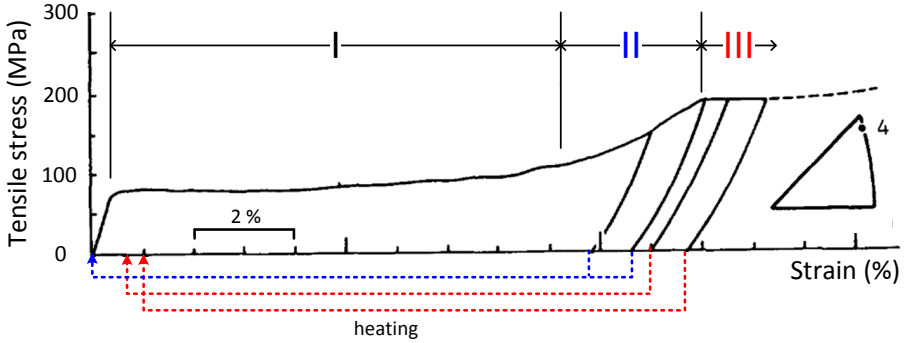

Figure 1.10: Example of stress-strain curve from a NiTi single crystal. The recoverable strain is measured after upon heating after straining the specimen by the end of stage II ((Miyazaki et al., 1984)).

This method was used to measure the recoverable strain in Ti - 50.5 at.% Ni single crystals submitted to tensile tests in seven orientations. These measurements were

compared with recoverable strain values calculated from phenomenological theory. Figure 1.11 shows in the inverse pole figure the orientation dependence map of recoverable strain.

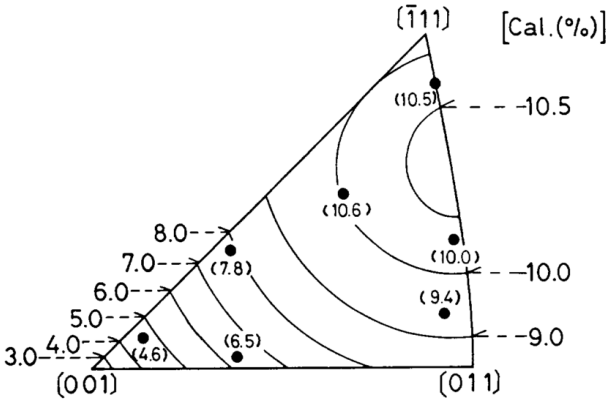

Figure 1.11: Inverse pole figure showing the orientation dependence of the recoverable strain of solution-treated single crystals (parenthesis) and calculated values (contour lines) (From Miyazaki et al., 1984).

As it can be seen, the maximum recoverable strains are achieved by crystals in the $\langle\bar{1}11\rangle_{B2}$ directions, while the minimum strains are achieved by the $\langle 001\rangle_{B2}$ directions. The values in the $\langle 011\rangle_{B2}$ direction are intermediate between the two extremes, but are indeed closer to $\langle\bar{1}11\rangle_{B2}$.

1.3.1.3 Influence of precipitates on orientation dependence of recoverable strain

Another important analysis performed in both aforementioned works was the influence of precipitates on recoverable strain orientation dependence. The presence of coherent or semi-coherent Ni-rich precipitates in a single crystal of a given direction can significantly change its mechanical response. Gall et al. (1999), Gall et al. (1998) and Miyazaki et al. (1984) observed and studied the mechanical behaviour of NiTi single crystals submitted to solution heat treatment (resulting in the absence of precipitates) and ageing heat treatment (resulting in the presence of precipitates). These precipitates do not undergo phase transformation and inhibit detwinning, therefore not contributing to the measured transformation strain. The overall observation is that the presence of precipitates decreases the orientation dependence of the critical transformation stress and strains.

Figure 1.12 shows the theoretical and measured recoverable strains from solutionized and aged single crystals by Miyazaki et al. (1984). The theoretical values are calculated from a phenomenological theory including detwinning strain and thus account for the maximum theoretical recoverable strain.

Confronting these results it was concluded that the precipitates resistance to transformation in the aged material leaves behind untransformed zones, consequently reducing the recoverable strain. The solution treated specimens, however, reach strain values that are very close to the theoretical ones, suggesting that the material fully transformed. Hence, the presence of precipitates reduced the orientation dependence of the recoverable strain due to incomplete transformation.

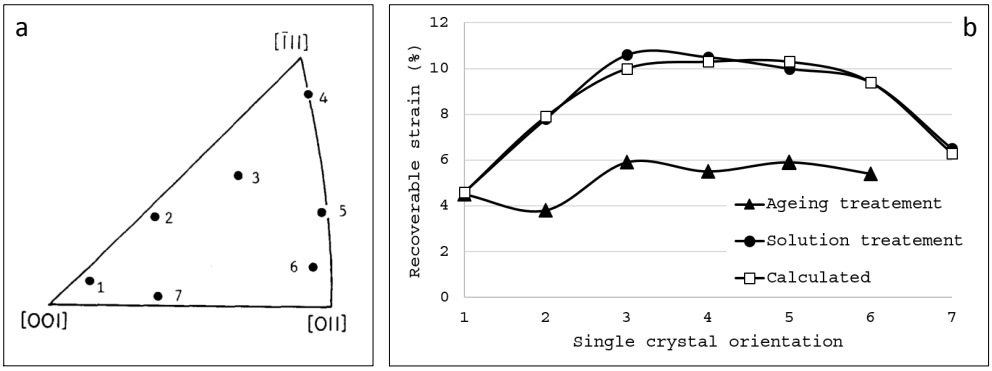

Figure 1.12: (a) Single crystal tension orientations studied by Miyazaki et al. (1984). (b) Comparison of measured recoverable strains from solution and aged treated materials with maximum strain values calculated from phenomenological theory (Plotted with data from Miyazaki et al., 1984).

1.3.1.4 Orientation dependence of microscopic deformation mechanism

The local behaviour and deformation mechanisms of [100] and [111] directions under tension were studied by Creuziger et al. (2008). The single crystal tensile samples were monitored by an optical metallurgical microscope with differential interference contrast microscopy. With this technique, any change in the sample surface tilt appears as a change in the surface color, and thus phase transformation is detected from the austenite polished surface.

Figure 1.13 shows micrographs of the samples before, during and after tensile loading. The structural differences between the surface of samples in both directions was already evident prior to loading. The surface of the [100] orientation was very uneven compared to [111] sample surface.

With subsequent loading, both orientations showed very distinct transformational behaviours. The rougher surface of the [100] crystal was intensified upon loading, while in the smoother [111] surface martensite bands grew into the austenite phase, along with a strain localization band (see Fig. 1.13b for both [100] and [111]).

Uniaxial notched dogbone samples were also observed for fracture observation. In these samples the transformational and fracture behaviours were also very different for both directions. In the notched [100] sample transformation distinctly started on the notch tip and propagated perpendicularly through the material. With further loading, cracks started on the notch tip and grew in the notch direction in a stable manner with minor crack kinking. In the [111] notched crystal a transformation zone only became distinct after substantial loading. This zone propagated from the notch tip in a direction around 25° from the notch direction in an almost symmetrical manner. The crack grew from the notch tip with substantial kinking and in an unstable fashion (see Fig. 1.13e for both [100] and [111]).

Creuziger et al. (2008) rationalise this difference in the crack propagation from an energy point of view. While in the [111] sample the transformation evolves mainly in the direction of the crack growth, providing more energy to its propagation, in the [100] sample the transformation occurs far from the crack growth path and some of the energy is dissipated.

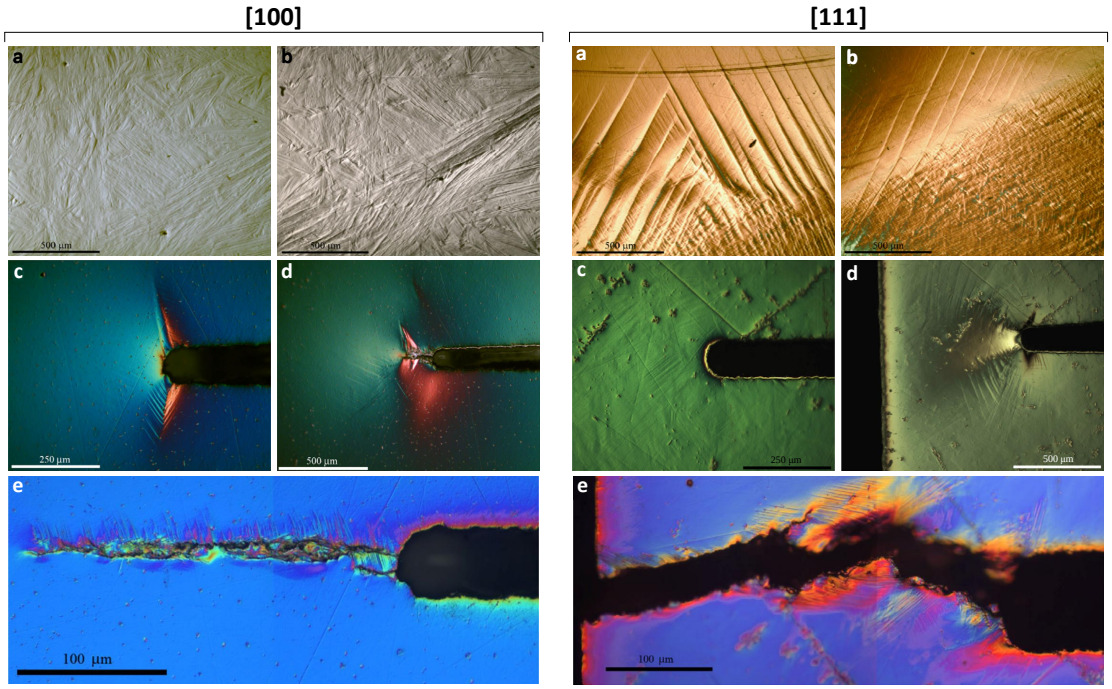

Figure 1.13: [100] orientation: (a) Surface of unloaded crystal. (b) Crystal during phase transformation, loaded at 920 N. (c) Notched sample with transforming zone perpendicular to the notch direction. (d) Notched sample with stable propagating crack. (e) Crack in the notched sample. [111] orientation: (a) Loaded crystal showing martensite bands propagating on the smooth austenite surface. (b) Transformation propagating in the form of a Lüders band. (c) Notched sample loaded at 127 N showing micro transformed zones ahead of notch tip in the form of small strips. (d) Transformed zone ahead of notch tip immediately prior to crack appearance. (e) Crack in the notched sample. (adapted from Creuziger et al., 2008).

1.3.2 Polycrystalline NiTi

Texture in polycrystalline alloys is created during metal forming processes such as drawing and rolling. An intuitive and correct assumption is that the **amount of plastic deformation** imposed in the manufacturing process is one key factor in the texture creation. Because NiTi alloys are often used for the fabrication of devices that have small dimensions, thin walled tubes, small diameter wires and thin plates are needed, causing polycrystalline NiTi alloys to be very textured.

Robertson et al. (2006) investigated the resulting texture of various NiTi **product forms**. The authors tested NiTi tubes, sheets and rods with different diameters and observed that all forms have very distinct textures, even rods with different diameters (16 mm and 41 mm). These different textures cause different types of anisotropic behaviour. Furthermore, the authors investigated the influence of heat treatments on the resulting texture of all forms. They have found out that the heat treatments not only do not erase the pre-existing texture, but intensify it. Other works show this same relation between texture and heat treatments. (Adharapurapu et al., 2010; Inoue et al., 1996). These results show that texture is indeed created during the early stages of manufacturing processes.

1.3.2.1 Anisotropy in NiTi sheets

A good number of investigations about the anisotropic mechanical behaviour of NiTi sheets can be found in literature. The works of Inoue et al. (1996), Gao and Yi (2003) and Liu (2015) show for example that the recoverable strain is maximum in the rolling direction (RD) and gradually decreases until reaching a minimum in the transversal direction (TD) (see Fig. 1.14). The absolute difference between these two directions may change with different heat treatments (Inoue et al., 1996), but the overall trend is the same.

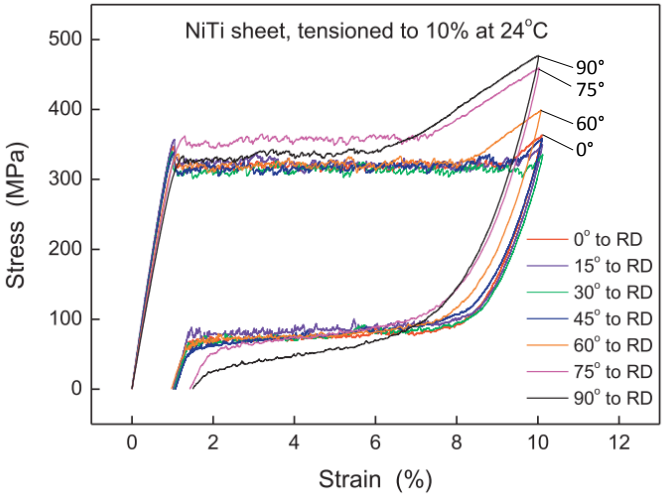

Figure 1.14: Tensile stress–strain curves of a NiTi thin sheet along different directions with respect to RD (From Liu, 2015).

Other mechanical properties were also investigated like elastic modulus and transformation stress. Gao and Yi (2003) extracted these two properties from stress-strain superelastic curves of tensile samples cut along various orientations and found out that the transformation stress is relatively low in the RD, reaches a minimum around 45° and again increases around the TD. For the elastic modulus they observed little variation between RD and TD. Liu (2015) also measured the orientation dependence of tensile damping capacity as the area inside the superelastic loop. The author observed a little decrease from RD until 60° with a subtle substantial increase for 75° and 90° (TD). This behaviour is related to the fact that when loaded until 10% strain these two latter directions presented shorter stress plateaus.

1.3.2.2 Anisotropy in NiTi tubes

The number of works found in literature addressing the anisotropic mechanical behaviour of NiTi tubes is still small compared to NiTi sheets. As cited previously, Robertson et al. (2006) investigated the evolution of texture with heat treatments on a NiTi tube, among other forms, through X-ray diffraction. As-received tubes with 4.6 mm outer diameter and 0.35 mm thickness were subjected to three different heat treatments, each one representative of a typical industrial processing step, according to the authors (see

Fig. 1.15). The results showed that with heat treatment the texture in the thickness (radial) direction was redistributed from a mostly [111] to a mostly [110] and in the drawing direction the [111] texture was intensified.

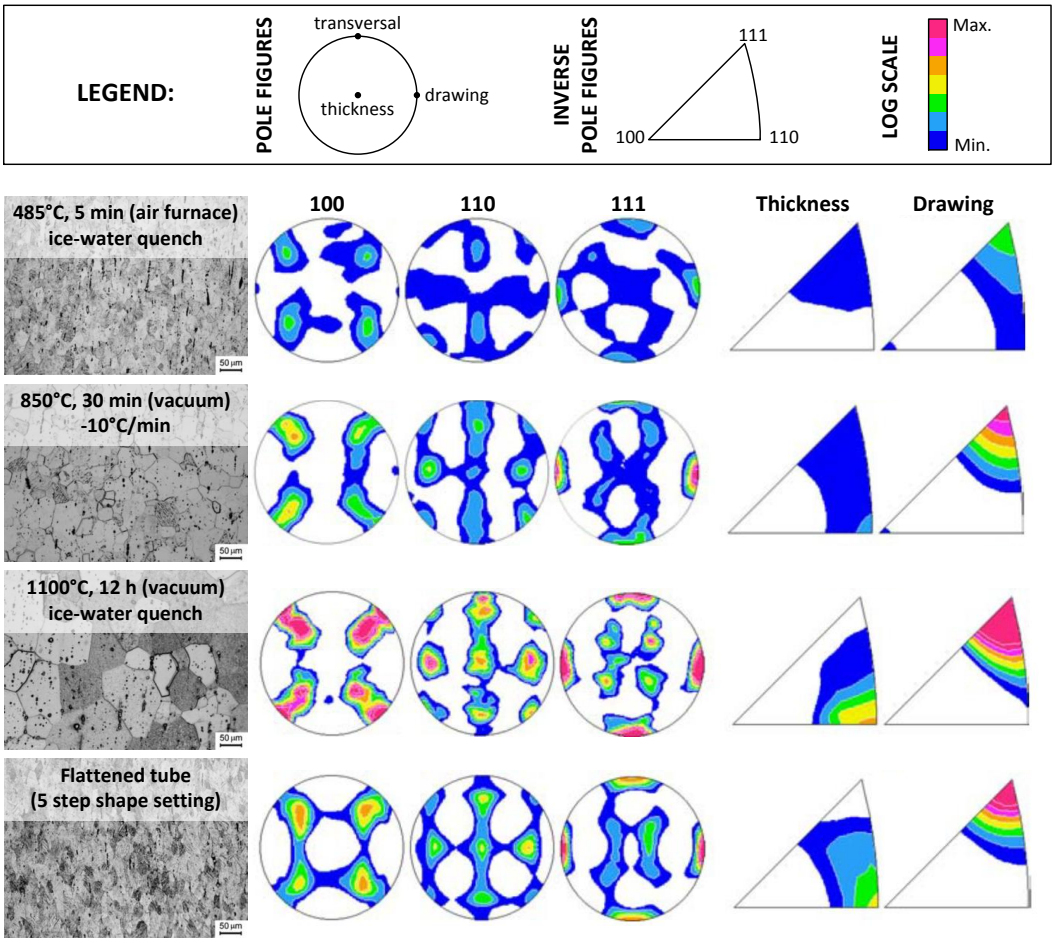

Figure 1.15: Texture evolution with heat treatment in a NiTi tube. Little change is observed in the drawing direction, that rather experiences an intensification of the [111] texture. In the thickness direction the texture evolves from mostly [111] to [110]. In the transversal direction mostly the [111] is observed, with some [110] (adapted from Robertson et al., 2006).

Moreover, the texture of an as-received flattened tube with 5.84 mm outer diameter and 0.43 mm thickness was studied (bottom of Fig. 1.15). The flattening process consisted of a five steps shape setting. They observed that the relatively strong flattening process did not alter significantly the tube texture when compared to the tube with the lightest heat treatment. The largest difference was the stronger [110] texture in the thickness direction on the flattened tube. Using the measured textures the authors estimated the transformation strain of the studied forms. Besides this estimation, it was presented an experimental curve of strain transformation dependence on orientation for the NiTi tube (Fig. 1.16). Both estimation and measurement tendencies agreed, showing that the smallest strain achieved happens at 45° from the drawing direction.

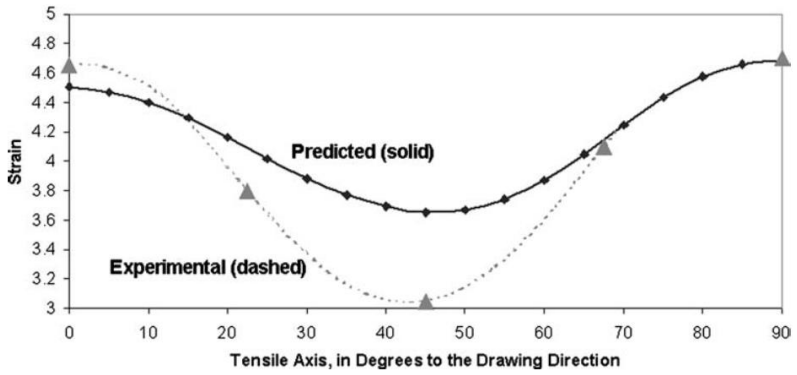

Figure 1.16: Measured and texture-predicted transformation strain at the end of stress plateau of a flattened tube at various angles relative to the tube drawing axis (From Robertson et al., 2006).

Another important contribution to the study of anisotropic behaviour of tubes is the work of Barney et al. (2011) in which micro dogbone samples were cut from a flattened tube at 0°, 45° and 90° from the drawing direction. Figure 1.18 shows the tensile behaviour of these samples.

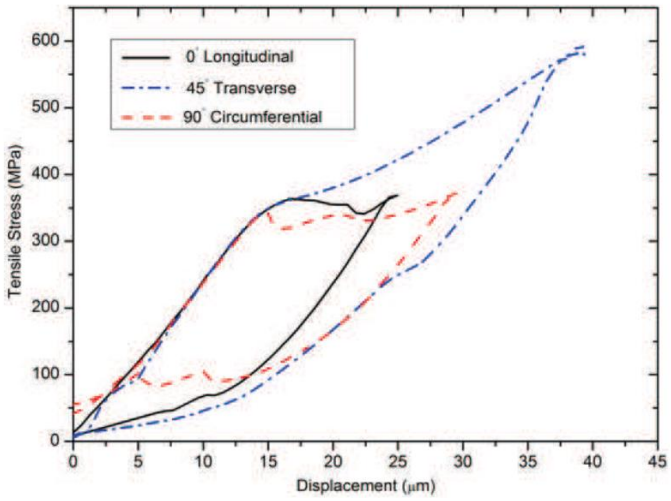

Figure 1.17: Global uniaxial tensile stress-displacement behaviour of samples cut at 0°, 45° and 90° from the tube drawing direction. Tensile samples' gauge section measures $800 \times 200 \times 200$ μm to allow simultaneous diffraction measurements (From Barney et al., 2011).

With X-ray diffraction measurements they reported that these tensile samples are mostly composed of crystals oriented in the [111], [100] and [110] directions, respectively, regarding the tensile axis. As aforementioned, the [111] and [110] single crystals have similar mechanical behaviour. Indeed, samples cut from the tube at 0° and 90° behave alike, as shown in Fig. 1.18. Figure 1.18 show the local grain distribution in the 0° and 45° dogbone samples as well as the averaged texture.

Tensile tests were performed with simultaneous X-ray diffraction measurements. The authors were able to discuss the local transformational behaviour. Grain-level elastic strain maps were built throughout tensile test, as shown in Fig. 1.19. The black regions are grains that have exceed the elastic limit and have started the phase transformation.

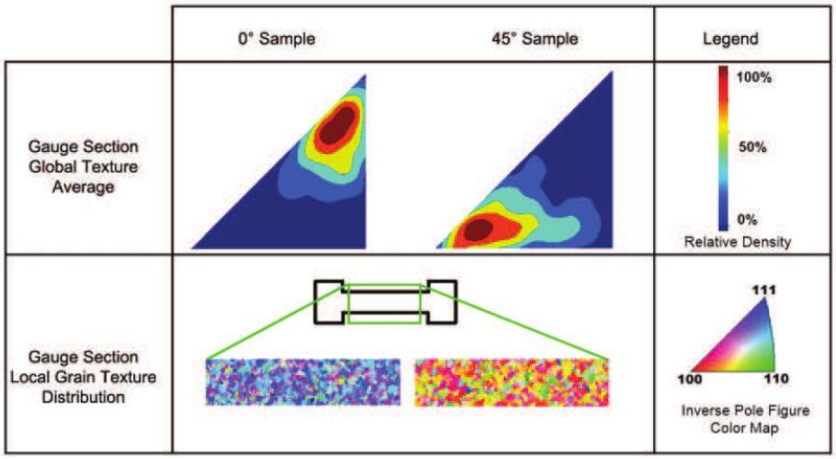

Figure 1.18: Global texture averaged in the gauge area and local texture distribution in the tensile samples cut from 0° and 45° from the NiTi tube drawing direction (From Barney et al., 2011).

It can be noticed that the transformed zones (black regions) in the maps of the 0° and 45° dogbone samples have very distinct morphologies. The distribution of transformed zones appears more concentrated in the 0° sample, while it is more scattered throughout the gauge area in the 45° sample. As transformation propagates in this latter it leaves a significant number of untransformed grains. The hardened tensile behaviour of [100] oriented grains, which resist more the tensile strain than [111] or [110] crystals, causes this orientation dependence. This validates the single crystal observations and confirms that the anisotropy in polycrystalline alloys are indeed caused by crystallographic texture.

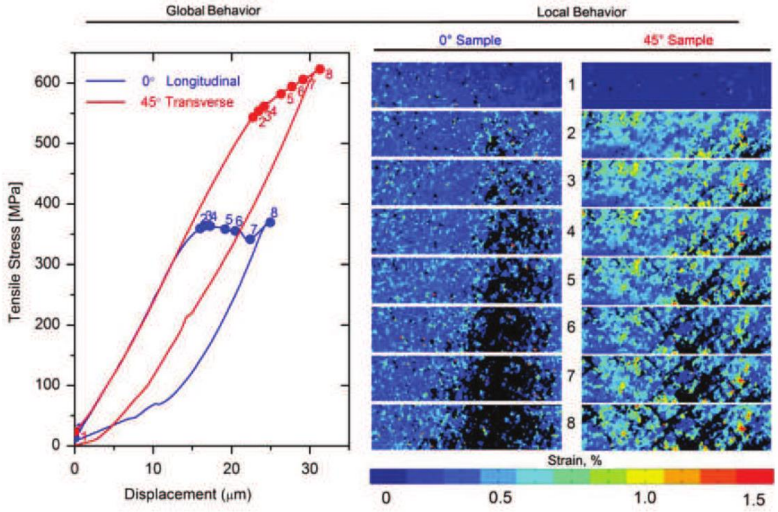

Figure 1.19: Evolution of grain local elastic strain of 0° and 45° NiTi digbone samples. The black zones are transformed grains (martensite phase). The samples' gauge length is 800μm which means loading was carried out until 3-4% tensile strain (From Barney et al., 2011).

1.4 Experimental observations of strain localization in NiTi alloys

Strain localization is a phenomenon widely reported in NiTi alloys submitted to tensile load. It is recognized macroscopically by the presence of a very defined boundary between a mostly untransformed zone and a mostly transformed zone in the material, accompanied by a stress plateau on the stress-strain curve.

The origin of this behaviour is still discussed, although experimental observations on polycrystalline NiTi indicate that it probably lies on the mechanical aspects of deformation (Šittner et al., 2005). Because of the macroscopic similarities between strain localization in NiTi SMA and Lüders bands in low-carbon steels, this strain localization is often called Lüders-like Deformation Mode (LDM). Both phenomena are strictly different at microscopic scale, though (more details in Section 1.6.3.1).

1.4.1 Localization phenomenon in SMA: influence of stress state

In SMA the strain localization phenomenon is observed under certain specific circumstances like, only in NiTi alloys and exclusively under tension. There are no reports about strain localization under compression (see Fig. 1.20a) or torsion. Under bending, NiTi wires and tubes show strain localization on the tensioned side (Bechle and Kyriakides, 2014; Reedlunn et al., 2014), as in the example of Fig. 1.20b. The compressed side shows a homogeneous strain field, following the tension-compression asymmetry observed in uniaxial loadings.

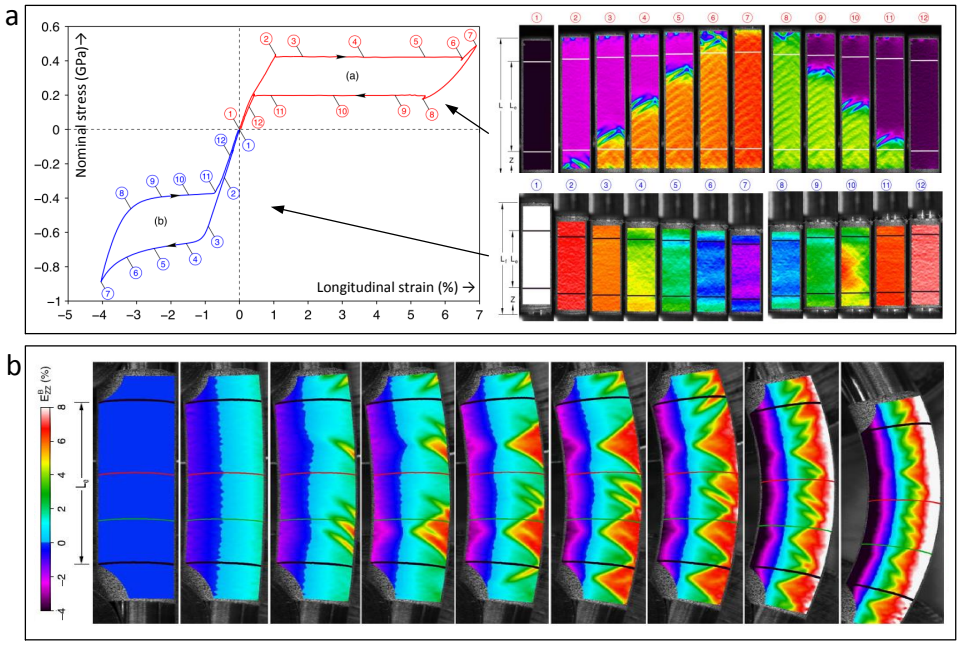

Figure 1.20: (a) Uniaxial behaviour a NiTi tube, showing localization during tensile loading but no localization during compressive loading. (b) Bending of the NiTi tube showing strain localization only on the tension side. (From Reedlunn et al., 2014).

Sun and Li (2002) showed experimentally how the localized behaviour of NiTi tubes under pure tension gradually becomes homogeneous when torsion is added, until no strain localization is observed when the tube is under pure shear (see Fig. 1.21). Instead of the stress plateau seen in pure tension, a monotonic hardening is observed in pure torsion.

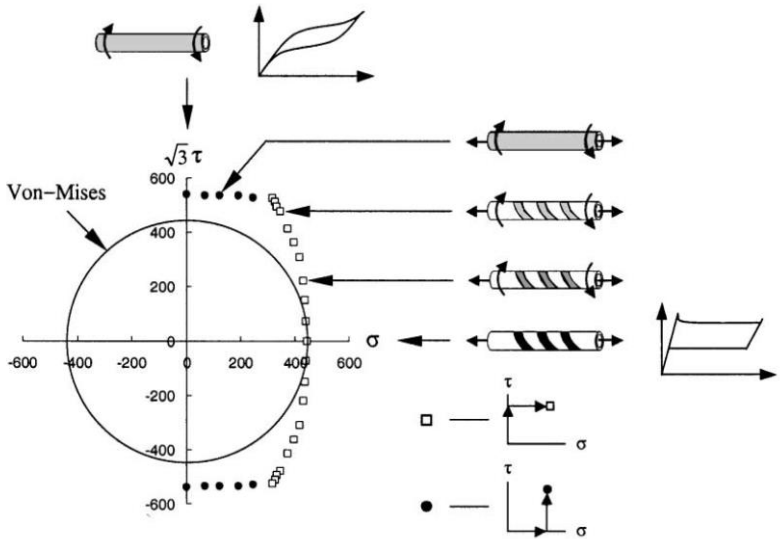

Figure 1.21: Evolution of strain distribution on the surface of a NiTi tube when subjected to stress states ranging from pure uniaxial tension to pure torsion (Sun and Li, 2002).

Recently, Bechle and Kyriakides (2016) also showed the evolution from localized to homogeneous behaviour in NiTi tubes submitted to various stress states combining axial load and internal pressure. They observed that the strain localization does not happen only in a narrow range of stress states near the equibiaxial condition.

Texture is considered to be the main source for this mechanical behaviour dependence on stress state. Other aspects seem to also play important roles like the anisotropy at the single crystal grain level (Šittner and Novák, 2000) and martensite low symmetry, besides detwinning during stress induced transformation (Favier and Orgéas, 1998).

1.4.2 Experimental conditions for localization in NiTi SMA

One of the main experimental conditions affecting the localization phenomenon in NiTi SMA is the strain rate (Elibol and Wagner, 2015; Iadicola and Shaw, 2004). High strain rates cause specimen self heating which, according to the Clausius-Clapeyron relationship, simultaneously increases the stress needed to keep the phase transformation going on. As a result, higher strain rates cause the nucleation and propagation of more bands in the specimen surface, as demonstrated by Kim and Daly (2013) (see Fig. 1.22). In the mechanical behaviour a monotonic hardening takes over the stress plateau.

Cycling also affects the occurrence of localized behaviour. It can induce a homogeneous deformation mode on specimens that originally experimented strain localization (Polatidis et al., 2015; Zotov et al., 2017). In general, after 100 transformation cycles the localization phenomenon gives way to an homogeneous deformation.

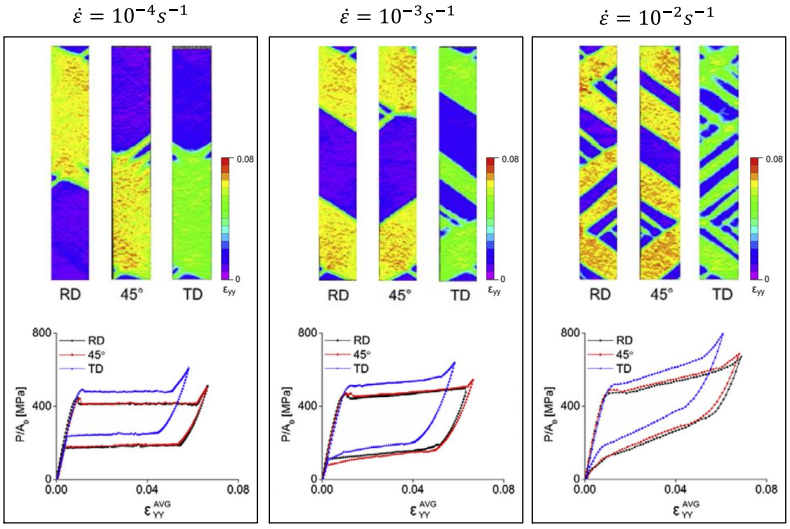

Figure 1.22: Evolution of strain localization behaviour with increasing strain rate in a NiTi strip (Kim and Daly, 2013). The maps correspond to an instant the middle of phase transformation plateau.

1.4.3 Influence of sample geometry

In addition, the localized behaviour depends on geometric factors such as specimen aspect ratio and shape. Shaw and Kyriakides (1998) observed that long NiTi strips under tension present sharp bands inclined 50° to 60° to the loading direction. Shear deformation associated with these bands cause kinking in the sample plane (see Fig. 1.23a), which is dependent on geometric, transformational and testing conditions.

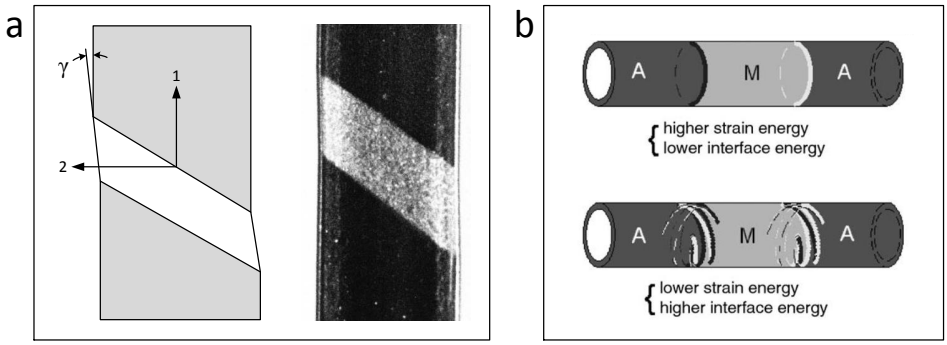

Figure 1.23: (a) Kinking angle schematically shown and an experimental example (Shaw and Kyriakides, 1998). (b) Schematic representation of different strain localization front morphologies (Feng and Sun, 2006).

In shorter strips, however, the kinking is more difficult and criss-crossed patterns are observed instead (see Fig. 1.23b). This difference in the morphology of front propagation can be an attempt of the material to be more thermodynamically stable, reducing the strain energy stored near the sharp band at the expense of increasing the surface energy of the front through the formation of fingers or criss-cross pattern, as discussed by Feng

and Sun (2006).

As for the shape of the specimen, when deformed under tension, the localization is recognized as a sharp inclined band in NiTi plates (Shaw and Kyriakides, 1998; Shaw and Kyriakides, 1997) (see Fig.1.24c) and as a conical transformation front in cylindrical specimens, perceived as bands perpendicular to the loading direction (Sedmak et al., 2016a) (see Fig.1.24d).

In tubes under tension the localization morphology has been reported to be helical or annular around the tube surface. Schlosser (2008) verified that the band morphology in NiTi in tubes strongly depends on temperature and on macroscopic strain rate. When tensile tests were performed with water flow inside the tube, the band observed was annular and perpendicular to the tube axis. When tests are performed without internal flow, NiTi tubes generally have a helical front (Favier et al., 2007; Feng and Sun, 2006; Sun and Li, 2002).

Besides the differences in the transformation front morphology, differences in the stress-strain response are observed for different material shapes, presumably caused by texture. Tensile samples cut from polycrystalline NiTi sheet along various directions all present a stress plateau under tension, although the length of the plateau changes with orientation (Gao and Yi, 2003; Liu, 2015). Meanwhile, samples cut from flattened NiTi tubes do not present localized behaviour around the 45° direction (Barney et al., 2011).

1.4.4 Evolution of techniques used to observe strain localization phenomenon in NiTi

Some of the most used techniques to observe localization phenomenon are based either on the strain difference between phases or on the temperature difference due to heat release or absorption during transformation.

One of the first observations of localization in NiTi alloys was performed using four thermocouples attached to a wire under tension and measuring the evolution of temperature in each point during a tensile loading (Leo et al., 1993). In the same manner, Shaw and Kyriakides (1995) coupled miniature extensometers and thermocouples along the length of a NiTi wire to follow local strains and temperatures (Fig. 1.24a). The information provided with this technique is, however, discontinuous and unidimensional.

Some years later Shaw and Kyriakides (1997) used thin layers of brittle coating (TiO_2) applied on the surface of NiTi strip specimens. The oxide layer cracks whenever a localization front appears and propagates, allowing to identify the strain localization with naked eye as a change in the color of the specimen 2D surface (Fig. 1.24b). The downside of this technique is that it does not provide quantitative information about the strain state of the material. Also, there is a loss of contrast between forward and reverse transformations since part of the oxide layer detaches during loading.

In this same work the authors also followed the transformation with a thermal camera. This latter technique is still broadly used mainly in thermomechanical coupling studies. Nowadays the vast majority of works use Digital Image Correlation (DIC) to measure displacement, strain and velocity fields. This technique can be used on 2D or 3D surfaces, providing very good quantitative data (Fig. 1.24c).

Lastly, diffraction techniques like 2D and 3D X-ray diffraction can be used to measure surface or volumetric strain and stress fields in the grain level, as demonstrated by the

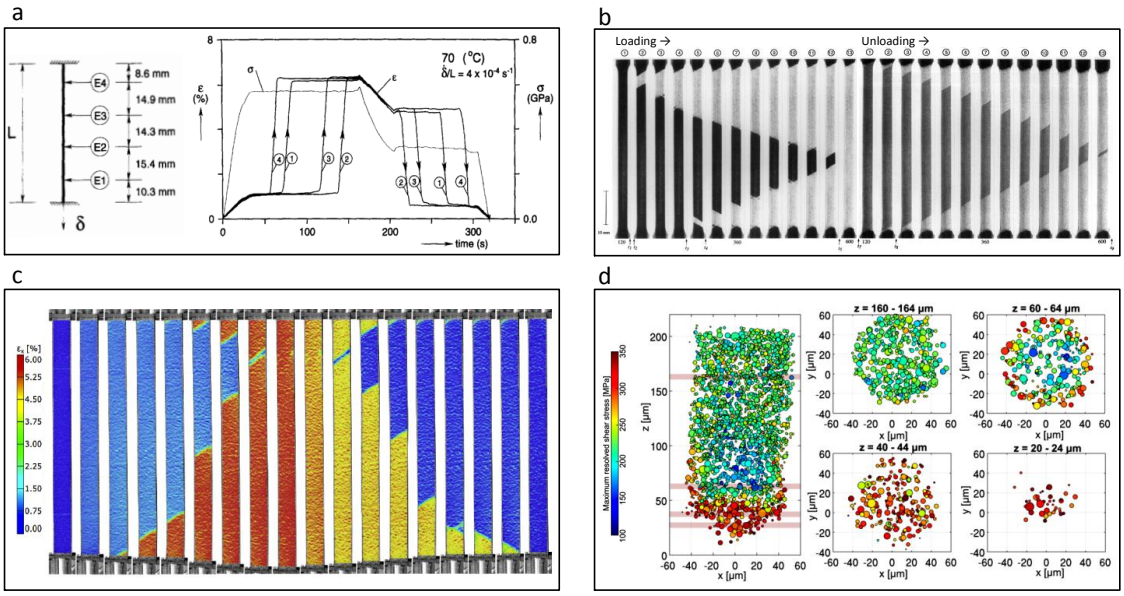

Figure 1.24: (a) Strain profiles obtained from four extensometers installed on a NiTi wire (Shaw and Kyriakides, 1995). (b) Strain localization phenomenon observed on the surface of NiTi strips through oxide layer cracking (Shaw and Kyriakides, 1997). (c) Strain fields on the surface of NiTi strips captured with digital image correlation (Jiang et al., 2017). (d) Stress state in the grain level in a NiTi wire calculated using 3D-XRD technique (Sedmak et al., 2016b).

works of Sedmak et al. (2016a) on NiTi wires, Mao et al. (2010) on NiTi tubes and Barney et al. (2011) on NiTi speciments cut from flattened tubes (Fig. 1.24d).

1.5 Thermodynamic framework of thermoelastic martensitic transformation

A thermoelastic martensitic phase transformation is a first-order diffusionless transition between two solid phases, comparable to the allotropic transformation of a pure element (Wollants et al., 1993). However, differently from allotropic transformations, thermoelastic martensitic transformation is accompanied by a recoverable macroscopic deformation which is in its nature a source of irreversibility, deviating the system from the thermodynamic equilibrium.

Based mainly on the works of Ortín and Planes (1989) and Wollants et al. (1993), this section shows the description of the thermoelastic martensitic transformation from a thermodynamic point of view. The hypothetical absence of any irreversibility is firstly considered. Next, the particular case of a uniaxial stress induced phase transformation is presented. Finally, the sources of irreversibility are introduced and its effects on thermomechanical behaviour are discussed.

Notation and units

The units of properties involved in the thermodynamic framework is listed on Table 1.1.

The units apply to the symbols even when sub or superscripts are added. This table is for reference and throughout text these symbols are still presented. Throughout this section $\Delta\bullet$ denotes the difference of a property between martensite and the parent phases.

Table 1.1: Units of the properties used in this thermodynamic framework

Symbol	Property	Unit
C	Clausius-Clapeyron coefficient	Pa/K
C_P	specific heat capacity at constant hydrostatic pressure	J/kg.K
E_{fr}	specific frictional work	J/kg
E_{st}	specific stored elastic energy	J/kg
ε	uniaxial strain	-
f_m	martensite fraction	-
G	specific Gibbs free energy	J/kg
H	specific enthalpy	J/kg
P	pressure	Pa
ρ	mass density	kg/m^3
S	specific entropy	J/kg.K
σ	uniaxial stress	Pa
T	temperature	K
U	specific internal energy	J/kg
V	specific volume	m^3/kg
W	specific work	J/kg

1.5.1 The Gibbs free energy equation

A **thermodynamic potential** is a state function that describes the behaviour of a thermodynamic system as function of its natural variables. For the thermodynamic system consisting of martensite or austenite phases, the thermodynamic potential is the Gibbs free energy G and the natural variables are pressure P and temperature T. According to the first and second laws of thermodynamics, Eq. (1.1) relates G to P and V for the case where only $P-V$ reversible work is involved

$$G(P,T) = U + PV - TS = H - TS \tag{1.1}$$

where U is the specific internal energy, V is the specific volume, S is the specific entropy and H is the specific enthalpy.

The driving force for the phase transformation is the difference between the Gibbs free energy of of austenite $G^A_{P,T}$ and that of martensite $G^M_{P,T}$:

$$\Delta G_{P,T} = G^M_{P,T} - G^A_{P,T} \tag{1.2}$$

A thermodynamic equilibrium is met when the difference between the thermodynamic potential of the phases is minimal for a set of values of the natural variables (P, T) . In the two-phase system composed by martensite (M) and austenite phases (A), this means at

$$G^M_{P,T} = G^A_{P,T} \tag{1.3}$$

and according to Eq. (1.1), at

$$\Delta G_{P,T} = \Delta H_{P,T} - T\Delta S_{P,T} = 0 \tag{1.4}$$

with $\Delta H_{P,T}$ and $\Delta S_{P,T}$ being the enthalpy and entropy variation between phases at a given P, T pair. They originate from the chemical differences of austenite and martensite phases. Figures 1.25a and 1.25b illustrate schematically $G^M_{P,T}$ and $G^A_{P,T}$ in a constant temperature and constant pressure scenarios, respectively.

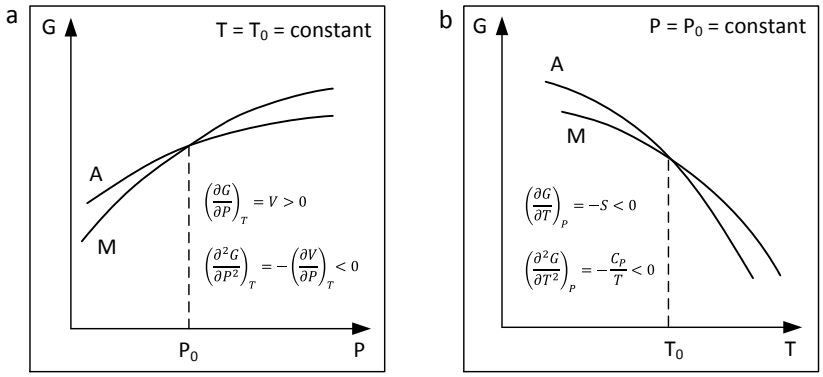

Figure 1.25: (a) Isothermic and (b) isobaric schematic behaviour of austenite and martensite Gibss free energy (From Wollants et al., 1993). C_P is the specific heat at constant pressure.

Because this is a first-order transformation, the thermodynamic equilibrium can be unambiguously defined as occurring at temperature T_0 at constant pressure, or at pressure P_0 at constant temperature.

Furthermore, Eq (1.4) states that, keeping one natural variable constant while varying the other, the chemical difference between martensite and austenite, given by $\Delta H_{P,T}$ and $\Delta S_{P,T}$, alone triggers the phase transformation. This is true in the hypothetical situation where no irreversibilities occur. Figure 1.26 illustrates the case where only these chemical contributions ($\Delta H_{P,T}$ and $\Delta S_{P,T}$) are present in the phase transformation, considering that heat capacities of austenite and martensite are equal at any temperature ($C^A_P = C^M_P$ $\forall\ T$). The graph in Fig. 1.26 also illustrates the following facts:

- The slope of the ΔG versus T curve is the entropy change ΔS.
- The value of ΔG when $T = 0$ K is the enthalpy change ΔH of the transformation.
- The chemical differences ΔH and ΔS are both negative.

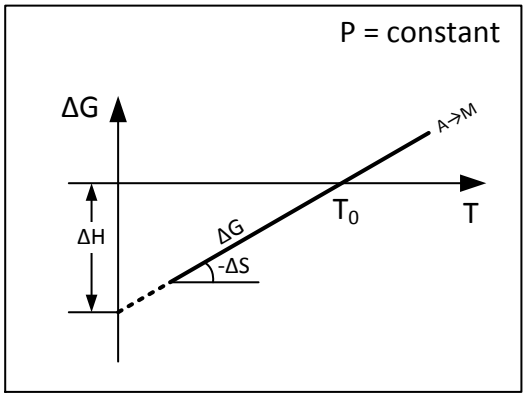

Figure 1.26: Gibbs free energy difference in function of temperature in a thermodynamic equilibrium situation, according to Eq. 1.3 and considering $C_P^A = C_P^M \ \forall \ T$ (From Wollants et al., 1993).

The Clausius-Clapeyron relation when only P-V work is involved

The Clausius-Clapeyron equation relates the two natural variables P and T. It is obtained from the fundamental Equation (1.1):

$$dG = VdP - SdT \tag{1.5}$$

In the thermodynamic equilibrium $dG = 0$ in Eq. 1.5 and the relation between P and T is given by

$$\frac{dP}{dT} = \frac{\Delta S}{\Delta V} = \frac{\Delta H}{T\Delta V} \tag{1.6}$$

ΔV is the difference of specific volume between martensite and austenite. In SMA $\Delta V \approx 0$.

1.5.2 Uniaxially stress-induced transformation

When a stress is externally applied in the thermodynamic system, the thermoelastic martensitic transformation is said to be stress-induced. In this case a reversible mechanical work is performed on the system. According to continuum mechanics theory, the mechanical work per unit of mass performed on a representative element volume (REV) can be written as a function of the average stress and macroscopic strain tensors. If the stress is applied uniaxially and only transformation strain is considered, an infinitesimal amount of mechanical work is

$$dW_{mech} = \frac{1}{\rho}\sigma d\varepsilon_{tr} \tag{1.7}$$

where ρ is the mass density, σ is the uniaxial stress externally applied on the system and ε_{tr} is the transformation component of uniaxial macroscopic strain.

Introducing f_m as the martensite fraction and df_m as an infinitesimal step of martensite fraction, Eq. (1.7) can be written as

$$\frac{1}{\rho}\sigma d\varepsilon_{tr} = \left(\frac{\partial W_{mech}}{\partial f_m}\right) df_m = W'_{mech} df_m \tag{1.8}$$

A linear relation between $d\varepsilon_{tr}$ and df_m is assumed:

$$d\varepsilon_{tr} = \Delta\varepsilon_{tr} df_m \tag{1.9}$$

where $\Delta\varepsilon_{tr}$ is defined as the transformation strain for a complete transformation, at $f_m = 1$. Equation (1.8) then becomes

$$W'_{mech} = \frac{1}{\rho}\sigma\Delta\varepsilon_{tr} \tag{1.10}$$

Finally, the difference between the specific Gibbs free energy of martensite and austenite in Eq. (1.4) can be rewritten as

$$\Delta G_{P,T} = \Delta H_{P,T} - T\Delta S_{P,T} - \frac{1}{\rho}\sigma\Delta\varepsilon_{tr} = 0 \tag{1.11}$$

which expresses the thermodynamic potential of a uniaxially stress-induced thermoelastic martensitic transformation happening on thermodynamic equilibrium. Figure 1.27 shows the ΔG difference when external mechanical work is involved in the transformation.

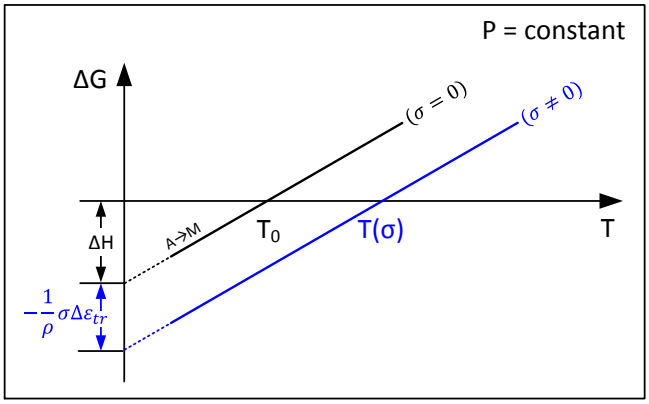

Figure 1.27: Gibbs free energy difference in function of temperature in a thermodynamic equilibrium situation where reversible external work is involved (adapted from Wollants et al., 1993).

This external work displaces the thermodynamic equilibrium, that now occurs at $T = T(\sigma)$. However, it does not change the fact that the transformation happens isothermically when pressure is kept constant.

The Clausius-Clapeyron relation when external mechanical work is involved

From Eq. 1.27, and analogously to the case with only P-V work, the Clausius-Clapeyron equation relates external stress σ and temperature through

$$\frac{d\sigma}{dT} = -\frac{\rho\Delta S}{\Delta\varepsilon_{tr}} = -\frac{\rho\Delta H}{T\Delta\varepsilon_{tr}} \tag{1.12}$$

1.5.3 Sources of thermodynamic irreversibility

In the previous section the thermodynamic potential for phase transformation was presented for the case where only reversible work is involved (either $P - V$ or external mechanical work). However, in reality, the martensitic phase transformation does not occur isothermally, but rather in a temperature range, generally accompanied by a hysteresis between forward and reverse transformations.

These deviations from equilibrium are caused by the presence of two main non-chemical irreversible contributions in the thermodynamic potential: the **stored elastic energy**, associated with the shape and volume changes during transformation between austenite and martensite; and the **frictional work**, associated with the energy dissipated by the relative movements between the austenite and martensite interfaces.

Stored elastic energy

The stored elastic energy has two sources: elastic strain energy and interfacial energy (Hamilton et al., 2004; Ortín and Planes, 1989). The first can be defined as the work performed against internal forces to modify the total strain of the system. The latter comes from the creation of new interfaces and/or changes in existing interface dimensions.

This generation process is different for thermally and stress induced phase transformations. In the first scenario no appreciable shape or volume changes are involved because the martensite is formed in a self-accommodated manner, minimizing elastic strain energy. Nevertheless, the interfacial energy is present and is therefore the main reversible non-chemical contribution for the system free energy. In the presence of external stress both elastic strain and interfacial energies exist.

The stored elastic energy constitutes an opposition to the forward transformation, during which the energy is stored elastically. During the reverse transformation the energy previously stored is released, favouring the transformation in this sense. However, this mechanical reversibility does not mean a thermodynamic reversibility. Its existence still constitutes a source of irreversibility because it is responsible for the transformation to not occur isothermally, but instead within a temperature range. Figure 1.28 shows schematically the isolated effect of reversible stored elastic energy. The difference between T_0 and T_f is directly related to the amount of stored elastic energy in the system.

Frictional work

Frictional work is present in thermally or stress induced transformations, even in single-crystal single-interface specimens, where no shape or volume change occurs. It can be defined as the work performed to overcome interface motion, which is directly related to the amount and nature of the barriers opposing the movement of transformation fronts. This parcel of energy is ultimately dissipated from the system as heat (Wollants et al., 1993), during both forward and reverse transformations.

It constitutes a thermodynamic irreversibility because it increases the entropy of the universe (transforming system + surrounding), degrading the useful work performed by the system. Taking as reference the thermomechanical behaviour at the thermodynamic

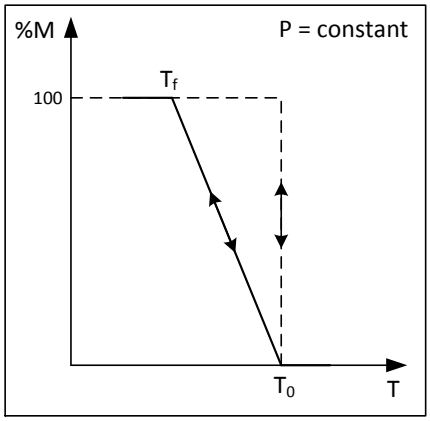

Figure 1.28: Isolated effect of stored elastic energy on the thermodynamic behaviour of the temperature induced thermoelastic transformation ($\sigma = 0$) (Hamilton et al., 2004).

equilibrium, Fig. 1.29 shows schematically the isolated effect of frictional work on the transforming behaviour of the two-solid phase system composed of austenite and martensite. The size of the hysteresis cycle (shaded area) is directly related to the frictional work dissipated.

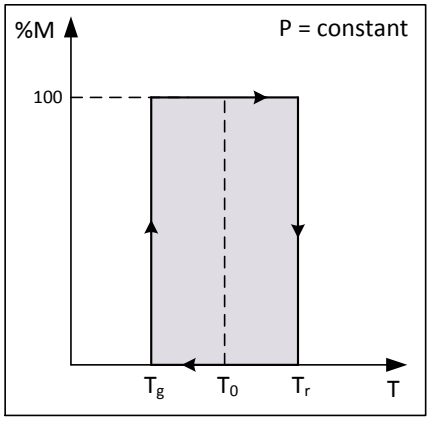

Figure 1.29: Isolated effect of frictional work on the thermodynamic behaviour of the temperature induced thermoelastic transformation ($\sigma = 0$) (Wollants et al., 1993).

1.5.4 Effect of thermodynamic irreversibilities on mechanical behaviour in the presence of mechanical load ($\sigma, \varepsilon \neq 0$)

The thermomechanical behaviour of SMA undergoing martensitic phase transformation in the presence of mechanical work is much affected by thermodynamic irreversibilities. Figure 1.30 illustrates the mixed effect of frictional work and stored elastic energy on

the strain-temperature behaviour. They are responsible for the initial and final phase transformation temperatures M_s, M_f, A_s and A_f.

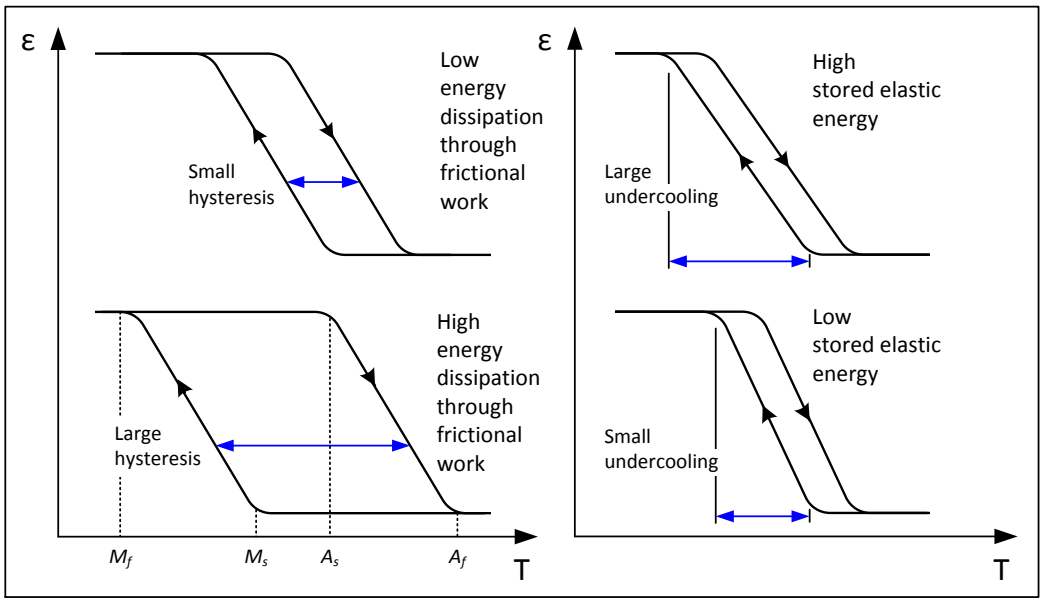

Figure 1.30: Mixed effect of frictional work and stored elastic energy on the thermomechanical behaviour of the SMA phase transformation in the presence of mechanical work ($\sigma, \varepsilon \neq 0$) (Hamilton et al., 2004)).

1.5.5 Thermodynamic potential with irreversibility contributions

These irreversible contributions must be added to the thermodynamic potential expressed in Eq. (1.4), characterizing the thermoelastic phase transformation as it happens in reality. From now on, the subscript notation "P, T" is omitted and the following subscripts are adopted: "ch" for chemical energy contributions, "fr" for frictional work and "st" for stored elastic energy.

Since frictional work and stored elastic energy are not state functions, the thermodynamic potential is written as function of an infinitesimal matensite fraction step df_m. Thus, for a given set of natural variables one obtains

$$dG = (\Delta H_{ch} - T\Delta S_{ch})df_m + (\partial E_{st}/\partial f_m)df_m + (\partial E_{fr}/\partial f_m)df_m = 0 \tag{1.13}$$

where ΔH_{ch} and ΔS_{ch} are the chemical contributions of enthalpy and entropy changes, respectively; and E_{st} and E_{fr} are the contributions of stored elastic energy and frictional work, respectively.

In derivative form one has

$$G' = \Delta H_{ch} - T\Delta S_{ch} + E'_{st} + E'_{fr} = 0 \tag{1.14}$$

where the superscript $'$ designates the partial derivative of a property in relation to f_m. Thus, $E'_{st} = \partial E_{st}/\partial f_m$ and $E'_{fr} = \partial E_{fr}/\partial f_m$.

When the material is fully in the austenite phase $f_m = 0$ and when fully in the martensite phase $f_m = 1$. During the forward transformation the infinitesimal martensite mass fraction step df_m is positive and during reverse transformation it is negative.

Including the contribution of an external mechanical work in a stress-induced phase transformation occurring under the application of uniaxial stress, Eq. (1.14) can be rewritten as

$$G' = \Delta H_{ch} - T\Delta S_{ch} + E'_{st} + E'_{fr} - \frac{1}{\rho}\sigma\Delta\varepsilon_{tr} = 0 \tag{1.15}$$

Sign convention

Considering that work performed by the system is negative and work performed on the system is positive, the sign of each non-chemical contribution in Eq. (1.14) can be defined for the forward and reverse transformations.

The stored elastic energy is work performed by the system during forward transformation and work performed on the system during reverse transformation. Therefore dE'_{st} must be positive during forward and negative during reverse transformation. This makes both $E'^{A\to M}_{st}$ and $E'^{M\to A}_{st}$ positive values due to df_m signs in each sense. The frictional work is always performed by the system and thus is always positive. This leads to a positive $E'^{A\to M}_{fr}$ and a negative $E'^{M\to A}_{fr}$. Furthermore, ΔH_{ch} and ΔS_{ch} are both negative.

The Clausius-Clapeyron relation

The temperature derivative of Eq. (1.15) gives the relation between uniaxial stress and temperature. If it is assumed that ρ, $\Delta\varepsilon_{tr}$, E'_{st} and E'_{fr} do not depend on temperature, the usual Clausius-Clepeyron relation is obtained:

$$\frac{d\sigma}{dT} = -\frac{\rho\Delta S_{ch}}{\Delta\varepsilon_{tr}} \tag{1.16}$$

1.6 Mechanics of strain localization

1.6.1 Different types of strain localization

Strain localization is a phenomenon observed in many ductile materials. During a tensile test, it takes place when the deformation distribution throughout a body changes from homogeneous to inhomogeneous upon achieving a certain stress level. In classic materials this phenomenon is observed during plasticity and is widely acknowledged as a plastic instability. This subject receives a lot of attention among metallurgists because plastic instabilities generally precede failure.

In SMA, however, strain localization is related to the phase transformation, and therefore is reversible. Although both cases are fundamentally different regarding their crystallographic nature, their macroscopic manifestations are very comparable (Shaw and Kyriakides, 1998; Šittner et al., 2005). For this reason, theoretical approaches addressing

the localization in SMA are based in the plasticity theory developed for classic metallic alloys.

Lüders bands and localized necking are the two phenomena to which SMA localization is mostly referred to. Although both terms are often used interchangeably (Šittner et al., 2005), both designating a macroscopic strain localization, metallurgists differentiate them. Lüders bands is a plastic instability that generally takes place between elastic and plastic regimes. Its occurrence is related to very specific crystallographic conditions.

Localized necking is a strain localization mostly observed when plasticity is already established and fracture is imminent. The conditions for its occurrence are rather explained based on continuum mechanics.

The next subsections are dedicated to present the theories developed to explain both Lüders deformation mode and localized necking and contextualize the localization observed in NiTi alloys in view of these theories.

1.6.2 Mechanics of strain localization in usual metallic alloys

1.6.2.1 Lüders bands

According to specific crystallographic conditions, the transition from linear elastic to plastic deformation in metallic alloys can be either smooth (Fig. 1.31a) or very well marked (Fig. 1.31b). The discontinuity between elastic and plastic regimes in the curve of Fig. 1.31b is the macroscopic mechanical manifestation of the presence of Lüders bands, which characterize the LDM.

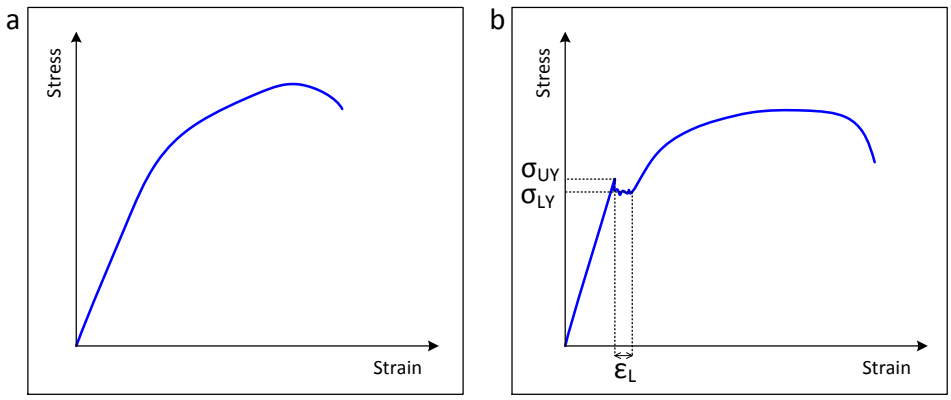

Figure 1.31: Schematic tensile stress-strain curves (a) with homogeneous deformation only and (b) with Lüders bands behaviour.

This transitory deformation mode is characterized by a drop in tension followed by a fluctuation around an average stress value. The stress σ_{UY} is called upper yield stress and the average fluctuation stress σ_{LY} is called lower yield stress. ε_L is the Lüders strain, reaching around 1-3 % in mild steels (Ananthan and Hall, 1991; Sylwestrowicz and Hall, 1951).

This material instability causes an undesirable surface irregularity during sheet metal forming processes (Sotomayor and Herrera, 1994). This inconvenience, and the quest to

avoid it, is the reason why Lüders bands is a phenomenon extensively studied and well understood among metallurgists.

Crystallographic causes Lüders bands behaviour in usual metallic alloys

For many polycrystalline alloys, the typical mechanism of plastic deformation is slip, which consists in the movement of dislocations (linear crystallographic defects) throughout the material. The Lüders bands phenomenon happens under specific crystallographic conditions related to restrictions to the movement of dislocations, which ultimately causes their movement to be noticeable in the macro-scale.

According to dislocation theory, such restrictions are solute interstitial carbon and nitrogen atoms clustered around dislocations, known as Cottrell atmospheres (Cottrell and Bilby, 1949). During a uniaxial test, the upper yield stress σ_{UY} marks the first episode of dislocation release from the Cottrell atmospheres. After this fist burst of dislocation movement the stress drops until the lower yield point. The fluctuation around the lower yield stress is then caused by subsequent episodes of dislocation releasing, movement and re-blocking. This continues until all the dislocations have freed themselves and have swept the tensioned material. After that, the plastic deformation continues normally, generally with strain hardening.

1.6.2.2 The Schmid law

Regardless of the strain distribution in a material, the slip mechanism takes place along a specific plane and a specific direction in a grain. Both constitute the grain slip system, as illustrated in Fig. 1.32. The slip system (plane and direction) is characteristic of the crystallographic structure (face-centred cubic, body centred-cubic, hexagonal, etc).

By knowing the slip system of a grain it is possible to calculate the critical resolved shear stress (τ_c) that will initiate the slip in the grain. This is performed through the Schmid law, under the assumption that the stress state is homogeneous throughout the material. This law is expressed in Eq. 1.17 for a uniaxial tensile loading:

$$\tau_c = \frac{\text{resolved force acting on slip plane}}{\text{area of slip plane}} = \frac{F_c \cos\lambda}{A/\cos\varphi} = \frac{F_c}{A}\cos\varphi\cos\lambda = \sigma_c \cos\varphi\cos\lambda \tag{1.17}$$

where φ is the angle between the applied tensile load and the slip plane and λ is the angle between the applied tensile load and the slip direction, as illustrated in Fig. 1.32. From Eq. 1.17, the **Schmid factor** (m) is defined as

$$m = \cos\varphi\cos\lambda \tag{1.18}$$

and the Schmid law can be written as

$$\tau_c = \sigma_c m \tag{1.19}$$

In a polycrystalline material under uniaxial load, Eq. 1.19 can be used to identify which grains will first experience slip as being the ones with the larger Schmid factor. That is, which grains requires the lowest stress σ_c to begin slip.

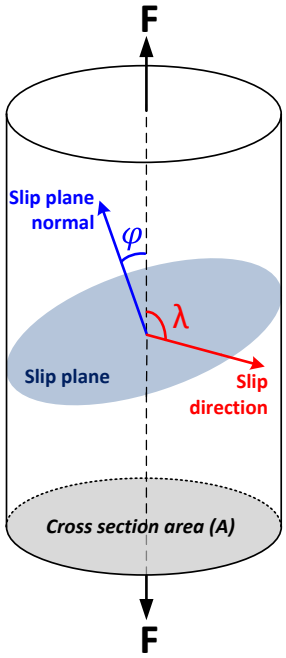

Figure 1.32: Scheme of slip system in a tensile sample and the angles used to calculate the Schmid factor.

The grains favourably oriented with the slip system will undergo slip before other grains that are less favourably oriented. This means that plastic deformation evolves inhomogeneously at the grain scale. In the macro-scale, the degree of strain inhomogeneity clearly depends on the material texture and on the loading direction.

1.6.2.3 Localized necking

Necking can be observed in uniaxial and biaxial tensile loadings of ductile metals. Encouraged by the automotive industry, many studies focused on investigating the necking phenomenon in the light of sheet metal forming processes, where diffuse and localized necking are distinguished (Aretz, 2007; Bao et al., 2016), as shown in Fig. 1.33.

Localized necking is always preceded by a diffuse necking. However, it is the localization that determines the maximum allowable strain in industrial stamping (Barata da Rocha et al., 1985), known as forming limits. The localized necking, therefore, is considered more important in practice.

The criterion of velocity discontinuity

Hill (1948, 1952) developed a theory for localization phenomenon occurring in a plane stress state ($\sigma_{33} = \sigma_{31} = \sigma_{32} = 0$). The localized neck is idealized as a discontinuity in velocity on the basis of plasticity theory. He states that the neck will appear along a *characteristic*, which is a direction of zero rate of extension.

Characteristics are solutions of partial differential equations (PDE). In the plane stress problem the strain equations are either hyperbolic or elliptic PDE (Hill, 1948), having two or none characteristics in the set of real numbers, respectively. Thus, in

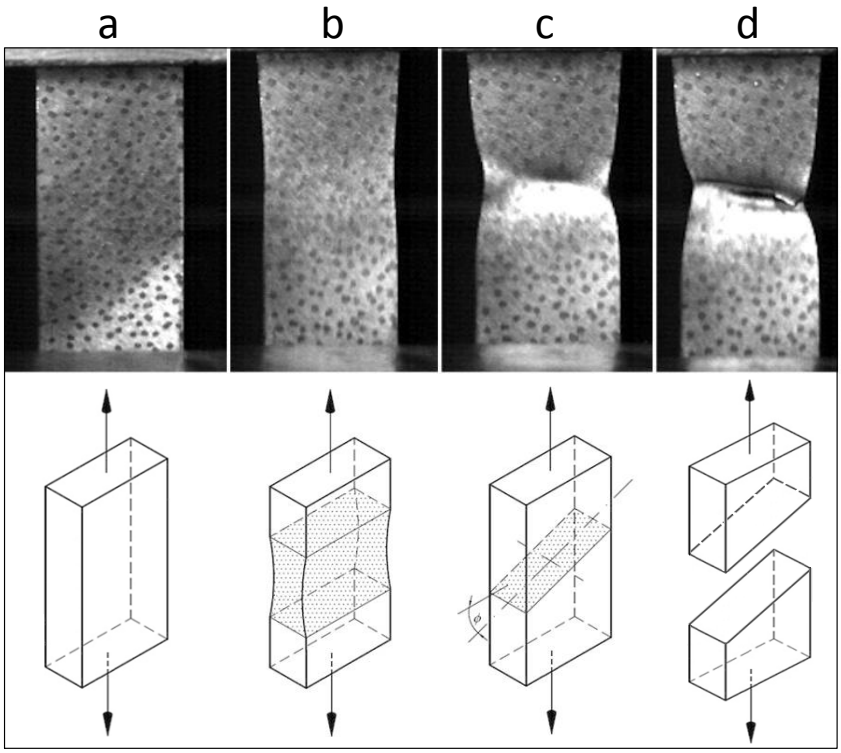

Figure 1.33: Photographs of a metallic sample at various stages of tensile loading: (a) uniform deformation, (b) diffused necking, (c) localized necking (d) and fracture (Krishnan et al., 2014). Neck domain is illustrated below the pictures.

a sheet uniaxially loaded, if the velocity equations are elliptic there is no localization. Otherwise, the neck will appear along one characteristic. Perpendicular to the other is the velocity vector $\overrightarrow{v}$ developed by the neck, which is different from that of the neighbouring material. Figure 1.34 illustrates these geometric relations in a thin sheet under tensile load.

The angle between $\overrightarrow{v}$ and the neck direction is ψ and is related with the strain increment on the principal directions 1 and 2 (in a plane stress state) by

$$\sin\psi = \frac{\dot{\varepsilon_1} + \dot{\varepsilon_2}}{\dot{\varepsilon_1} - \dot{\varepsilon_2}} \tag{1.20}$$

This expression states another condition for the occurrence of localized necking, which is $\psi \neq 0$. Otherwise there is no necking, only a relative sliding (Hill, 1952).

If a yield function f and a plastic potential are identical due to the use of an associative flow rule, stress and strain increment in the principal directions are related (in a plane stress state) by

$$f(\sigma_1, \sigma_2) = \text{constant}, \quad \frac{\partial f/\partial\sigma_1}{\partial f/\partial\sigma_2} = \frac{\dot{\varepsilon_1}}{\dot{\varepsilon_2}} \tag{1.21}$$

and Eq. 1.20 can also be written in terms of the yield function as

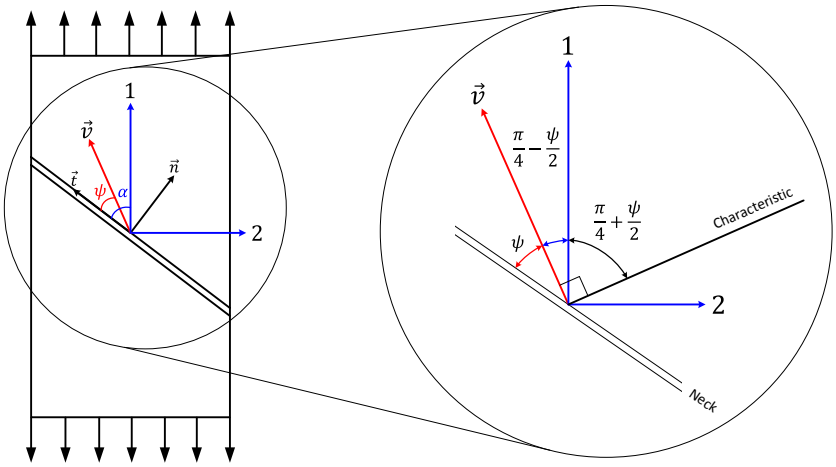

Figure 1.34: Illustration of a neck in a thin sheet under uniaxial tension caused by a velocity discontinuity along the direction of a strain rate characteristic (Hill, 1952; Shaw and Kyriakides, 1998).

$$\sin\psi = \frac{\left(\dfrac{\partial f}{\partial \sigma_1} + \dfrac{\partial f}{\partial \sigma_2}\right)}{\left(\dfrac{\partial f}{\partial \sigma_1} - \dfrac{\partial f}{\partial \sigma_2}\right)} \tag{1.22}$$

where σ_1 and σ_2 are the yield stresses in the principal directions of the material.

If an isotropic yield function is used in Eq. 1.22 the angle between the neck and the axis of applied tension can be calculated using the Lévy-Mises equations. It follows from these equations that under tensile stress along principal direction 1 that $\dot{\varepsilon_1}/\dot{\varepsilon_2} = -2$. Then, the angle between the neck and the tension direction is:

$$\psi = \sin^{-1}\left(\frac{1}{3}\right) = 19°28' \quad \text{and} \quad \alpha = \frac{1}{4}\pi + \frac{1}{2}\psi = 54°44' \tag{1.23}$$

Indeed band angles close to this predicted value were measured in mild-steel under tensile loadings (Ananthan and Hall, 1991). Sometimes, however, different angles are observed. Wakashima and Mori (1972) attributed these differences to the effect of internal stress from undeformed regions on each side of the band, which are not considered by Hill theory.

Also, applying an isotropic yield function in Eq. 1.22 results in a single value for band angle α. In order to take into account any orientation dependence, an anisotropic yield function should be used in this equation.

1.6.3 Mechanics of strain localization in NiTi SMA

Due to the many similarities between strain localization phenomenon in usual metallic alloys and NiTi SMA, the theories developed for plasticity are often applied for the

phase transformation. The next sections discuss the use of the aforementioned plasticity theories in the case of phase transformation in NiTi alloys.

1.6.3.1 Lüders deformation mode (LDM) in NiTi SMA

In NiTi SMA the LDM is observed in both shape memory effect, during martensite reorientation (Fig. 1.35a) and in superelasticity, during the stress induced phase transformation (Fig. 1.35b).

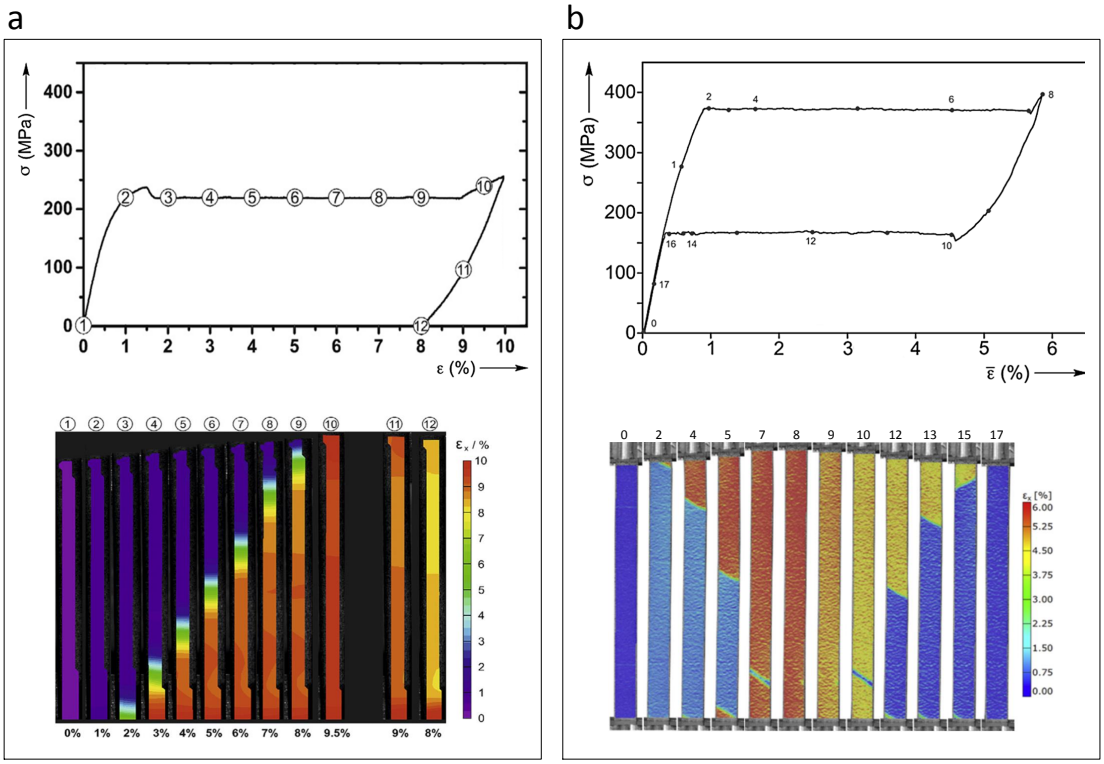

Figure 1.35: NiTi mechanical tensile behaviour at temperature T and corresponding strain distribution. (a) Wire originally at martensite state (M_s > T > M_f) during detwinning (adapted from Laplanche et al., 2017). (b) Strip originally at austenite state (T > A_f) during stress induced phase transformation (adapted from Jiang et al., 2017).

Like classic metallic alloys, NiTi SMA present a drop in tension prior to stress plateau. The upper "yield" point is associated with the nucleation of the first martensite domain during SE, or with the nucleation of the first reorientation domain in SME (Shaw and Kyriakides, 1997).

Unlike the LDM observed in classic alloys, the plateau strain in NiTi can reach 8% in tension (Liu, 2015). Also, since phase transformation and detwinning processes are crystallographically reversible, a stress plateau is also observed upon unloading.

1.6.3.2 Origin of LDM in NiTi SMA

For a long time many authors associated the stress plateau with the full phase transformation or reorientation process. However, it has been proved that both phenomena

start before and continue after the plateau (Favier et al., 2007; Stebner et al., 2015). The localization can be seen as an intensification of these phenomena (Brinson et al., 2004), but they do not happen exclusively while band(s) propagate.

In order to comprehend the origin of LDM in NiTi SMA many investigations have been carried out. The brief review that follows is based on the review presented by Mao et al. (2010).

Shaw and Kyriakides (1997) and Shaw and Kyriakides (1995) raised the hypothesis that the LDM in SMA can be explained by the difference between thermodynamic driving forces of martensite nucleation and variant growth during phase transformation. However, this argument was contested in view of the fact that the LDM is also observed during martensite reorientation, while no phase transformation takes place. In the same manner, the LDM is not observed during uniaxial compression where the phase transformation does take place.

Experimental observations have shown that the angle of the band front can reach as low as 48° (Pieczyska et al., 2006) and as high as 67° (Shaw and Kyriakides, 1998), suggesting that there is possibly an interaction between strain mechanics and martensite crystallography, and thus it can not be a mechanism purely governed by the mechanical principle of maximum shear stress.

Mao et al. (2007) used in situ EBSD technique to analyse the characteristics of LDM in bulk NiTi and concluded that it is the orientation and distribution of individual grains with respect to the orientation of the externally applied load that control the selection of some martensite variants to the detriment of others, as well as the propagation of the band front.

While the crystallographic motion experienced by SMA is not caused by slip but rather by reversible twinning, both mechanisms have in common a shearing nature. For this reason the Schmid factor criterion is widely used to predict how phase transformation evolves in a given SMA when stress is applied (Otsuka and Shimizu, 1986; Sehitoglu et al., 2001; Yu et al., 2015). For NiTi alloys, this criterion states that the martensite variant with the highest Schmid factor in the applied stress direction will be induced first among all possible variants (Liu, 2015). Figure 1.32 illustrates the plane and directions involved in the calculation of the Schmid factor in a SMA crystal, except that the slip plane is now considered to be the habit plane (planar interface between austenite and martensite phases).

In the work of Mao et al. (2010) the origin of LDM in SMA was investigated at the grain level. For this, they examined the asymmetry between tensile and compressive mechanical responses of a NiTi tube. Using EBSD technique, the orientation of the grains during tensile and compressive loading was defined. Then, the authors calculated the Schmid factor of several grains and compared the scattering for both loadings. The compressive Schmid factor scattering was significantly higher (±20%) than for tensile load (±8.7%), as shown in Fig. 1.36).

This result shows that in a NiTi tube the grains are oriented in such a way that the variation of the critical transformation stress for tension among grains is small. This favours the nucleation of a transformation domain in a concentrated zone (i.e. in a Lüders band). Meanwhile, under compression the critical transformation stress among grains differs significantly, causing the transformation to nucleate throughout the material, in a more distributed manner.

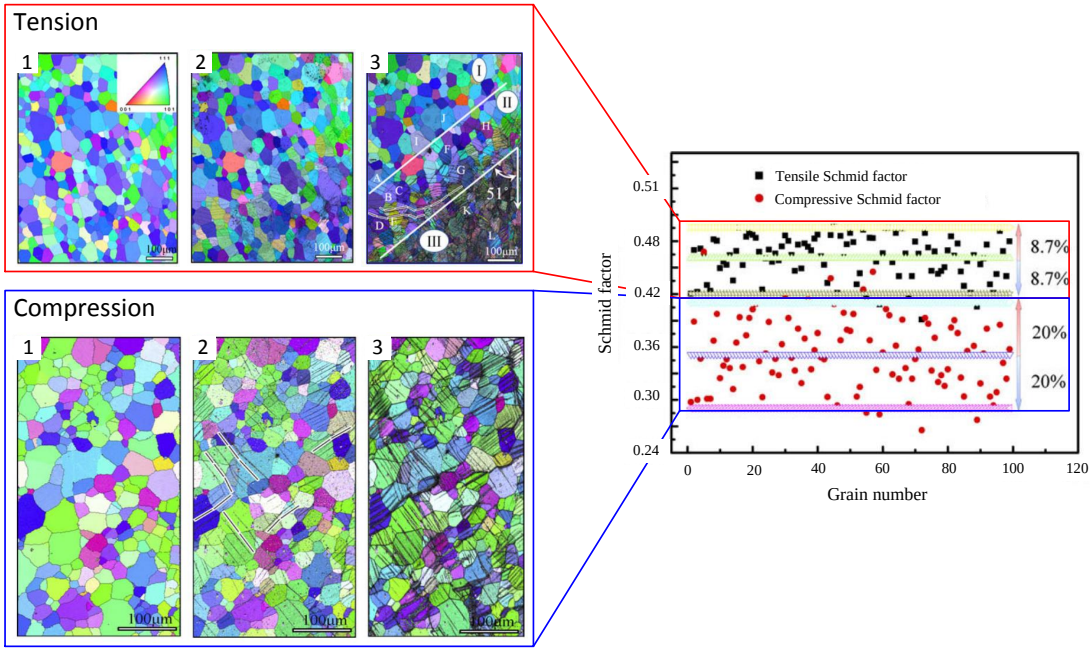

Figure 1.36: EBSD grain orientation maps of NiTi tubes submitted to tension and compression. The (1) maps show the samples before loading, in the austenite phase. In (2) and (3) different stages of loading are shown. The black lines are martensite plates. The graphic on the right side of the figure presents tensile and compressive Schmid factors calculated for 100 grains chosen randomly in the samples (adapted from Mao et al., 2010).

1.6.3.3 Localized necking theory applied in NiTi alloys

Despite its limitations, the theory of zero-extension-rate direction has been successfully used in the prediction of the band angle at appearance in NiTi alloys under uniaxial tension (Reedlunn et al., 2014; Shaw and Kyriakides, 1998). These authors evaluate the band angle appearing in NiTi SMA using an isotropic criterion.

Recently, Bechle and Kyriakides (2016) also used Hill theory to predict the angle of the localization band. The study was performed in a NiTi tube under biaxial load. The biaxial stress state was imposed by tensile load combined with internal pressure (see Fig. 1.37a). The ratio between axial (σ_x) and hoop (σ_θ) stresses is defined as

$$\alpha_b = \frac{\sigma_x}{\sigma_\theta} \tag{1.24}$$

The localization in the tube was analysed for several α_b values and the band angle from the axial direction was measured experimentally. The band angle measured in the test with $\sigma_\theta = 0$ was 55.8°. In the test with $\sigma_x = 0$ it was 29.1°, whose complement is near 55.8°.

The experimental angles were compared with Hill prediction using Eq. 1.22. In this equation were applied the von Mises isotropic criterion and an anisotropic criterion (CPB06 from the works of Cazacu et al. (2006) and Plunkett et al. (2008)). Both functions were calibrated with transformation stresses measured during tests.

Figure 1.37b shows measured and predicted band angles. The anisotropic yield criterion applied in Hill theory predicts the band angles fairly well.

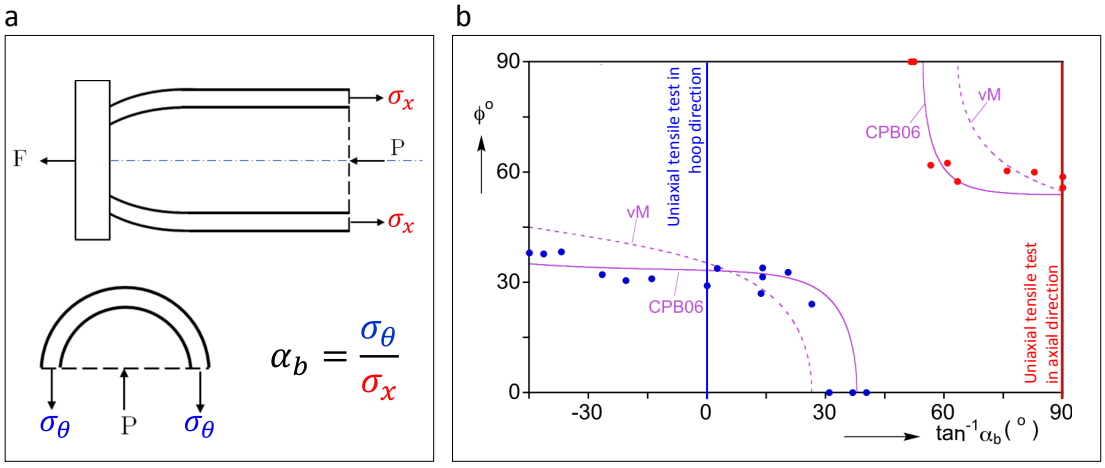

Figure 1.37: (a) Free body diagram of the tube during submitted to combined axial and hoop stresses (adapted from Linardon, 2014. (b) Relation between band angle ϕ and biaxial stress ratio α in a NiTi tube. The experimental results agree considerably well with the ones calculated using Hill theory and the anisotropic yield function calibrated with transformation stresses (adapted from Bechle and Kyriakides, 2016).

1.7 Conclusion

NiTi SMA are very good candidates for biomedical applications due to its exceptional thermomechanical behaviour. Mainly used in the manufacturing of medical devices, the alloy production always involves some type of mechanical forming process. These processes in turn induces a considerable amount of texture, causing the material to have significant anisotropy.

The many studies about texture in NiTi SMA help to elucidate important questions related to anisotropy. It has been shown that the mechanical behaviour of strongly anisotropic polycrystalline alloys closely resemble the behaviour of single crystals oriented similarly. The information about the mechanical behaviour of single crystals serves as guideline for the anisotropic behaviour of the polycrystalline alloy. However, it has also been shown that each type of mechanical forming process results in different orientation dependencies. Hence, as many studies have addressed the anisotropy in NiTi sheets, these results cannot be extended to tubes, a form whose anisotropy is still lacking on quantitative information.

In order to address the consequences of NiTi tube anisotropy in subsequent chapters, the thermodynamics of phase transformation and the mechanics of strain localization were considered. A thermodynamic framework was revised in which the material is treated as a two-phase system that undergoes a phase transformation away from the thermodynamic equilibrium. This analysis takes into account thermodynamic irreversibilities that are responsible for the behaviour of SMA.

Finally, the mechanics of localization is addressed under the light of plasticity theory. It has been discussed how the crystallographic and mechanical approaches to strain localization agree that this phenomenon is very sensible to the material texture and anisotropic behaviour.

CHAPTER

TWO

MATERIAL AND EXPERIMENTAL SET-UP

Contents

2.1 Introduction

To study the anisotropy of thin walled NiTi tubes an experimental campaign was defined and carried out. This chapter details this experimental procedure, from the fabrication of samples, to its thermomechanical characterization. The tensile tests were performed in samples cut at different orientations from the drawing direction of the tube.

Special care was taken to minimize the impact of the process of fabrication of samples on the original anisotropy of the tube. This chapter describes the technique adopted to cut the tube using laser machining. The final aim of this experimental campaign is to obtain strain fields over the surface of the samples when submitted to tensile tests, captured with Digital Image Correlation (DIC) technique.

2.2 Material

Thin walled NiTi tubes were chosen to conduct this study due to the more accentuated level of anisotropy of this form, compared to sheets. Furthermore, NiTi tubes have been widely used on an industrial scale for vascular stent manufacturing, which is reflected in the growing interest of the scientific community in this form in recent years.

The used NiTi tube has nominal composition 50.8%atNi-Ti. It was manufactured by Minitubes SA (France), obtained after the last cold mandrel drawing. Its dimensions are 8.27 mm of outer diameter D and 0.165 mm of wall thickness t, which gives an outer diameter to thickness ratio of 50.

2.3 Fabrication of Samples

2.3.1 Fabrication process of dogbone tensile samples

In order to study the anisotropy on the NiTi tube, oriented dogbone samples were cut from the tube. Firstly, the tube was longitudinally opened through laser cutting. After, the tube was flattened through a single step shape setting. Finally, once the tube was flattened, dogbone samples were laser cut in five orientations, including drawing (DD) and transverse directions (TD). Figure 2.1 illustrates schematically the five studied orientations, as well as the final dimensions of samples and the definition of reference coordinate systems.

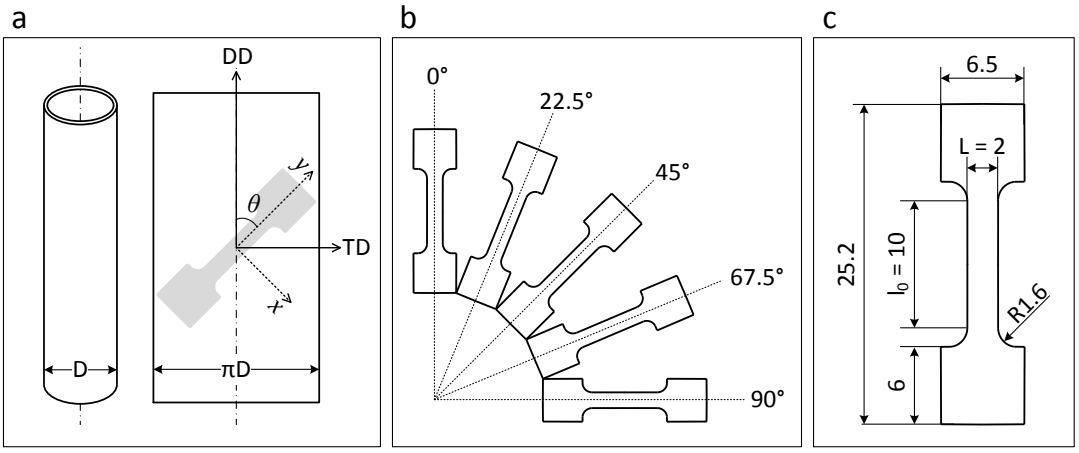

Figure 2.1: (a) Coordinate systems' nomenclature of the flattened tube and dogbone sample. (b) The five orientations at which the dogbone samples were cut, between drawing direction (0°) and transverse direction (90°). (c) Dimensions of the tensile samples in millimetres.

Figure 2.2 shows the NiTi tube in each of these steps. The shape setting and laser cutting processes are explained in details in the following sections.

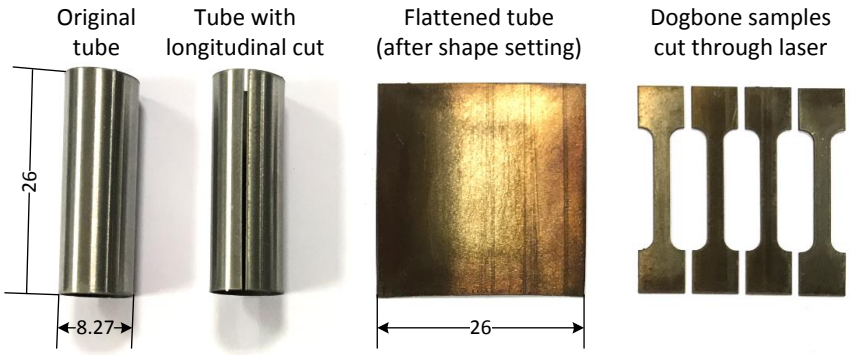

Figure 2.2: The thin walled NiTi tube in all steps of the fabrication of the dogbone samples. Dimensions are in millimetres.

2.3.2 Shape setting influence on thermal behaviour of samples

The shape setting process to flatten the NiTi tube was performed in a single step. The tube was opened between two stainless steel plates (see Fig. 2.3) and was put in a resistive furnace at 450°C for 20 min, followed by water quench. Argon gas flow was used as protective atmosphere against oxidation.

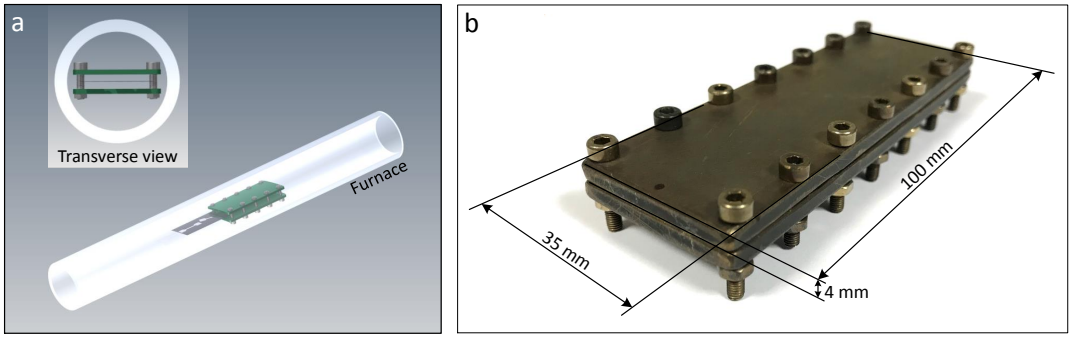

Figure 2.3: (a) CAD visualization of the plates inside the resistive furnace chamber. (b) Shape setting stainless steel plates.

The maximum bending strain ε_{bend} to flatten the tube was 1.9%. This value is calculated as shown in Fig. 2.4. It is very small compared to the amount of strain to which the material is submitted in the manufacture of the NiTi thin walled tube — 15% to 30% of section reduction per drawing pass (Linardon et al., 2014). Thus, it is expected that the shape setting process does not affect the overall behaviour of the tube. Furthermore, Robertson et al., 2006 shows that the flattening of a thin walled NiTi tube does not alter its pre-existing texture (see Fig. 1.15).

In order to evaluate the influence of the shape setting on the tube material, DSC tests on a Q200 model from TA Instruments were performed on the original and on the flattened tube. The temperature sweep was carried out between -60°C to 100°C with a 10°C/min rate. Fig. 2.5 presents these results. The original tube does not

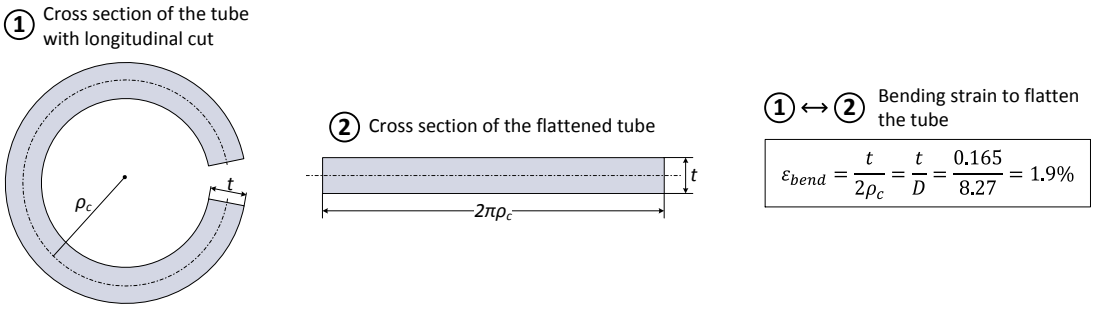

Figure 2.4: Mximum bending strain ε_{bend} to flatten a tube with thickness t and radius ρ_c.

present any transformation in this temperature range, while the flattened tube shows a small transformation peak. The small temperature hysteresis and small peak energy are indications that this transformation happens between austenite and R-phase. In order to evaluate the homogeneity of the "sheet", DSC samples were cut from various positions in the flattened tube, as shown in Fig 2.5. With regard to the temperature hysteresis, transformation enthalpy and transformation temperatures, the flattened tube is fairly homogeneous.

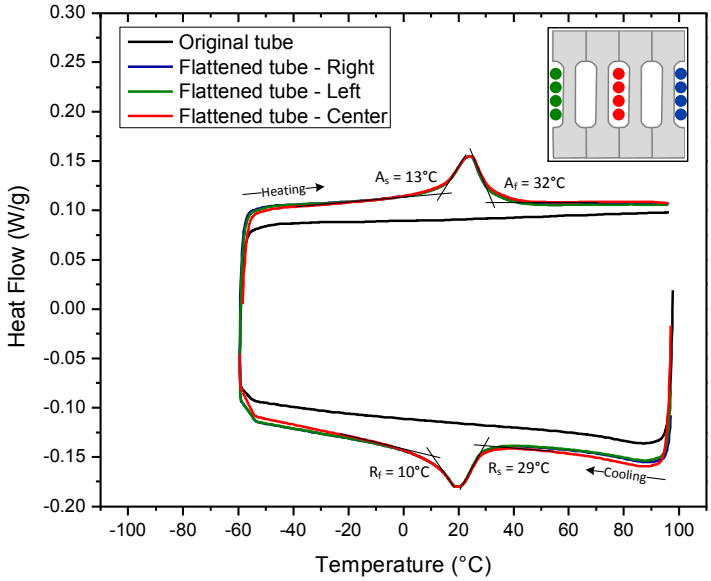

Figure 2.5: DSC results of the original and flattened tubes. The flattened tube was tested in various positions to verify the homogeneity of the "sheet".

2.3.3 Laser cutting

Tensile dogbone samples were obtained from NiTi flattened tubes by laser cutting. The available laser equipment is a marking laser system. The cutting process could be effectively performed because of the small dimension of the tube wall thickness. The

procedure used is explained in detail in the following subsections, after an overall review about cutting laser systems used in the fabrication of small NiTi components.

2.3.3.1 Brief review of NiTi laser cutting

Laser cutting is essentially a thermal process in which a material is removed through vaporization or melting, usually with the assistance of a gas flow to evacuate the removed material. It has the advantage of being remarkably precise compared to mechanical machining processes, leaving the cut material with a reduced heat affected zone (HAZ) and very good finishing. The thermomechanical properties of NiTi alloys, such as low thermal conductivity and low elastic modulus, make the mechanical machining difficult (Pfeifer et al., 2010). These alloys were specially favoured with the development of laser cutting, which has been essential to the success of miniaturized devices such as vascular stents and micro-electro-mechanical systems (MEMS).

Regarding the activation time of the laser beam, laser cutting systems can be divided in continuous and pulsed systems. Literature shows that pulsed systems are preferred to obtain miniatured devices from NiTi alloys. This is due to the minimum thermal impact on the material. Besides, pulsed laser cutting results in extreme good cutting quality and width control of the kerf (width of material that is removed by a cutting process) (Pfeifer et al., 2010).

Pulsed laser systems can be categorized based on the range of pulse width (duration of the pulse) as long, short and ultrashort lasers. The shorter the pulse width, the minimum is the HAZ, being practically non-existent for ultrashort lasers like picosecond and femtosecond lasers. This consists in a huge advantage, seen that no post-processing for removing HAZ is necessary, besides the improved surface topography. However, ultrashort lasers have lower cutting speed due to low material remove rate and therefore have limited applications on industrial scale manufacturing (Liu et al., 2016).

In the manufacturing of stents, long pulse width lasers like Nd:YAG (neodymium-doped yttrium aluminum garnet) and fiber lasers are more commonly used. Cutting with these systems results in the presence of a recrystallization zone (HAZ) of the order of 1 μm to 100 μm, depending on the chosen laser parameters (Liu et al., 2016; Pfeifer et al., 2010). Pfeifer et al., 2010 observed that for a given pulse energy E_p the HAZ size after cutting NiTi with Nd:YAG laser is smaller for larger pulse widths (see Fig. 2.6). Liu et al., 2016 reported that no significant difference in HAZ size was observed using different parameters to cut a NiTi tube in a fiber laser. The HAZ size was about 5μm large. However, ther cuts were performed using water flow inside the tube in order to increase heat dissipation, which certainly contributes to minimize the HAZ. Overall, comparisons between both systems show that fiber lasers achieve better kerf quality in terms of width, roughness and HAZ size (Kleine and Watkins, 2003; Meng et al., 2009).

2.3.3.2 Particularities of the procedure used to laser cut the NiTi tube and dogbone samples

The laser system used to cut the dogbone samples from the flattened NiTi tube was a marking laser system, model Easymark F20 from Rofin. It is a pulsed fiber laser with wavelength of 1070 ± 5 nm. The pulse width is fixed in 5μs, the nominal maximum power is 18 W, and the pulse frequency ranges from 20 to 100 kHz. The material is removed by

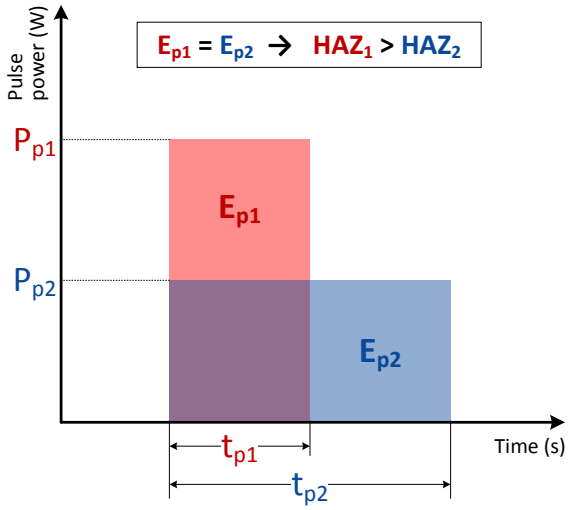

Figure 2.6: Pulser laser parameters, illustrating Pfeifer et al., 2010 results about the relation between HAZ size and pulse width (t_p). For the same pulse energy (E_p) the HAZ is smaller for larger t_p values.

ablation at ambient condition (no protective gas flow). The removed material is cleaned by a vacuum system. The laser beam is fixed at the top part of the marking chamber and can move covering a solid angle so that the laser spot can sweep an 120 mm x 120 mm x 120 mm volume. This model can perform laser markings/cuttings on planar or curved surfaces. In the first case the material to be marked/cut is positioned on the chamber table surface. For curved surfaces, the material is clamped on a rotatory mandrill. A CNC system controls the z axis position of the table and the angular position of the mandrill.

Because this is primarily a marking system, the maximum pulse energy is rather small. For that, in order to cut the NiTi material, the software was programmed to perform multiple laser passes over a hatch around the desired shape. The laser and hatch parameters used are listed on Table 2.1.

Table 2.1: Pulse laser parameters used to cut the NiTi tube material

Laser parameters						Hatch parameters	
Pulse width t_p (μs)	Pulse power P_p (W)	Pulse energy E_p (μJ)	Pulse Frequency f_p (kHz)	Cutting speed v_c (mm/s)	Spot diameter ϕ_{spot} (mm)	Width w_{hatch} (mm)	Number of passes -
5	3.6	18	20	200	0.02	0.1	150

These parameters were chosen in order to minimize the HAZ and to achieve a good finishing, according to the literature reports cited in section 2.3.3.1. To help heat dissipation, aluminium pieces were put in contact with the NiTi surface during cutting process. Figure 2.7 shows the laser chamber with the flattened tube (planar surface) and original tube (curved surface) prepared to be cut.

A study was conducted to verify the influence of the laser cutting on the tensile behaviour of the tube and to help decide the sample width. The next section explains in more detail the methodology used in this study as well as its conclusions.

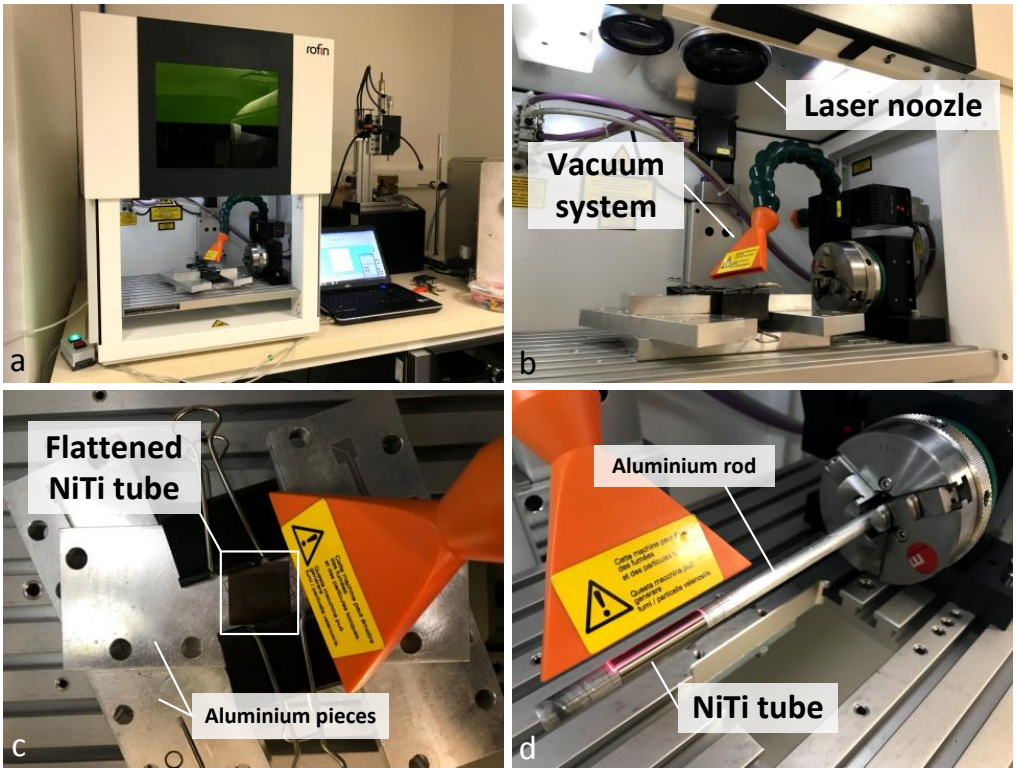

Figure 2.7: (a) Easymark F20 marking laser system. (b) Laser marking/cutting chamber. (c) Flattened tube positioned prior to dogbone sample cutting. (d) NiTi tube positioned to be cut longitudinally, prior to shape setting.

2.3.3.3 Influence of laser cutting on the tensile behaviour

For comparison purposes, the dogbone samples cut in all five orientations (see Fig. 2.1b) must have the same dimensions. The samples' length is then limited by the sample cut in the circumferential direction. In order to keep the samples' aspect ratio (length/width) as high as possible, the width must be the smaller possible. However, the laser cutting leaves a HAZ which could only be minimized but not eliminated.

Therefore, a brief investigation concerning the effects of laser cutting was carried out prior to the anisotropy study in the tube. The main objective is to define the minimum tensile sample width with a minimum influence of the HAZ on mechanical behavior. In this preliminary study it was used a Ni-rich 0.35 mm thick NiTi sheet ($A_{f_{sheet}}$ = -5°C). Since the tube is more than twice thinner than this sheet, heat is more easily dissipated during cutting. Thus, it is expected the HAZ in the tube material to be even smaller than in this sheet.

Firstly, in order to homogenize the microstructure, the sheet was submitted to an annealing at 800°C for 30 min followed by an aging at 400°C for 30 min, both followed by water quench. From the homogenized sheet, four dogbone samples with different widths L (1, 1.4, 2.2 and 2.8 mm) were cut by laser using the parameters on Table 2.1. These

four dogbone samples were subjected to quasi static tensile tests at 60°C.

Figure 2.8 presents the tensile behaviour of these samples. It was concluded that widths larger than 1.4 mm do not present significant change in mechanical behavior and the width of L = 2 mm was chosen to the study of tube anisotropy. This width allows good strain field measurement with digital image correlation technique.

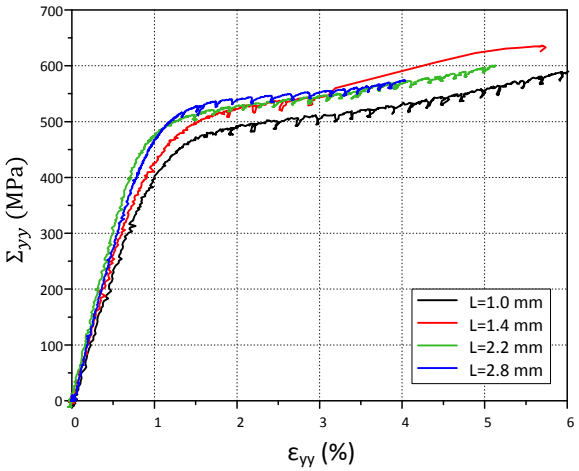

Figure 2.8: Results of tensile tests performed on a 0.35 mm NiTi sheet in order to evaluate the laser influence on the NiTi mechanical behaviour. Σ_{yy} is the nominal longitudinal stress and ε_{yy} is Hencky longitudinal strain.

2.4 Experimental Set-up

Quasi static isothermal tensile tests were performed on the oriented samples. Tensile tests were carried out in a Gabo Explexor 500N equipment under displacement control. Tests were carried out in four temperatures to allow the evaluation of the anisotropy temperature dependency of the material. Testing temperatures were chosen so that at the start of tensile tests samples had an austenite microstructure, based on the DSC results presented in Fig. 2.5. The chosen temperatures were 40°C, 50°C, 60°C and 70°C. Each sample was submitted to only one tensile test. Prior to the isothermal tensile tests, the dogbone samples were heated in boiling water for 1 min, so that all structure was austenitic, and cooled to room temperature to ensure that all samples start tests with the same structure.

After the completion of a superelastic cycle, samples were loaded until rupture. Figure 2.9 shows the stress profile applied, where $\Sigma_{yy} = F/A_0$ is the nominal stress applied in the longitudinal direction of the sample, with F being the axial force and A_0 the initial cross section area of the sample. The nominal stress level attained at the end of the superelastic cycle was dependent on the test temperature to allow the sample to attain approximately the same strain level at all temperatures. Furthermore, the Cauchy (or true) stress is calculated as $\sigma_{yy} = F/A$ where A is the current cross section area, obtained from the hypothesis of volume conservation (Otsuka and Ren, 2005): $A = A_0(l_0/l)$, with

l_0 and l being the initial and current gauge sample lengths, respectively. l_0 = 10 mm and A_0 = sample width (L) x sample thickness = 2 × 0.165 mm^2. A strain rate of $5 \times 10^{-4} s^{-1}$ was used, which was slow enough to avoid the effects of self heating (Elibol and Wagner, 2015).

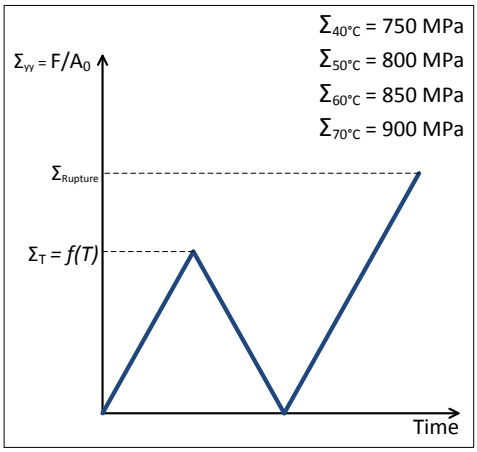

Figure 2.9: Profile of nominal stress applied on the tensile tests.

Strain data acquisition was performed by digital image correlation technique. Figure 2.10a shows a representative example of the specular pattern on the surface of a sample. A black speckle was applied on a white background. The zone of interest (ZOI) has around 200 x 1000 pixels. The speckle allowed a 29 px x 29 px subset to be used in the correlation analysis, performed with Vic2D software from Correlated Solutions. The digital image scale is 0.01 mm/pixel.

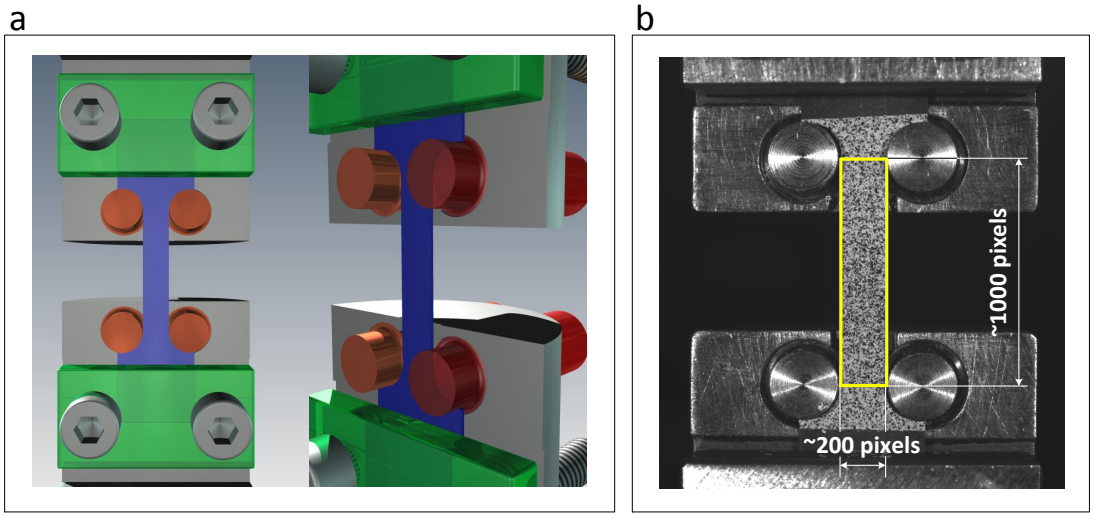

Figure 2.10: (a) Clamping system in CAD, showing in more detail the cylinders used to prevent slipping. (b) Example of speckle pattern used to measure strain maps on the sample surface, with the dimension of the zone of interest in pixels.

The DIC analysis provides longitudinal, transverse and shear strain maps of the sam-

ple surface (see Fig. 2.1 for reference frame nomenclature). The strain maps correspond to the components of the Hencky strain tensor $\varepsilon_{xx}(M)$, $\varepsilon_{yy}(M)$ and $\varepsilon_{xy}(M)$ in function of the material point M. To plot the global mechanical behaviour, strain was averaged over the interest zone (yellow rectangle) shown in Fig. 2.10a at each instant.

2.5 Conclusion

To study the anisotropy of the NiTi tube, it was shape set into a sheet form and then tensile samples were laser cut in five orientations between drawing and transverse directions. The influence of the shape setting and the laser cutting was analysed.

The shape setting parameters can be considered mild (450°C for 20 min) and, besides, it was performed in one single step. It did release the superelastic behaviour in the originally cold-worked material, as seen in the DSC result. However, literature reports confirm that not even strong heat treatments are capable of erasing the anisotropy caused by deep mechanical forming, as is the case of NiTi thin walled tubes (Robertson et al., 2006). With this, it can be safely presumed that the anisotropy of the samples fabricated through this shape setting process do not significantly differ from the original anisotropy of the tube.

The laser cut was used to open the tube for the shape setting and, after, to cut the dogbone tensile samples from the flattened tube. The cut process was performed with a marking machine equipped with a pulsed laser system. Its maximum available pulse energy is a lot smaller than in laser systems specific for cutting. Because of that, the cut was performed by repeatedly applying the laser beam with low intensity pulse parameters. This cutting method, although more time-consuming, cause very little heating, which reduces the HAZ. Nevertheless, a brief study was conducted and the laser cut effect was minimized with the choice of a minimum sample width of 2 mm.

The tensile tests performed in the oriented samples give valuable information about the anisotropic state of the NiTi tube. As discussed in the next chapters, global and local behaviours can be extracted from the DIC strain fields, with data of longitudinal, transverse and shear deformations. Because the tensile tests were carried out at four temperatures for each oriented sample, both anisotropy and temperature dependencies can be evaluated.

CHAPTER

THREE

ANISOTROPY OF THE TEMPERATURE DEPENDENCE IN THE SUPERELASTIC BEHAVIOUR OF NiTi THIN WALLED TUBES: EXPERIMENTS AND THERMODYNAMIC ANALYSIS

This chapter is written in the form of an article to be published soon. Because of that, it contains sections summarizing the experimental set-up (presented in chapter 2) and the thermodynamic approach (presented in chapter 1). Its main objective is to examine the anisotropy of thermomechanical properties related to phase transformation, especially to the superelastic effect: transformation strain, transformation stresses, stress hysteresis and Clausius-Clapeyron coefficients. These properties are extracted from tensile stress-strain curves in four temperatures. The temperature dependence is evaluated and conclusions are drawn based on the performed thermodynamic analysis.

Contents

3.1 Introduction

Nickel-Titanium (NiTi) alloys are the most successful Shape Memory Alloys (SMA). They have the remarkable ability to totally recover strains of the order of 10% in tension. This recovery can happen either by heating, known as the shape memory effect, or by simple mechanical unloading, effect known as superelasticity. In many areas NiTi alloys are a prosperous composition family of SMA. They are remarkably suitable for biomedical applications due to their outstanding transformational properties, biocompatibility, good corrosion resistance in physiological environments and for being much more mechanically compatible with human tissues than the traditional stainless steels (Duerig et al., 1999; Jani et al., 2014; Ryhänen et al., 1998).

NiTi alloys have increasingly been used in the form of thin walled tubes for the fabrication of catheters and self-expanding stents. A review about evolution in stents design (Bonsignore, 2004) showed that of all self-expanding stents, 90% use NiTi alloys as material. They take advantage of the NiTi superelasticity for the stent implantation. The review also showed that 65% of self-expanding stents are manufactured from thin walled tubes cut by laser. The thin walled NiTi tubes need to be manufactured with very good dimensional accuracy and surface finish to be used in the fabrication of stents. These prerequisites can be more satisfactorily met from cold tube drawing processes with the use of a mandrel (Poncin and Proft, 2003). This process involves initially hot drawing of a hollow rod and a subsequent series of cold mandrel drawing to progressively reduce thickness. The cold work is intermediated with short annealing heat treatments to recover workability and allow further processing (Favier et al., 2006; Linardon et al., 2014; Palengat et al., 2013). During the drawing process, the microstructure of the NiTi alloy becomes highly textured.

Superelasticity and shape memory effect in NiTi SMA are associated with a stress or temperature induced phase transformation of its crystalline structure. The so-called martensitic phase transformation takes place through ordered atomic movement. Therefore, any significant alignment of crystallographic grains directly affects the mechanical behaviour of the material and the more texturized the alloy, more anisotropic it is. A considerable amount of experimental work can be found in literature about texture in NiTi sheets and its associated anisotropy (see for example Gao and Yi (2003), Inoue et al. (1996), Liu et al. (1999), and Liu (2015)). However, as analysed by Robertson et al. (2005), drawn tubes and rolled sheets have very distinct textures. Indeed the authors showed that the resulting texture is strongly dependent on the forming process. Hence the several studies about the anisotropic mechanical behaviour of sheets do not apply to the case of tubes.

Literature works concerning the quantification of anisotropy of superelastic behaviour of NiTi tubes are scarce. To the best of the authors' knowledge, only two works directly access the mechanical tensile behaviour in different orientations of NiTi tubes. Barney et al. (2011) performed X-ray microdiffractions on micrometric tensile samples cut from a tube in the longitudinal (0°) and circumferential (90°) directions and at 45°. They showed that 0° and 45° samples have predominantly ⟨111⟩ and ⟨100⟩ type grains orientations, respectively, along the deformation axis. Through a microstructural phase and strain analysis they showed that the mechanical behaviour at 45° greatly differs from the other two studied directions. The other work, from Robertson et al. (2006), calculated the theoretical transformation strains of twelve variants of martensite from texture data of drawn tubes. It resulted in the prediction of macro transformation strains in several loading orientations relative to the drawing axis. Their predictions showed that at 45° the attained strain is smaller than in the longitudinal and circumferential directions. No work access the anisotropy of the temperature dependence.

In this context, this work investigates and analyses the anisotropies of the superelastic behaviour and of the temperature dependence of a thin walled NiTi tube. Firstly, an experimental investigation is carried out in order to address the anisotropy of the thermomechanical behaviour of the tube's material. The original tube is flattened and samples cut along five orientations from the drawing direction are cut. The samples are submitted to isothermal tensile tests at several temperatures above A_f. The experimental results obtained at each orientation allow the calculation of key SMA properties and a clear quantitative analysis of anisotropy. Afterwards, the observations from this first part are examined from a thermodynamic point of view. This thermodynamic analysis addresses the anisotropy of energy terms involved in a transformation cycle. The anisotropy of the temperature dependence of these energy terms is also analysed, a dependence which is typically neglected.

3.2 Material and methods

3.2.1 NiTi tube and fabrication of tensile samples

A 50.8%atNi-Ti thin walled tube of outer diameter = 8.27 mm and wall thickness = 0.165 mm was used. This tube was manufactured by Minitubes SA (France). Figure 3.1 shows a scheme of the fabrication process of the tensile samples, together with samples' final dimensions and nomenclature used in this work. The original tube was a tube obtained after the last cold mandrel drawing. A section of this original tube was first cut longitudinally using a pulsed optical fibre laser. This tube section was then flattened through a one-step shape setting at 723 K (450°C) for 20 min in a resistive furnace followed by water quench. The maximum strain to flatten the tube in a "sheet" form was about 2.1% (in absolute value). This is negligible when compared to the strain to which the material is subjected in the manufacturing process of the tube from the ingot. From the flattened tube, dogbone samples were laser cut in five different orientations: $\theta = 0°$ (drawing direction-DD), $\theta = 22.5°$, $\theta = 45°$, $\theta = 67.5°$ and $\theta = 90°$ (transversal direction-TD). The $\vec{e_y}$ and $\vec{e_x}$ directions correspond to the longitudinal and transverse directions of the dogbone samples, respectively.

Differential Scanning Calorimetry (DSC) analysis (model Q200 from TA Instruments)

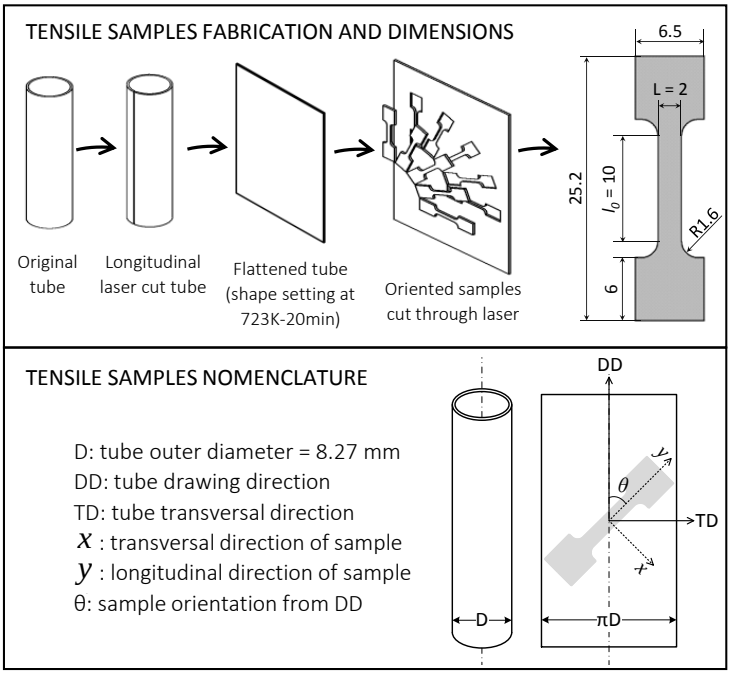

Figure 3.1: Scheme of fabrication process of dogbone tensile samples from NiTi tube, the final dimensions of samples and adopted nomenclature.

was performed in samples of both original and flattened tubes. This technique was used to verify the effects of shape setting process in the transformation behaviour of the tube. The analysis was carried out between 373 K and 213 K with a 10 K/min rate. Figure 3.2 presents the DSC results for both original and flattened tubes.

The curve for the original cold-worked tube does not indicate the presence of phase transformation. The curve for the flattened tube presents two peaks during cooling and heating. They are associated with Austenite to R-phase transformation (A→R), since little peak energy ($\approx$ 4.3 J/g) and small temperature hysteresis ($\approx$ 5 K) are observed (Otsuka and Wayman, 1998; Zheng et al., 2008). Transformation temperatures were extracted by slope-line-extension method and are: R_s = 302 K; R_f = 283 K; A_s = 286 K; A_f = 305 K.

Robertson et al. (2006) used a flattening process similar to the above process. They showed that there is no significant texture difference between the NiTi tube and a sample cut from a flattened tube. Moreover, they showed that the texture of NiTi tube is not altered when submitted to strong heat treatments. On the contrary, the texture is intensified by the heat treatements.

3.2.2 Isothermal tensile tests

The dogbone samples were subjected to isothermal, strain controlled tensile tests in a Gabo Eplexor 500N testing machine at a strain rate of 5×10^{-4} s^{-1}. Tests were performed at four temperatures: 313 K (40°C), 323 K (50°C), 333 K (60°C) and 343 K (70°C), as indicated in Fig. 3.2. Different oriented samples were used for tests at each temperature. The tensile tests consisted of loading to a stress set point, followed

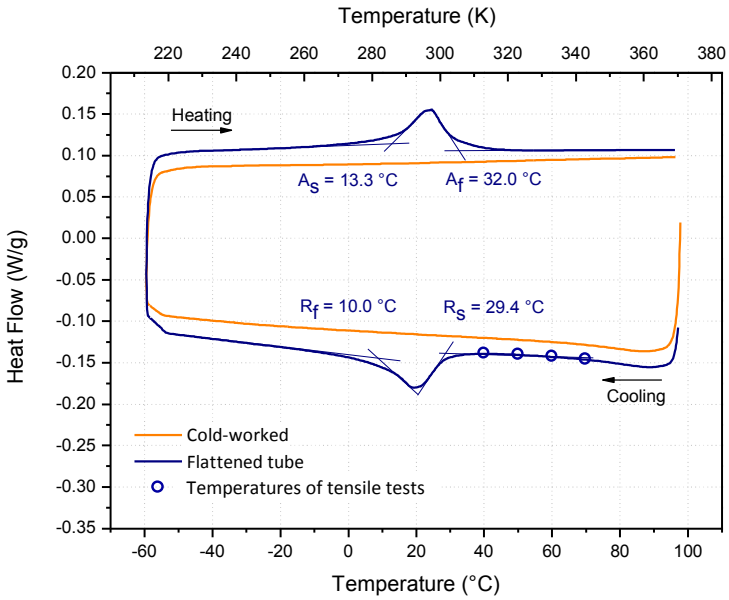

Figure 3.2: DSC results for the original tube (cold-worked) and for flattened tube (after shape setting at 723 K for 20 min).

by unloading to zero force. The stress set points were chosen differently for each testing temperature to allow the observation of mechanical response after the end of stress plateau. They were: 750 MPa, 800 MPa, 850 MPa and 900 MPa for the tests at 313 K, 323 K, 333 K and 343 K, respectively. An additional loading until rupture was performed for the tests at 313 K, 323 K and 333 K. Prior to each test the samples were heated in boiling water for some minutes and subsequently cooled by natural convection before being exposed to the testing temperature. Testing temperature was imposed with an accuracy of ± 1 K by the resistive air furnace of the machine, which has fanned convection.

The furnace lid contains a transparent crystal window, allowing strain measurement with 2-D Digital Image Correlation (Digital Image Correlation). This is a non contact measurement technique that provides the strain maps over the surface of a sample. This is performed through search and track algorithms applied to the digital images captured at constant intervals during specimen deformation. In our study the Vic2D software from Correlated Solutions was used. The strain maps correspond to the longitudinal $\varepsilon_{yy}(M)$ and transverse $\varepsilon_{xx}(M)$ and shear $\varepsilon_{xy}(M)$ components of the Hencky strain tensor in function of the material point M.

In this work, logarithmic tensile strain ε_{yy} at each instant is calculated as the mean of ε_{yy}(M) inside an observation zone in the sample gauge area. Axial nominal stress is calculated as $\Sigma_{yy} = F/A_0$ where F is the axial force and A_0 is the initial cross section area (A_0 = sample width (L) $\times$ sample thickness = 2 $\times$ 0.165 mm^2). Cauchy (or true) stress is calculated as $\sigma_{yy} = F/A$ where A is the current cross section area. A is obtained from the hypothesis of volume conservation ($A = A_0/e^{\varepsilon_{yy}}$).

3.3 Thermodynamic framework of thermoelastic martensitic transformation

This section aims to provide a background on the thermodynamic framework used in this work to calculate and discuss some of the analysed properties. The approach used in this article is based on the works of Ortín and Planes (Ortín and Planes, 1988, 1991, 1989) and Wollants et al. (1993). The martensitic transformation is considered as a solid-to-solid, diffusionless, first order, reversible transition.

This approach is expressed at the scale of a representative element volume (REV). The free energy change dG per unit mass of REV over an infinitesimal step f_m of transformation for a thermoelastic martensitic transformation in a polycrystalline matrix is expressed as (Ortín and Planes, 1989; Wollants et al., 1993):

$$dG = (\Delta H_{ch} - T\Delta S_{ch})df_m + \delta E_{st} + \delta E_{fr} - \delta W^{tr}_{mech} = 0 \tag{3.1}$$

where:

- f_m is the mass fraction of martensite, defined in the REV. In full austenitic state $f_m = 0$, in full martensitic state $f_m = 1$ and infinitesimal steps are $0 \leq df_m \leq 1$;
- ΔH_{ch} is the specific enthalpy of transformation per mass unit of transforming material, understood as the difference between the two chemical specific enthalpies of the martensite and austenite phases: $\Delta H_{ch} = H^M_{ch} - H^A_{ch}$;
- ΔS_{ch} is the specific entropy of transformation per mass unit of transforming material, understood as the difference between the two chemical specific entropies of the martensite and austenite phases: $\Delta S_{ch} = S^M_{ch} - S^A_{ch}$;
- T is temperature;
- δE_{st} accounts for the elastic energy stored in the REV by an infinitesimal step df_m of the transformation at the stage corresponding to f_m;
- δE_{fr} accounts for the energy dissipated by the infinitesimal step df_m of transformation at the stage corresponding to f_m;
- δW^{tr}_{mech} represents the external mechanical work per unit mass of the REV required to induce the infinitesimal step of transformation at the same stage.

The occurrence of a stress induced martensitic transformation is determined when the Gibbs free energy of the REV (G) reaches a minimum, which is expressed by the condition ($dG = 0$). In derivative form, this condition results in:

$$G' = \frac{\partial G}{\partial f_m} = \Delta H_{ch} - T\Delta S_{ch} + E'_{st} + E'_{fr} - W'^{tr}_{mech} = 0 \tag{3.2}$$

where:

- G' is defined by $dG = (\partial G/\partial f_m)df_m = G'df_m$;
- $\delta E_{st} = (\delta E_{st}/\delta f_m)df_m = E'_{st}df_m$;

- $\delta E_{fr} = (\delta E_{fr}/\delta f_m)df_m = E'_{fr}df_m$;
- $\delta W^{tr}_{mech} = (\delta W^{tr}_{mech}/\delta f_m)df_m = W'^{tr}_{mech}df_m$.

In Equation 3.2, all terms are expressed as energy per unit mass of transforming material in J/kg and are algebraic values. The infinitesimal martensite mass fraction step df_m is positive during forward transformation (austenite to martensite, A→M) and negative during reverse transformation (martensite to austenite, M→A).

The specific **enthalpy and entropy changes**, respectively, ΔH_{ch} and ΔS_{ch}, originate from the difference in atomic arrangement between the two phases. They are both considered constant for a given transformation in a given alloy system. $H^M_{ch} < H^A_{ch}$ and $S^M_{ch} < S^A_{ch}$, leading to $\Delta H_{ch} = H^M_{ch} - H^A_{ch} < 0$ and $\Delta S_{ch} = S^M_{ch} - S^A_{ch} < 0$. Also, the heat capacities of austenite and martensite are assumed equal (Delobelle, 2012; Wollants et al., 1993).

The **stored strain energy** term, δE_{st}, includes the elastic energy associated with the accommodation of the shape and volume changes of the transformation. This energy is stored in the system during the forward transformation ($\delta E_{st} > 0$) and progressively released with the reversion of martensite to the parent phase ($\delta E_{st} < 0$). As $df_m > 0$ during forward transformation (A→M) and $df_m < 0$ during reverse transformation (M→A), $E'_{st} > 0$ for both forward and reverse transformations.

The **dissipated energy** term, δE_{fr}, is the sum of all energies consumed during phase transformation. It includes frictional work associated with the moving of internal defects and transformation phase boundaries (Wollants et al., 1993). As δE_{fr} is always dissipated, its value is always positive for both forward and reverse transformations. As $df_m > 0$ during forward transformation (A→M) and $df_m < 0$ during reverse transformation (M→A), $E'_{fr} > 0$ for the forward transformation and $E'_{fr} < 0$ for the reverse transformation.

The **external mechanical work**, δW^{tr}_{mech}, is expressed as function of the macroscopic strain and stress tensors at the level of the REV, according to continuum mechanics theory. In a tensile test the external mechanical work per unit mass is accounted as $\delta W_{mech} = \frac{1}{\rho}\sigma d\varepsilon$. The volumetric mass density, ρ, is considered in this work as $\rho = 6450$ kg/m^3, σ is the applied tensile Cauchy stress (or true stress) and $d\varepsilon$ is the increment of logarithmic strain. If plastic deformation is negligible, the strain increment can be divided in two summands, an elastic strain increment and a transformation strain increment:

$$d\varepsilon = d\varepsilon_{el} + d\varepsilon_{tr} \tag{3.3}$$

From this division the external mechanical work can be written as:

$$\delta W_{mech} = \delta W^{el}_{mech} + \delta W^{tr}_{mech} \tag{3.4}$$

Which gives the external mechanical work to induce transformation

$$\delta W^{tr}_{mech} = \frac{1}{\rho}\sigma d\varepsilon_{tr} \tag{3.5}$$

In this paper, the increment $d\varepsilon_{tr}$ is assumed proportional to the infinitesimal step df_m (Pelton et al., 2015): $d\varepsilon_{tr} = df_m \Delta\varepsilon_{tr}$, where $\Delta\varepsilon_{tr}$ is the tensile transformation strain

for a complete transformation. Thus, $W'^{tr}_{mech} = \frac{1}{\rho}\sigma\Delta\varepsilon_{tr}$. Therefore, for a tensile test, Eq. 3.2 reads:

$$G' = \Delta H_{ch} - T\Delta S_{ch} + E'_{st} + E'_{fr} - \frac{1}{\rho}\sigma\Delta\varepsilon_{tr} = 0 \tag{3.6}$$

Now, isolating the tensile Cauchy stress in Eq. 3.6 one obtains:

$$\sigma = \frac{\rho}{\Delta\varepsilon_{tr}}[\Delta H_{ch} - T\Delta S_{ch} + E'_{st} + E'_{fr}] \tag{3.7}$$

Equation 3.7 dictates the energy balance of the thermodynamic system (constituted by the two-phase transforming material) at each σ, T pair. While the enthalpy and entropy changes are function of composition only, the terms of transformation strain, storage and frictional energies can be function of martensite fraction and temperature.

Differentiating Eq. 3.7 with respect to temperature the general form of the Clausius-Clapeyron relation is obtained. At a given martensite fraction f_m:

$$\frac{d\sigma}{dT} = \frac{\rho}{\Delta\varepsilon_{tr}}\left(-\Delta S_{ch} + \frac{\partial E'_{st}}{\partial T} + \frac{\partial E'_{fr}}{\partial T}\right) - \frac{\sigma}{\Delta\varepsilon_{tr}}\frac{\partial\Delta\varepsilon_{tr}}{\partial T} \tag{3.8}$$

In Eq. 3.8 the terms of transformation strain, stored and dissipated energy are often assumed to be independent of temperature. Then, the classic Clausius-Clapeyron relation is obtained, where C is the Clausius-Clapeyron coefficient for a given phase transformation:

$$C = \frac{d\sigma}{dT} = -\frac{\rho\Delta S_{ch}}{\Delta\varepsilon_{tr}} \tag{3.9}$$

3.4 Experimental results

Figure 3.3 contains a set of Σ_{yy}-logarithmic ε_{yy} strain curves for five orientations θ and four testing temperatures T. For clarity purposes, the last loading up to rupture is omitted in this figure and is presented further in the article (see Fig. 3.6). Perfect superelastic behaviour is observed for all orientations and testing temperatures, with negligible residual strain after unloading.

The curves in Fig. 3.3 show that the strain achieved at the end of loading varies with orientation, as well as the plateau stress, although to a lesser extent. Unlike the other orientations, it is notable that at $\theta = 45°$ the material does not present a well-defined stress plateau. The absence of a plateau is an indication of a non-localized deformation (Bechle and Kyriakides, 2016; Šittner et al., 2005), which was confirmed through the strain maps of DIC (presented in Chapter 4).

The testing temperature has little influence on the strain levels. Stress levels rise with testing temperature for all orientations, as expected in NiTi alloys according to the Clausius-Clapeyron relation.

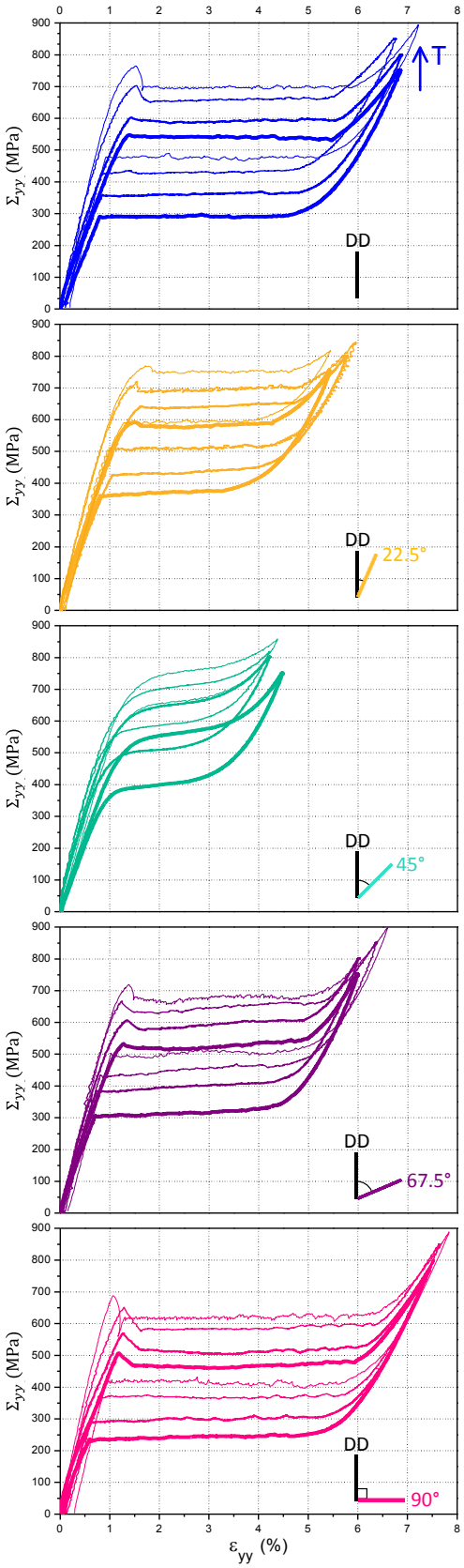

Figure 3.3: Nominal tensile stress versus logarithmic strain plotted for each orientation at 313 K, 323 K, 333 K and 343 K. The thickness of the line decreases with increasing temperature.

3.5 Discussion

In this section thermomechanical key properties of NiTi are presented and discussed. A quantitative analysis of the anisotropic behaviour of transformation strain, stress, stress hysteresis and Clausius-Clapeyron coefficients is performed. The methodology used for calculations is presented along with the property itself.

3.5.1 Qualitative analysis of the anisotropy of mechanical behaviour

From the stress-strain curves of Fig. 3.3 it is possible to qualitatively infer a strong anisotropy in the mechanical behaviour of the NiTi tube. The strains at the end of loading are very dependent on the orientation. The plateau stresses are to a less extent also orientation dependent. The overall observation is that the mechanical behaviour evolves almost symmetrically from 0° and 90° directions towards 45°.

The shape of stress-strain curves at 45° from the drawing direction is very distinct compared to the other orientations. Besides reaching the smaller strain at the end of loading, this orientation has a very smooth mechanical behaviour with some degree of hardening. The origin of this distinct mechanical behaviour is attributed to the texture induced by the drawing process of the tube (Robertson et al., 2005, 2006). Texture measurements performed by Barney et al. (2011) in a NiTi tube flattened through a shape setting process show that a specimen cut along the 45° orientation contains predominantly ⟨100⟩-type grains.

Indeed the tensile behaviour of ⟨100⟩ NiTi single crystals measured by Gall et al. (1999) resembles those of Fig. 3.3 for the 45° orientation. The authors show that ⟨100⟩-type grains present strong transformation hardening under tension, which seems to hinder the stress-induced martensitic transformation compared to other single crystal orientations, as well as cause early rupture. Therefore, less transformation strain is observed in this direction.

Another feature of the anisotropy of NiTi tubes observed in the results of Fig. 3.3 is the symmetrical tendency of mechanical behaviour from 45° orientation towards drawing and transversal directions (0° and 90°). In both senses – from 45° to 0° and from 45° to 90° – the strain at the end of loading increases and the plateau stress decreases for tests at the same temperature. Barney et al. (2011) and Bechle and Kyriakides (2016) also pointed out the similarities of mechanical behaviour between drawing and transversal directions in NiTi tubes. According to texture measurements, samples cut from thin walled NiTi tubes along the drawing direction have predominantly ⟨111⟩ grains (Barney et al., 2011; Robertson et al., 2006), while samples cut along the transversal direction have a mix of ⟨111⟩ and ⟨110⟩-type grains (Robertson et al., 2006). The tensile tests in NiTi single crystals performed by Gall et al. (1999) show that both ⟨111⟩ and ⟨110⟩ grains reach substantial larger strains than ⟨100⟩ grains at the same stress level, besides presenting a well-defined stress plateau.

3.5.2 Anisotropy of the austenite elastic modulus (E)

The estimation of elastic modulus of a transforming material from a stress-strain curve can be rather inaccurate. This happens because, associated to pure elasticity, other mechanisms of deformation are involved in the deformation process. In the case of NiTi the phase transformation, martensite reorientation and/or plasticity may contribute to lower the measured elastic modulus. Liu and Xiang (1998) analysed the measurement of elastic modulus from stress-strain curves of a near-equiatomic NiTi alloy. As a conclusion the authors suggested that the largest value ever measured should be taken into account. Therefore, the true value of E will always be expected to be greater than the typical measurements from stress-strain curves.

Following this reasoning, the elastic modulus E of the austenite is measured at the very beginning of the true stress (σ_{yy}) versus logarithmic strain ε_{yy} curves at testing temperature $T = 333$ K. This zone has less phase transformation influence. Figure 3.4b shows the $\sigma_{yy} - \varepsilon_{yy}$ curves (right ordinate axis) at 333 K for all orientations, along with slopes $d\sigma/d\varepsilon$ (left ordinate axis) as a function of strain. Figure 3.4a shows with more detail the behaviour of $d\sigma/d\varepsilon$ at the beginning of loading. The elastic modulus at each orientation, E(θ), was determined by linear regression of $d\sigma/d\varepsilon$ in the range $0\% < \varepsilon_{yy} < 0.5\%$.

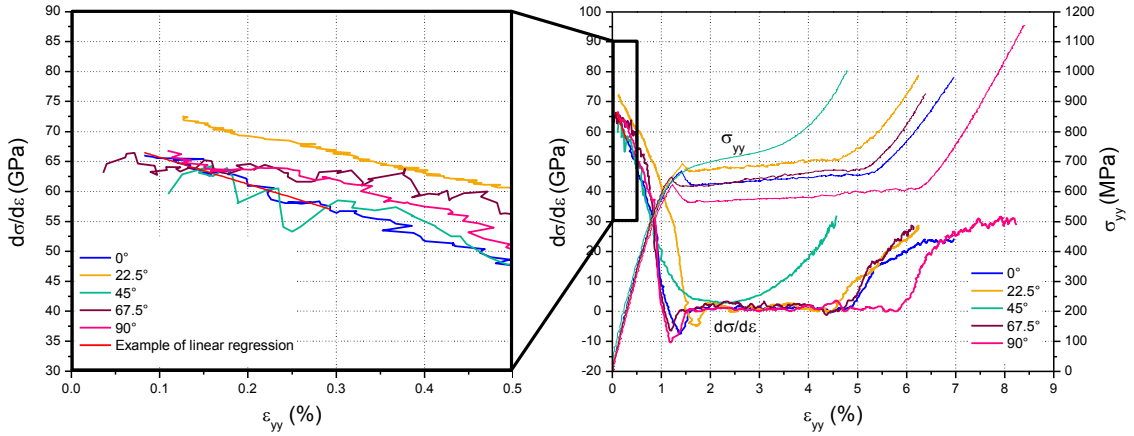

Figure 3.4: (a) Local slopes $d\sigma/d\varepsilon$ at the beginning of loading for all orientations at T = 333 K, showing the overall tendency when $\varepsilon_{yy} = 0$ and an example of linear regression and methodology for calculation of E(θ). (b) $\sigma_{yy} - \varepsilon_{yy}$ behavior (right axis) and local slopes $d\sigma/d\varepsilon$ (left axis) for the whole strain range.

Figure 3.5 shows the extracted E(θ) values. Little orientation dependence is observed. No anisotropy of the austenite elastic modulus E is measured from the results obtained in the present paper.

A mean value of E = 70 GPa is considered and used in this work. This value is a typical elastic modulus value for austenite phase (Alonso, 2015). Bechle and Kyriakides (2016) have also reported similar elastic modulus values for austenite phase after performing tensile tests in NiTi tubes: 66.8 GPa and 65.7 GPa for longitudinal and circumferential directions, respectively.

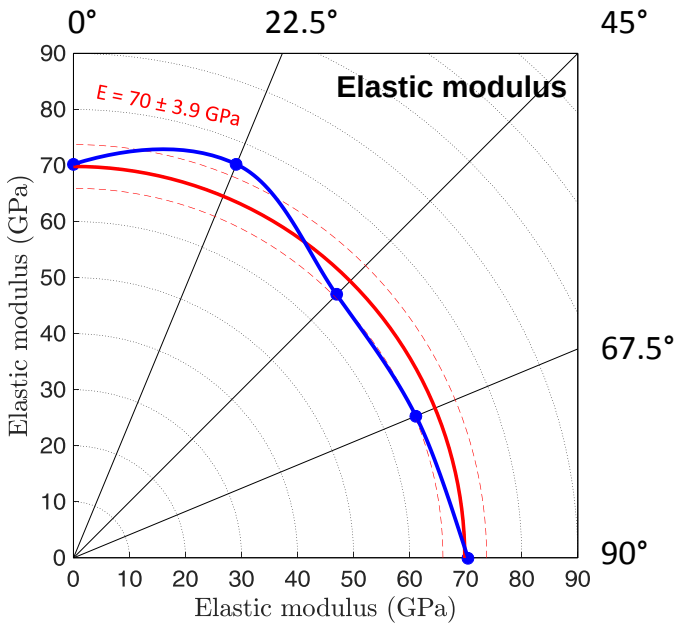

Figure 3.5: Elastic modulus extracted from tests at 333 K (blue), mean value of 70 GPa (red) and indication of standard deviation of ±3.9 GPa.

3.5.3 Inelastic stress-strain curves

Inelastic strain ε_{in} was obtained by subtracting the elastic strain $\varepsilon_{el} = \sigma_{yy}/\mathrm{E}$ from the global mechanical behaviour: $\varepsilon_{in} = \sigma_{yy} - \varepsilon_{yy}/\mathrm{E}$, with E = 70 GPa for all orientations. Figure 3.6 presents the tensile true stress σ_{yy}- logarithmic inelastic ε_{in} strain curves, plotted for each testing temperature, including loading until rupture for tests at 313 K, 323 K and 333 K. Except for plateau stress, the overall behaviour of all samples is similar for all temperatures. Some cycling effect was observed between the first and second loadings but mainly in the stress level and practically negligible on strain.

3.5.4 Anisotropy of the transformation strain ($\Delta\varepsilon_{tr}$)

Among the different methods to measure transformation strain, the plateau strain — which is simply the length of the stress plateau in a stress-strain curve — has been a very recurrent method used for superelastic alloys. It was once associated with the total transformation strain, in which the material is fully transformed into martensite. Now it is known that the plateau strain is in fact associated with the deformation of only the most favourably oriented martensite variants. In order to complete phase transformation the less favourably oriented variants still need to transform. This takes place as the stress resumes increasing right after the plateau (Liu, 2015). In other words, the transformation keeps going on even outside the stress plateau (Favier et al., 2007).

There are other evidences that martensitic transformation completion does not coincide with the end of stress plateau (Favier et al., 2007; Liu, 2015; Šittner et al., 2005). One work in particular (Pelton et al., 2015) shows that at the end of macroscopic stress plateau the martensite fraction has reached around 85%. These measurements were performed with neutron diffraction technique, which allows to compute the behaviour of the

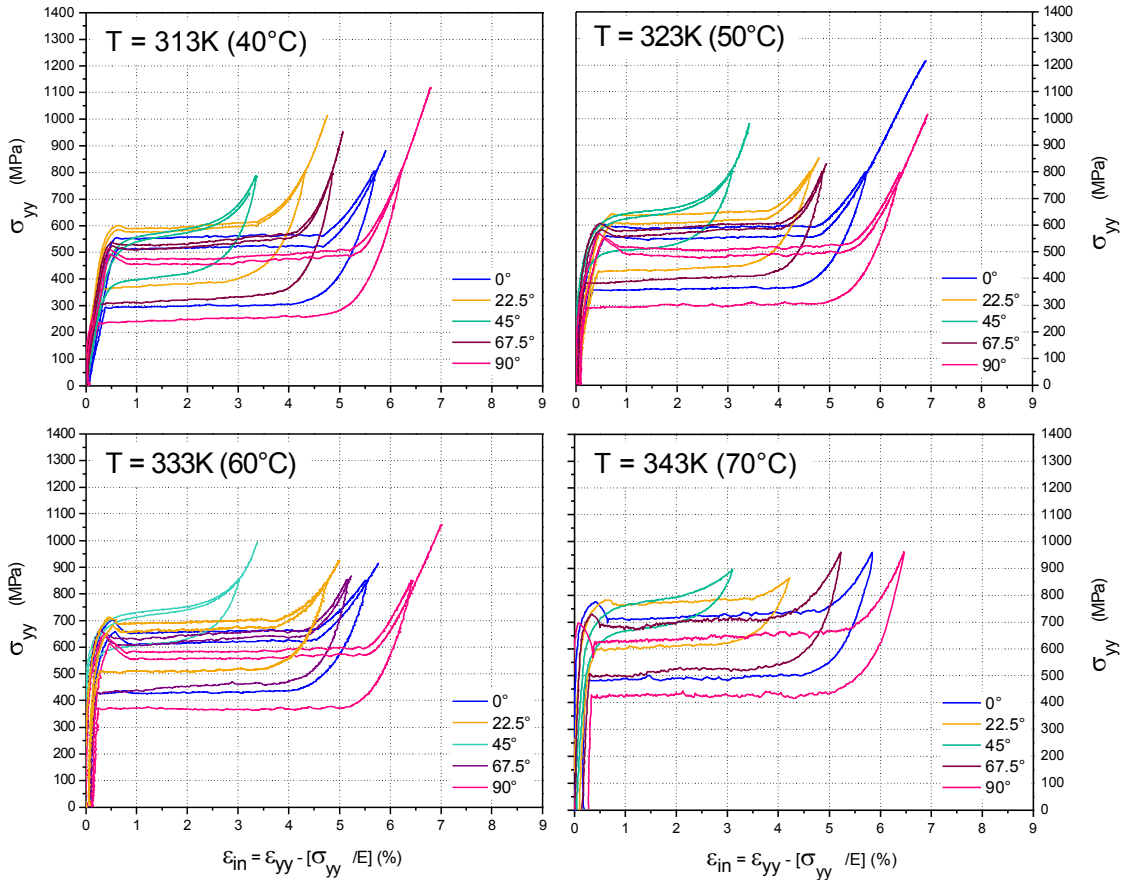

Figure 3.6: True tensile stress versus inelastic strain curves as function of testing temperature.

bulk material.

Therefore, instead of the plateau strain, total transformation strains are estimated in this work. Transformation strains ($\Delta\varepsilon_{tr}$) were determined from the σ_{yy}- logarithmic ε_{in} strain loading curves until rupture, plotted in Fig. 3.6. The procedure to estimate $\Delta\varepsilon_{tr}$ is based on the following:

- It was considered that there is a region of the loading curve after the stress plateau for which no plastic strain was experienced by the samples. Two facts give support to this assumption. On one hand, no residual strain was observed after the first cycle unloading; it means that there is no plastic deformation for strains lower than the maximum strain reached in the first cycle. On the other hand, seen the trend of loading curves until rupture in 3.6, it is likely that negligible plastic strain was experimented by the samples. The fact that the $d\sigma/d\varepsilon$ ratio is still increasing at the end of loading for all orientations (see Fig. 3.4b) is also an indication of the absence of plastic deformation. This is consistent with the amount of cold-work to which the tube was submitted during manufacturing process. Moreover, the $\sigma_{yy} - \varepsilon_{in}$ curves do not show any change of curvature between the end of stress plateau and the rupture point (except for the sample $\theta = 0°$ tested at 323 K).

- Elastic moduli of austenite and martensite are equal when true stress is used

(Alonso, 2015; Wagner and Windl, 2008). With this, when the material completes transformation (martensite fraction $f_m = 1$) in the absence of plasticity, the $\sigma_{yy} - \varepsilon_{in}$ curves would tend to a vertical line.

- Because of that, the function in Equation 3.10 was used to fit the final portion of the $\sigma_{yy} - \varepsilon_{in}$ curve between a point P and the rupture point, as schematically illustrated in Fig. 3.7. The tanh function was chosen because it reaches smoothly a constant value. σ_P, ε_P and a are the true stress, inelastic strain and local slope at point P, respectively.

$$\varepsilon_{in} - \varepsilon_P = (\Delta\varepsilon_{tr} - \varepsilon_P) \tanh\left(a \frac{\sigma_{yy} - \sigma_P}{\Delta\varepsilon_{tr} - \varepsilon_P}\right) \tag{3.10}$$

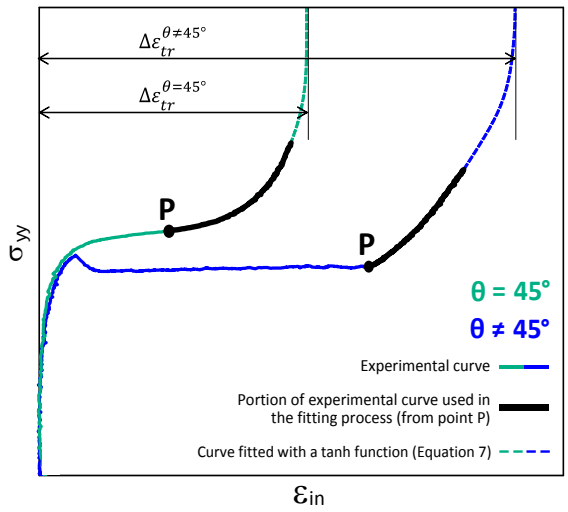

Figure 3.7: Methodology used for the estimation of transformation strain from curves of loading until rupture, which can be applied with or without the presence of a stress plateau.

Figure 3.8 shows the result of fitting for all orientations and testing temperatures.

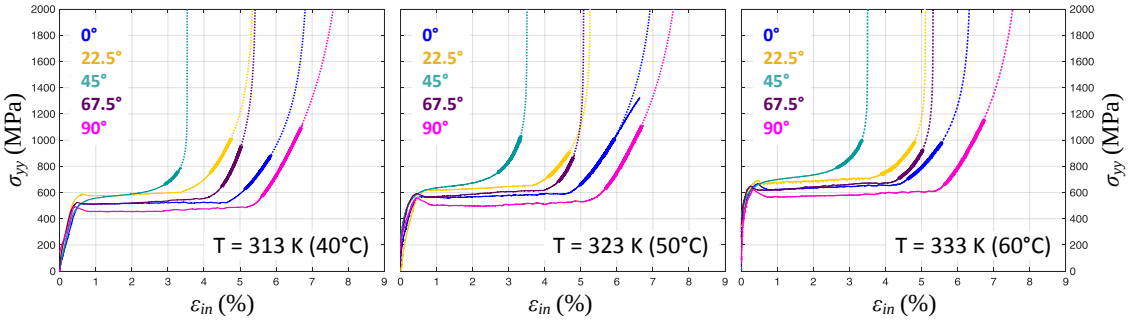

Figure 3.8: Results of fittings with Equation 3.10 for estimation of transformation strains ($\Delta\varepsilon_{tr}$). The thick zones are the final portions of the $\sigma_{yy} - \varepsilon_{in}$ curves that were used in the fitting process.

Figure 3.9 shows the dependence of $\Delta\varepsilon_{tr}$ on orientation, determined using the previous methodology.

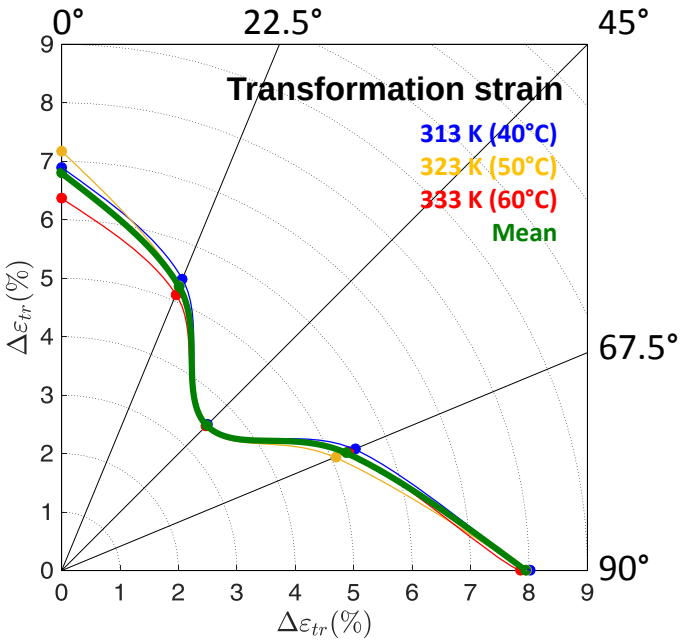

Figure 3.9: Transformation strain ($\Delta\varepsilon_{tr}$) values for all orientations and tested temperatures.

The following observations can be made regarding the orientation and temperature dependencies:

- $\Delta\varepsilon_{tr}$ is mostly independent of the testing temperature for all directions. The highest variation occurred at 0°, with small standard deviation of 4%.

- Because of that, mean values of $\Delta\varepsilon_{tr}$ are considered for each orientation and were plotted with a thicker line. A very strong anisotropy is observed. This anisotropy is almost symmetric with direction 45° as "mirror direction". The greatest difference reached 58%, between 45° and 90°.

A similar dependence was found experimentally by Robertson et al. (2006) for a flattened NiTi tube with 0.7 mm of wall thickness. However, the authors do not present their experimental curves and say only that the strain values correspond to the end of the stress plateaus. They also comment on how this shape of $\Delta\varepsilon_{tr} - \theta$ curve is consistent with paths of fatigue cracks in NiTi tubes, which preferentially follow the 45° direction, the direction that "requires the lowest strain energy to form martensite".

In his study about the anisotropy of a NiTi superelastic sheet, Liu (2015) observed that the recovery strain is independent of the sample orientation. The recovery strain is measured upon unloading after tensile loads up to 10% of global strain. Using theoretical transformation strains (calculated from texture measurements) they concluded that this orientation independence happens because the recovery strain is related with the transformation of both favourably and unfavourably oriented martensite variants. It is also worth noting that the degree of transformation of each sample was not the same at 10% strain, since some samples were deformed beyond the stress plateau and others not.

3.5.5 Anisotropy of forward and reverse transformation stresses

When a stress strain curve has a well defined stress plateau, the transformation stresses are generally defined as being the stress levels of the plateaus. In the absence of a plateau, the transformation stresses can be determined using the tangent intercept method along the stress strain curve. The stress-strain results presented in Fig. 3.3, however, show that the superelastic material of the tube can have these two behaviours, depending on the orientation. Then, for comparison purposes, the procedure for obtaining the transformation stresses had to be standardized.

The method used in this work was to measure the transformation stresses σ_{tr} at the same level of martensite fraction. Forward and reverse transformation stresses were then extracted at $\varepsilon_{in} = \Delta\varepsilon_{tr}(\theta)/2$, where $\Delta\varepsilon_{tr}(\theta)$ is the total transformation strain of each orientation. This is hypothetically equivalent to $f_m = 0.5$, assuming a linear relation between inelastic strain and martensite fraction f_m (Stebner et al., 2015).

Figure 3.10a presents the variation of σ_{tr} for forward and reverse transformations with θ for all testing temperatures. The overall trend of the curves is an increase of σ_{tr} from 0° to 45° followed by a decrease from 45° to 90°. However, less anisotropy is observed for the stresses for forward ($A \rightarrow M$) than for reverse ($M \rightarrow A$) transformation.

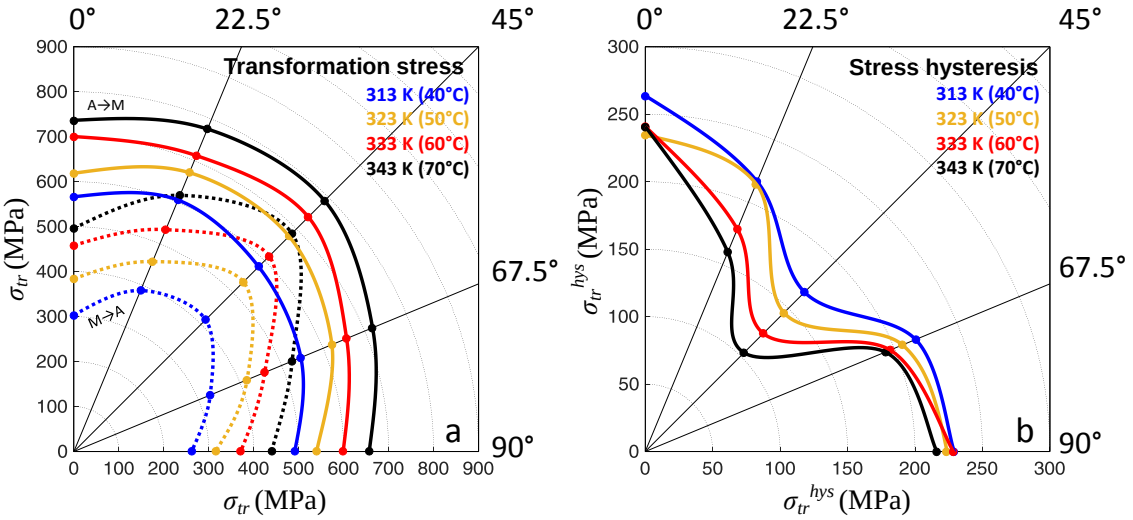

Figure 3.10: (a) Polar plot of transformation stresses at loading (forward transformation, $A \rightarrow M$) and unloading (reverse transformation, $M \rightarrow A$) defined at $f_m = 0.5$. (b) Stress hysteresis, calculated as the difference between transformation stress of loading and unloading ($\sigma_{tr}^{hys} = \sigma_{tr}^{A \rightarrow M} - \sigma_{tr}^{M \rightarrow A}$).

This difference between loading and unloading implies that exists an anisotropy in the stress hysteresis. The stress hysteresis, defined as $\sigma_{tr}^{hys} = \sigma_{tr}^{A \rightarrow M} - \sigma_{tr}^{M \rightarrow A}$ was calculated from the data in Fig. 3.10a and is shown in Fig. 3.10b. σ_{tr}^{hys} is smaller at 45° and higher at 0° and 90°.

In stress-induced phase transformation the hysteresis observed is caused mostly by dissipative processes which are associated mainly to the frictional work due to interfacial motion (Hamilton et al., 2004). Indeed, Barney et al. (2011) showed that tensile loading

at the 45° orientation leaves behind islands of untransformed material due to its predominant texture. Based on this, it is possible that the more restricted lattice movement in the 45° sample could hinder the interfacial motion. The restricted movement at 45° is caused by its probable predominant grain orientation, as discussed in Section 3.5.1. Therefore, less energy dissipation and smaller hysteresis were observed in this sample compared to other orientations.

3.5.6 Anisotropy of Clausius-Clapeyron coefficient

Clausius-Clapeyron coefficients (C) were calculated as being the slope of σ_{tr} versus T curves, thus at $f_m = 0.5$, for forward and reverse transformations.

Figure 3.11 shows the Clausius-Clapeyron coefficients for all orientations. A strong anisotropy is observed. Besides the anisotropy of both $C^{A\to M}$ and $C^{M\to A}$ coefficients, two other behaviours are observed:

- $C^{A\to M}$ is always smaller than $C^{M\to A}$;
- and the difference $C^{A\to M} - C^{M\to A}$ is very anisotropic.

These observations are discussed in more detail in Section 3.6 in a thermodynamic analysis.

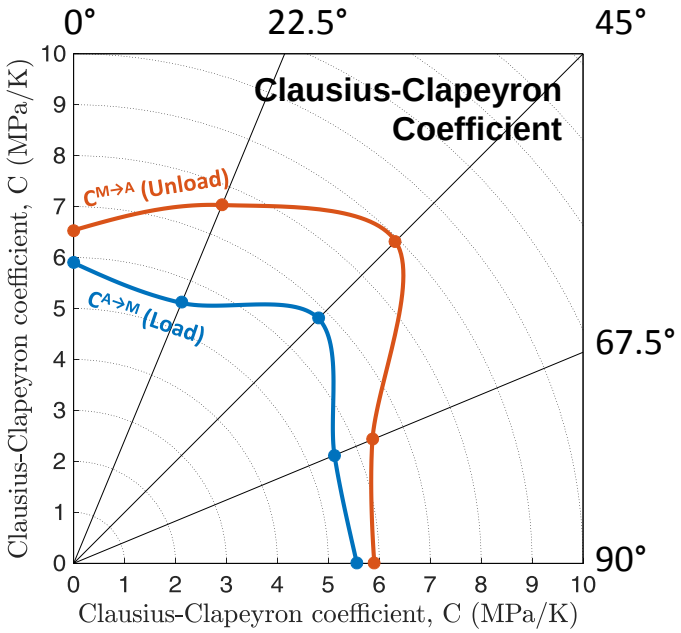

Figure 3.11: Clausius-Clapeyron coefficients for forward ($C^{A\to M}$) and reverse ($C^{M\to A}$) transformations at $f_m = 0.5$.

3.6 Thermodynamic analysis of the anisotropy

The experimental results are now analysed using the thermodynamic framework presented in Section 3.3.

3.6.1 Orientation dependence of the product $C\Delta\varepsilon_{tr}$

Equation 3.9 states the relation between external stress and temperature usually applied for a thermoelastic phase transformation. This form of the Clausius-Clapeyron equation is widely used for SMA. If this equation applies, the product $C\Delta\varepsilon_{tr}$ should not depend on orientation. This is because the entropy change ΔS_{ch} and mass density ρ depend only on the composition of the phases.

However, observing the curves in Fig. 3.12 one can see that the product $C\Delta\varepsilon_{tr}$ is in fact very orientation dependent. Considering the general form of the Clausius-Clapeyron relation written in Eq. 3.8, this result indicates that the storage and frictional energies might be temperature dependent.

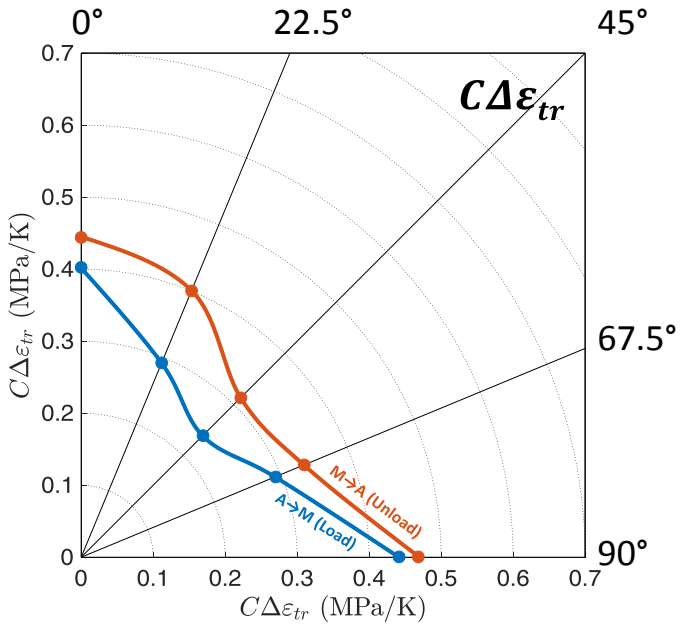

Figure 3.12: Product of Clausius-Clapeyron coefficients and transformation strain, showing an orientation dependent behaviour.

3.6.2 Temperature dependence of frictional work and stored elastic energy

In order to further investigate the temperature dependence of the frictional work and stored elastic energy terms, let us consider Eq. 3.7. Re-writing it for the forward and reverse transformations separately, respectively, gives:

$$\sigma_{tr}^{A\to M}(f_m,T)=\frac{\rho}{\Delta\varepsilon_{tr}}[\Delta H_{ch}-T\Delta S_{ch}+E_{st}^{'A\to M}(f_m,T)+E_{fr}^{'A\to M}(f_m,T)] \tag{3.11}$$

with $E_{st}^{'A\to M}(f_m,T)>0$ and $E_{fr}^{'A\to M}(f_m,T)>0$;

$$\sigma_{tr}^{M\to A}(f_m,T)=\frac{\rho}{\Delta\varepsilon_{tr}}[\Delta H_{ch}-T\Delta S_{ch}+E_{st}^{'M\to A}(f_m,T)+E_{fr}^{'M\to A}(f_m,T)] \tag{3.12}$$

with $E'^{M\to A}_{st}(f_m,T) > 0$ and $E'^{M\to A}_{fr}(f_m,T) < 0$.

Subtracting Eq. 3.12 from Eq. 3.11 one obtains the non-chemical energy variation within a transformation cycle:

$$\begin{aligned}(\sigma_{tr}^{A\to M} - \sigma_{tr}^{M\to A})_{(f_m,T)} &= \frac{\rho}{\Delta\varepsilon_{tr}}[(E'_{st} + E'_{fr})^{A\to M} - (E'_{st} - \mid E'_{fr} \mid)^{M\to A}]_{(f_m,T)} \\ &= \frac{\rho}{\Delta\varepsilon_{tr}}\Delta E'(f_m,T)\end{aligned} \tag{3.13}$$

where the notation $\mid E'_{fr} \mid$ is adopted to make explicit the sign of this term, avoiding any ambiguity.

Equation 3.13 states that $(\sigma_{tr}^{A\to M} - \sigma_{tr}^{M\to A})_{(f_m,T)}$ is directly proportional to $\Delta E'(f_m,T)$. This term accounts for the total variation of the irreversible energy between autenite-martensite transformation.

The dependence of $\Delta E'(f_m,T)$ with temperature is analysed for the specimens cut along 45° from the drawing direction. The mechanical behaviour in this orientation does not experience the localization phenomenon and thus the martensite fraction dependence can also be evaluated. Figure 3.13b illustrates the behaviour of $\Delta E'(f_m,T)$.

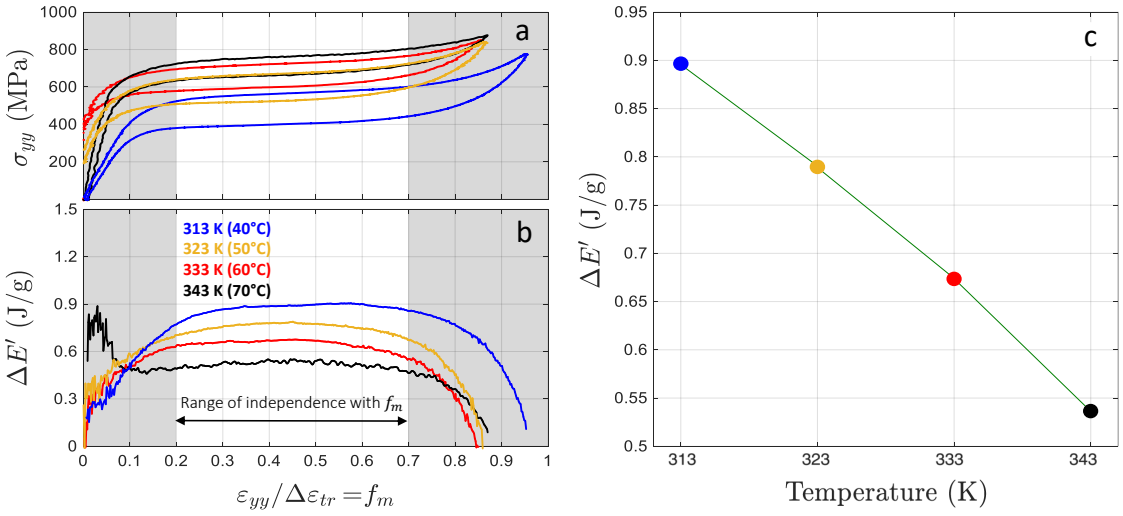

Figure 3.13: (a) True stress versus estimated martensite fraction at different temperatures for specimens cut along $\theta = 45°$. (b) Difference between loading and unloading stresses plotted in (a). (c) Temperature dependence of the term $\Delta E'$ extracted from (b) as the mean value in the range of independence with f_m.

To the most part $\Delta E'$ does not depend on f_m. It clearly depends on temperature, though. Figure 3.13c shows graphically $\Delta E'(T)$ as function of test temperature, calculated as mean values in the f_m range where it is constant. $\Delta E'$ decreases linearly with increasing temperature. This dependence on temperature is generally neglected, especially in the Clausius-Clapeyron equation.

3.6.3 Origin of the difference between forward and reverse Clausius-Clapeyron coefficients

The consequences of the aforementioned temperature dependence on the Clausius-Clapeyron relation are now analysed. The general form of Clausius-Clapeyron equation (Eq. 3.9) is written in Eq. 3.14 and Eq. 3.15 for the forward and reverse transformations, respectively. Since transformation strain does not depend on temperature, this term is neglected hereafter.

$$C^{A\to M} = \left(\frac{d\sigma}{dT}\right)^{A\to M} = \frac{\rho}{\Delta\varepsilon_{tr}}\left(-\Delta S_{ch} + \frac{\partial E'^{A\to M}_{st}}{\partial T} + \frac{\partial E'^{A\to M}_{fr}}{\partial T}\right) \tag{3.14}$$

$$C^{M\to A} = \left(\frac{d\sigma}{dT}\right)^{M\to A} = \frac{\rho}{\Delta\varepsilon_{tr}}\left(-\Delta S_{ch} + \frac{\partial E'^{M\to A}_{st}}{\partial T} - \frac{\partial \left|E'^{M\to A}_{fr}\right|}{\partial T}\right) \tag{3.15}$$

Subtracting the coefficient C for reverse transformation from the coefficient for forward transformation (Eq. 3.14 minus Eq. 3.15) one gets:

$$C^{A\to M} - C^{M\to A} = \frac{\rho}{\Delta\varepsilon_{tr}}\left[\frac{\partial(E'_{st} + E'_{fr})^{A\to M}}{\partial T} - \frac{\partial(E'_{st} - \mid E'_{fr} \mid)^{M\to A}}{\partial T}\right] \tag{3.16}$$

According to Eq. 3.13, the term inside the square brackets in Eq. 3.16 is equal to:

$$\left[\frac{\partial(E'_{st} + E'_{fr})^{A\to M}}{\partial T} - \frac{\partial(E'_{st} - \mid E'_{fr} \mid)^{M\to A}}{\partial T}\right] = \frac{\partial \Delta E'}{\partial T} \tag{3.17}$$

From Eq. 3.16 and Eq. 3.17, the difference between $C^{A\to M}$ and $C^{M\to A}$ is caused by the fact that $\partial\Delta E'/\partial T \neq 0$.

As shown in Fig. 3.11, $C^{A\to M} < C^{M\to A}$ for all orientations. This difference is commonly observed in NiTi alloys and some authors have attempted to explain it. Liu and Yang (2007), concluded that $C^{A\to M} < C^{M\to A}$ because the transformation strain is bigger for loading ($A \to M$) than for unloading ($M \to A$). Thus, as Clausius-Clapeyron coefficient is inversely proportional to transformation strain (see Eq. 3.14 and 3.15), $C^{A\to M} < C^{M\to A}$. However, they consider the transformation strains to be the lengths of forward and reverse stress plateaus. This premise is somewhat amiss, since it has been found evidence that martensitic transformation completion does not coincide with the end of the plateau (Favier et al., 2007; Šittner et al., 2005). In our opinion, the transformation strain is equal for forward and reverse transformations and then the explanation suggested by Liu and Yang (2007) would not be valid. The presented experimental results and the performed thermodynamic analysis show that $\partial\Delta E'/\partial T \neq 0$ is a more thermodynamically reasonable explanation for $C^{A\to M} \neq C^{M\to A}$.

Furthermore, as stated in Eq. 3.16 and Eq. 3.17, the nature of the relation between $\Delta E'$ and temperature determines the relation between $C^{A\to M}$ and $C^{M\to A}$: since $\partial\Delta E'/\partial T < 0$ (see Fig. 3.13c), $C^{A\to M} < C^{M\to A}$.

By definition, $\Delta E'$ is a term computing both of stored elastic energy and friction work contributions. However, while the friction work accumulates during forward and

reverse phase transformation, the stored elastic energy is accumulated during $A \rightarrow M$ to be mostly spent during the $M \rightarrow A$ transformation. According to the thermodynamic framework presented in Section 3.3, this is true once the macroscopic shape is totally recovered. This suggests that, at the end of a superelastic cycle, the dissipative energy is likely to have a stronger influence on the difference between $C^{A \rightarrow M}$ and $C^{M \rightarrow A}$.

3.7 Conclusion

The anisotropy of the temperature dependence of superelastic SMA was studied through the experimental characterization and thermomechanical analysis conducted in a thin walled NiTi tube. From the experimental data, the following conclusions are drawn:

1. Full transformation strain depends strongly on orientation but not on temperature. The lowest transformation strains were measured at 45° from the drawing direction. An almost symmetric profile was observed from this orientation to the drawing (0°) and transversal directions (90°). Variations of transformation strain reached 58% between orientations.

2. Transformation stress is also anisotropic. However, stress for reverse transformation is more orientation dependent than for forward transformation.

3. Clausius-Clapeyron coefficients of forward and reverse transformations are significantly anisotropic. Besides, the coefficient for reverse transformation is higher than for forward transformation for all orientations.

Supported by our experimental data, the following conclusions are achieved concerning the thermodynamic analysis:

1. The temperature dependence of the stored and dissipated energies is not negligible as typically assumed in the Clausius-Clapeyron equation. This conclusion is drawn based on the fact that the product of Clausius-Clapeyron coefficients and total transformation strain strongly depends on orientation.

2. Irreversibilities of the phase transformation are due to specific stored elastic energy (E'_{st}) and specific frictional energy (E'_{fr}). The difference $\Delta E'$ between ($E'_{st} + E'_{fr}$) during loading (forward $A \rightarrow M$ transformation) and unloading (reverse $M \rightarrow A$ transformation) of a superelastic test decreases with increasing test temperature.

3. The dependence of $\Delta E'$ on temperature is the cause for the Clausius-Clapeyron coefficient of forward transformation ($C^{A \rightarrow M}$) to be smaller than the Clausius-Clapeyron coefficient of reverse transformation ($C^{M \rightarrow A}$).

CHAPTER

FOUR

EFFECT OF ANISOTROPY ON THE STRAIN LOCALIZATION PHENOMENON DURING TENSILE TESTS

This chapter examines the strain distribution during tensile tests at different orientations in a NiTi tube. It particularly analyses the anisotropy influence on the strain localization phenomenon. Transformation fronts are identified using strain rate maps calculated from Digital Image Correlation (DIC) results. The phenomenon is examined throughout loading and unloading, during which the angle between the band and the tensile direction is measured. A plasticity approach is used to predict the band angle at different tensile orientations.

Contents

4.1 Introduction

Despite the undeniable potential of SMA, some of its typical phenomena hinders the development and improvement of engineering applications. Such phenomena are, for example: thermomechanical coupling, tension-compression asymmetry and heterogeneous deformation, all complex to model and simulate. The last one, also referred to as strain localization, is a heterogeneity from the micro to the macro scale. It appears as incompatibilities of crystallographic habit planes between austenite and martensite phases (Sedmak et al., 2016a), as well as is observable in tensile samples.

In practice, the localization phenomenon in SMA causes some inconveniences as: difficulties to perform an accurate characterization of the material mechanical behaviour (Hallai and Kyriakides, 2013); structural instabilities such is the case of tube bending, in which besides the tension-compression asymmetry, the tensioned side experiments strain localization (Bechle and Kyriakides, 2014; Reedlunn et al., 2014); and the negative impact it has on cyclic behaviour, reducing fatigue performance (Zheng et al., 2016) by cumulation of surface damage (Sedmak et al., 2016a).

In SMA, the localization phenomenon takes place in NiTi alloys when tension is the dominant mode of mechanical loading (Šittner et al., 2005). It is characterized by the appearance of a velocity discontinuity which constitutes a boundary between domains of transformed and untransformed material. The form of these boundaries depends on the sample geometry. In strip samples it is recognizable as inclined straight bands (Shaw and Kyriakides, 1997). The amount and distribution of these domains depend on some factors, like: nominal strain rate applied during loading, grain orientation (texture) and the direction of applied load.

In polycrystalline NiTi alloys it is generally accepted that most aspects of strain localization are explained by the relation between stress mode and texture. According to some literature reports, certain textures favour the development of localization bands while others hinder the phenomenon (Barney et al., 2011; Reedlunn et al., 2014). It has been demonstrated in NiTi tubes, for example, that the deformation is homogeneous under compression because the grains with higher critical transformation stress are more scattered compared to tension (Mao et al., 2010). In other words, tube texture seems to promote a uniform distribution of grains that transform easily under compression, while the grains that transform easily under tension are more concentrated.

Therefore, given that the strain localization is closely related with crystallographic texture, it is correct to state that this phenomenon is closely related to the anisotropic state of the material. With this in view, the objective of this chapter is to analyse the strain localization occurring in tensile samples cut at different orientations from the drawing direction of the NiTi tube. The phenomenon is studied using digital image correlation (DIC) strain maps.

Furthermore, Hill (1948, 1952) theory for localized necking, developed for plastic yielding, is used to analyse the angle between the transformation band and the tensile direction. Hill model has been used to predict angles of transformation bands in NiTi under tension with good agreement with experimental results (Bechle and Kyriakides, 2016; Shaw and Kyriakides, 1998). However, the analysis has been restricted to the the first band. In this chapter the evolution of the band angle throughout loading and unloading is studied.

4.2 Theoretical Approach

The influence of anisotropy on the localization phenomenon of the NiTi tube is addressed with Hill approach to localized necking based on plasticity theory, presented in Sections 1.6.2.3 and 1.6.3.3.

The description of Hill theory is focused on the case of uniaxial loading of orthotropic materials, i.e. materials that possess three mutually orthogonal planes of symmetry. Because the theory of plasticity was greatly developed in the light of sheet metal forming, the three orthogonal directions are generally denominated rolling, transverse and normal directions, as illustrated in Fig. 4.1. For the opened NiTi tubes used in this work, the rolling direction is called drawing direction.

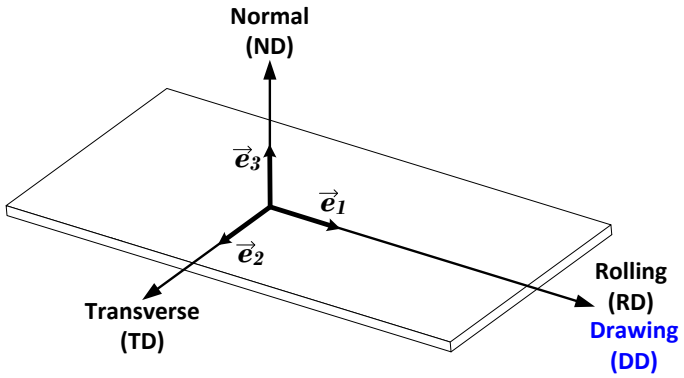

Figure 4.1: Orthogonal directions in a sheet. DD indicates the drawing direction of a flattened tube, which in the present work is equivalent to the rolling direction (RD) of a sheet.

Hill approach to localized necking requires the use of an anisotropic yield function. Here, Hill (1948) quadratic anisotropic criterion is used. This section starts with the presentation of Hill 1948 criterion, along with a correspondent anisotropic flow rule. The identification procedure of Hill 1948 parameters is described. Finally, the section presents Hill equations to predict the angle of a localized neck in a flat specimen under tensile load.

4.2.1 Hill (1948) anisotropic yield criterion

Hill was the first to propose an anisotropic yield criterion. He modified the Von Mises quadratic yield criterion by introducing six coefficients to express the orientation dependence. His new criterion is valid under three main conditions: (i) the material must have an orthotropic anisotropy; (ii) it must present no Bauschinger effect, where the yield stresses for tension and compression have the same algebraic value; and (iii) the yield stresses must not be influenced by hydrostatic pressure. Under these conditions, and having a Cartesian axes of reference coincident with the directions of symmetry (see Fig. 4.1), Hill yield criterion is

$$f(\sigma_{ij}) = F(\sigma_{22}-\sigma_{33})^2+G(\sigma_{33}-\sigma_{11})^2+H(\sigma_{11}-\sigma_{22})^2+2L\tau_{23}^2+2M\tau_{31}^2+2N\tau_{12}^2 = \sigma_Y^2 \quad (4.1)$$

where f denotes the yield function, σ_{ij} are the components of the Cauchy stress tensor in the basis $\vec{e}_1$,$\vec{e}_2$,$\vec{e}_3$; and F, G, H, L, M, N are material parameters describing the anisotropic state of the material. Plastic yielding occurs when $f = \sigma_Y^2$, where σ_Y is a reference yield stress, for example, in the rolling direction. These anisotropic parameters are related with the yield stresses in the principal directions of anisotropy by

$$\left.\begin{aligned} G+H &= \left(\frac{\sigma_Y}{X}\right)^2, \;\; 2L = \left(\frac{\sigma_Y}{R}\right)^2, \\ F+H &= \left(\frac{\sigma_Y}{Y}\right)^2, \;\; 2M = \left(\frac{\sigma_Y}{S}\right)^2, \\ F+G &= \left(\frac{\sigma_Y}{Z}\right)^2, \;\; 2N = \left(\frac{\sigma_Y}{T}\right)^2. \end{aligned}\right\} \tag{4.2}$$

where X, Y and Z are tensile yield stresses in the principal directions and R, S and T are the associated shear yield stresses. These six yield stresses are needed for a complete description of the anisotropic state of the material.

In a plane stress frame ($\sigma_{33} = \tau_{23} = \tau_{31} = 0$) Hill yield criterion is written

$$(G+H)\sigma_{11}^2 - 2H\sigma_{11}\sigma_{22} + (F+H)\sigma_{22}^2 + 2N\tau_{12}^2 = \sigma_Y^2 \tag{4.3}$$

It is easy to verify that if $3F = 3G = 3H = L = M = N$ the material is isotropic. This condition reduces Eq. 4.1 and Eq. 4.3 to the Von Mises yield criterion.

4.2.2 Experimental identification of anisotropic parameters

In a plane stress state, four mechanical parameters are needed to identify F, G, H and N. Usually, the first relation used in the identification process is either

$$G + H = 1 \tag{4.4}$$

taking X as reference yield stress ($\sigma_Y = X$), or

$$F + H = 1 \tag{4.5}$$

taking Y as reference yield stress ($\sigma_Y = Y$).

The other three equations typically involve strain increment relations.

4.2.2.1 Strain increment equations and definition of r-coefficient

For metallic materials, stresses and plastic strain increments are generally related by an associative flow rule (Khan and Huang, 1995), in which the plastic potential and a yield function are considered identical. In this case, the plastic strain increment is given by the flow rule

$$d\varepsilon_{ij}^p = \frac{\partial f}{\partial \sigma_{ij}} d\lambda \tag{4.6}$$

where $d\varepsilon_{ij}^p$ are the components of the plastic strain increment tensor, f is the yield function, σ_{ij} are the components of the Cauchy stress tensor and $d\lambda$ is the increment of the positive scalar factor of proportionality λ.

In the case of an associative flow rule, the principal directions of strain increment coincide with the principal directions of stress. Thus, for a plane stress state, applying the yield criterion (4.3) in the flow rule (4.6) results in the following strain increment equations

$$\left.\begin{aligned} d\varepsilon_{11}^p &= d\lambda[G\sigma_{11} + H(\sigma_{11} - \sigma_{22})], \\ d\varepsilon_{22}^p &= d\lambda[F\sigma_{22} + H(\sigma_{22} - \sigma_{11})], \\ d\varepsilon_{33}^p &= d\lambda[-(G\sigma_{11} + F\sigma_{22})], \\ d\varepsilon_{12}^p &= d\lambda(N\sigma_{12}). \end{aligned}\right\} \tag{4.7}$$

The ratio of the strain increment in the width direction and the strain increment in the thickness direction of a tensile sample is called r-coefficient, given by:

$$r = \frac{d\varepsilon_{width}^p}{d\varepsilon_{thickness}^p} \tag{4.8}$$

If the r-coefficient is greater than unity, the width deformation of the tensile sample is dominant. If it is less than unity the thickness deformation is dominant.

In terms of the principal directions represented in Fig. 4.1, the r-coefficient can be defined as

$$r = \frac{d\varepsilon_{\perp}^p}{d\varepsilon_{33}^p} \tag{4.9}$$

where $d\varepsilon_{\perp}^p$ is the strain increment in the direction perpendicular to the tensile axis and $d\varepsilon_{33}^p$ is the strain increment in the normal direction of the sample.

In specimens with small thickness it is very difficult to experimentally measure the deformation in the normal direction. In this case it is assumed that the material is incompressible and thus $d\varepsilon_{11}^p + d\varepsilon_{22}^p + d\varepsilon_{33}^p = 0$ during deformation . Under this assumption the r-coefficients can be calculated with the expression

$$r = -\frac{d\varepsilon_{\perp}^p}{d\varepsilon_{11}^p + d\varepsilon_{22}^p} \tag{4.10}$$

4.2.2.2 Orientation dependence of yield stress and strain increment

For a tensile sample oriented in an angle θ from the rolling direction, a new (x,y) coordinate system can be defined in the plane of the sample, as seen in Fig. 4.2.

The stress components in the $(\vec{e}_1,\vec{e}_2)$ and (x,y) coordinate systems are, respectively

$$\boldsymbol{\sigma} = \begin{bmatrix} \sigma_{11} & \sigma_{12} & 0 \\ \sigma_{21} & \sigma_{22} & 0 \\ 0 & 0 & 0 \end{bmatrix}_{\vec{e}_1,\vec{e}_2,\vec{e}_3} = \begin{bmatrix} 0 & 0 & 0 \\ 0 & \sigma & 0 \\ 0 & 0 & 0 \end{bmatrix}_{\vec{x},\vec{y},\vec{z}} \tag{4.11}$$

with:

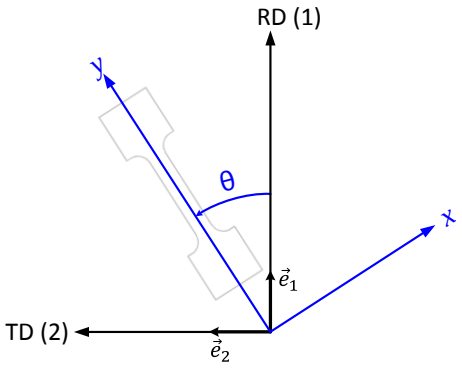

Figure 4.2: Tensile sample oriented in an arbitrary direction in the plane of the sheet metal. A new coordinate system is defined by an x-axis in its width direction and a y-axis in its longitudinal direction.

$$\left.\begin{aligned}\sigma_{11} &= \sigma\cos^2\theta,\\ \sigma_{22} &= \sigma\sin^2\theta,\\ \sigma_{12} &= \sigma\sin\theta\cos\theta.\end{aligned}\right\} \tag{4.12}$$

Substituting these relations in Eq. 4.3 gives the tensile yield stress as function of orientation angle θ:

$$\sigma_Y(\theta) = \sigma_Y[F\sin^2\theta + G\cos^2\theta + H + (2N - F - G - 4H)\sin^2\theta\cos^2\theta]^{-\frac{1}{2}} \tag{4.13}$$

The strain increments in the $(\vec{e}_1,\vec{e}_2)$ and (x,y) coordinate systems are, respectively

$$d\boldsymbol{\varepsilon^p} = \begin{bmatrix} d\varepsilon^p_{11} & d\varepsilon^p_{12} & 0\\ d\varepsilon^p_{21} & d\varepsilon^p_{22} & 0\\ 0 & 0 & d\varepsilon^p_{33}\end{bmatrix}_{\vec{e}_1,\vec{e}_2,\vec{e}_3} = \begin{bmatrix} d\varepsilon^p_{xx} & d\varepsilon^p_{xy} & 0\\ d\varepsilon^p_{yx} & d\varepsilon^p_{yy} & 0\\ 0 & 0 & d\varepsilon^p_{zz}\end{bmatrix}_{\vec{x},\vec{y},\vec{z}} \tag{4.14}$$

The strain increments in the $(\vec{e}_1,\vec{e}_2)$ coordinate system are obtained substituting Equations 4.12 in the strain increment Equations 4.7:

$$\left.\begin{aligned} d\varepsilon^p_{11} &= [(G+H)\cos^2\theta - H\sin^2\theta]\sigma d\lambda,\\ d\varepsilon^p_{22} &= [(F+H)\sin^2\theta - H\cos^2\theta]\sigma d\lambda,\\ d\varepsilon^p_{33} &= -(F\sin^2\theta + G\cos^2\theta)\sigma d\lambda,\\ d\varepsilon^p_{12} &= (N\cos\theta\sin\theta)\sigma d\lambda.\end{aligned}\right\} \tag{4.15}$$

4.2.2.3 Orientation dependence of r-coefficients and relation with F, G, H and N

By definition, the r-coefficient in an tensile sample oriented at an angle θ from the rolling direction is (see Fig. 4.2)

$$r_\theta = \frac{d\varepsilon^p_{xx}}{d\varepsilon^p_{zz}} = \frac{d\varepsilon^p_{xx}}{d\varepsilon^p_{33}} \tag{4.16}$$

where the strain increment $d\varepsilon^p_{xx}$ is obtained from the rotation around the z-axis, which results in

$$r_\theta = \frac{d\varepsilon^p_{11}\sin^2\theta + d\varepsilon^p_{22}\cos^2\theta - d\varepsilon^p_{12}\sin\theta\cos\theta}{d\varepsilon^p_{33}} \tag{4.17}$$

Substituting Eq. 4.15 in Eq. 4.17 gives

$$r_\theta = \frac{H + (2N - F - G - 4H)\sin^2\theta\cos^2\theta}{F\sin^2\theta + G\cos^2\theta} \tag{4.18}$$

which establishes a direct relation between r-coefficients and Hill anisotropic parameters.

In view of sheet metal forming processes, the identification of F, G, H and N is generally performed with r-coefficients calculated from uniaxial tests along $\theta = 0°$, $45°$ and $90°$. They are denoted r_0, r_{45} and r_{90}. Substituting these θ values in Eq. 4.18 gives:

$$r_0 = \frac{H}{G}, \qquad r_{45} = \frac{N}{F+G} - \frac{1}{2} \qquad \text{and} \qquad r_{90} = \frac{H}{F}. \tag{4.19}$$

The relations in Eq. 4.19, together with Eq. 4.4 or Eq. 4.5, are used to estimate Hill anisotropic parameters.

4.2.2.4 Comments and evaluation of Hill 1948 anisotropic yield criterion

Since Hill presented his anisotropic yield criterion in 1948, the subject evolved greatly and today a large number of anisotropic yield functions are available. Nevertheless, this criterion remains one of the most used to describe the plastic behaviour of sheet metals (Chen et al., 2013). This is due to some considerable advantages, like its simplicity, the fact that it requires a small number of mechanical parameters and because its coefficients have a direct physical meaning.

The suitability of the yield criterion is verified by the accuracy of the prediction of the yield locus, and the in-plane variation of uniaxial yield stresses and r-coefficients (Banabic, 2010). In this work, the yield criterion is tested by its ability to predict the orientation dependence of transformation stress, with Eq. 4.13.

Furthermore, it is worth noting that the validity of the analysis performed in this chapter is restricted to the tensile behaviour of NiTi. This is because Hill quadratic criterion is unable to predict the tension-compression asymmetry of NiTi uniaxial behaviour due to the condition of no Bauschinger effect.

4.2.3 Localization phenomenon in a strip under tension

Hill plasticity theory for localized necking establishes a criterion for determining the direction in which a neck will appear. As discussed in Section 1.6.2.3, a localized neck should coincide with a characteristic, since characteristics are curves of zero rate of extension (Hill, 1952). If the stress is uniform in the tensioned sample, the characteristic is straight (Hill, 1950) and thus the neck appears as a straight line.

In Hill (1948), the author determined the characteristics in a state of plane stress. Figure 4.3 shows a strip cut at an angle θ from the rolling direction (RD) of the material and in which a neck developed at an angle α from the y-axis of the strip.

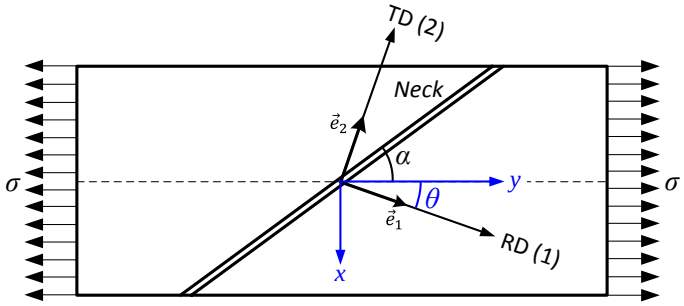

Figure 4.3: Tensile sample oriented at an angle θ from the rolling direction and a neck formed at an angle α from the y-axis of the sample.

In a plane stress state, the slopes dx_2/dx_1 of the characteristic (with dx_1 and dx_2 being the necks' local breadths along the rolling and transverse directions, respectively) satisfy the equation

$$d\varepsilon^p_{11}dx_1^2 + 2d\varepsilon^p_{12}dx_1dx_2 + d\varepsilon^p_{22}dx_2^2 = 0 \tag{4.20}$$

which, substituting with Eq. 4.12 and Eq. 4.15, gives

$$[(G+H)\sigma_{11} - H\sigma_{22}]dx_1^2 + 2N\sigma_{12}dx_1dx_2 + [(F+H)\sigma_{22} - H\sigma_{11}]dx_2^2 = 0 \tag{4.21}$$

With α being the angle of the neck measured away from the y-axis of the strip, the characteristic slopes are defined by

$$\frac{dx_2}{dx_1} = \tan(\theta + \alpha) \tag{4.22}$$

Inserting Eq. 4.22 and Eq. 4.12 in Eq. 4.21, a relation between θ and α is established as

$$a\tan^2(\alpha) + b\tan(\alpha) - c = 0 \tag{4.23}$$

where

$$\left.\begin{aligned} a &= H + \sin^2\theta\cos^2\theta[(N-F-2H) + (N-G-2H)], \\ b &= 2\sin\theta\cos\theta[(N-F-2H)\sin^2\theta - (N-G-2H)\cos^2\theta], \\ c &= a + F\sin^2\theta + G\cos^2\theta. \end{aligned}\right\} \tag{4.24}$$

4.3 Results

This section presents two sets of results. The first focus on the averaged strain measurements. An overline is used to differentiate the averaged strain notation from the local strain notation.

Figure 4.4a, 4.4b and 4.4c shows the nominal stress (Σ_{yy}), averaged transverse strain ($\bar{\varepsilon}_{xx}$) and averaged shear strain ($\bar{\varepsilon}_{xy}$) versus averaged longitudinal strain ($\bar{\varepsilon}_{yy}$), respectively. These curves are presented for three studied temperatures.

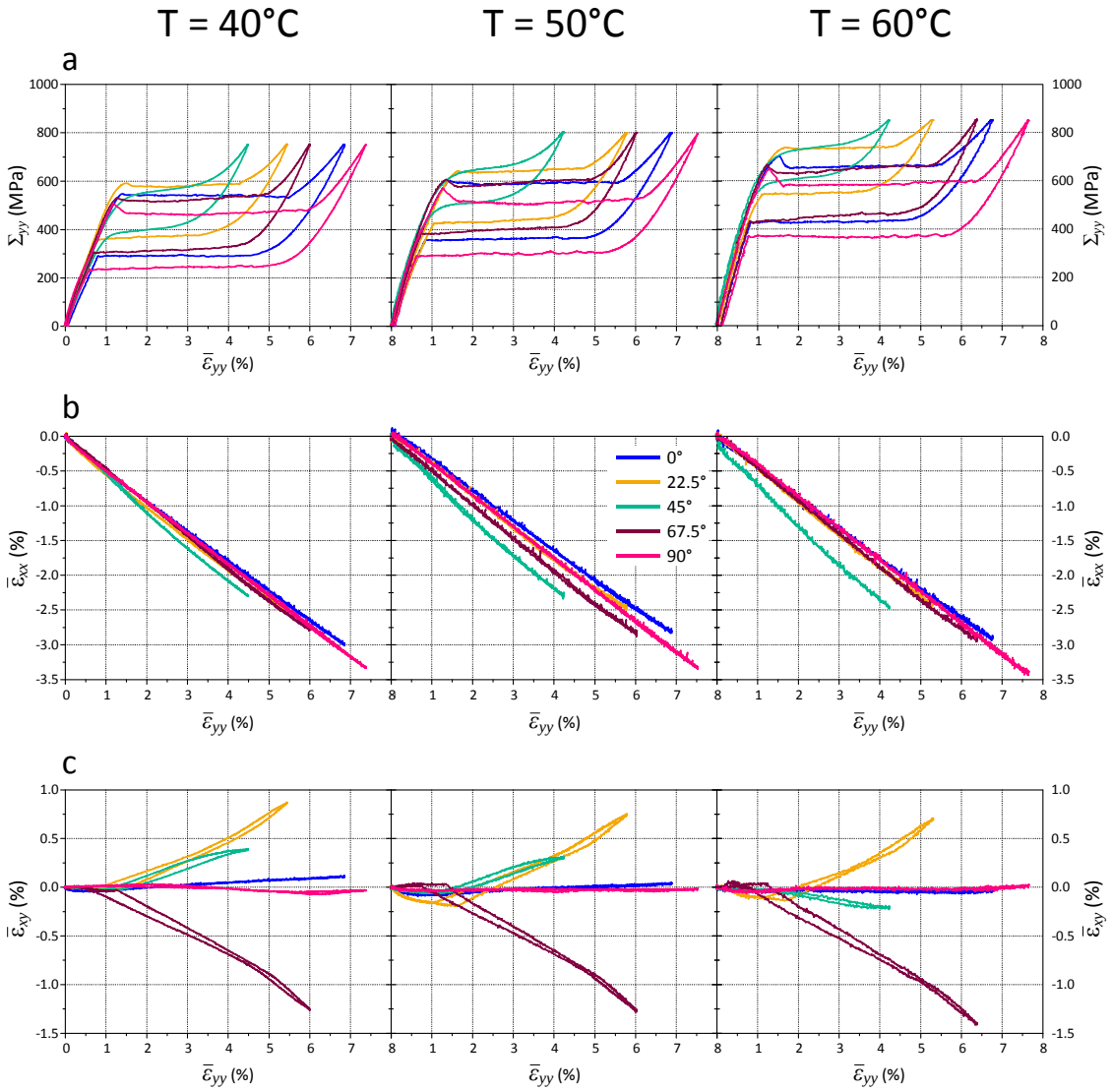

Figure 4.4: (a) Nominal tensile stress versus averaged longitudinal strain, (b) averaged transverse strain versus averaged longitudinal strain and (c) averaged shear strain versus averaged longitudinal strain for all studied directions and temperatures.

The second set of results focus on local strain measurements, where strain maps of the zone of interest (ZOI) throughout loading and unloading are analysed. The markers on the stress-strain curves in Fig. 4.5 correspond to the instants when the strain maps were extracted for each orientation. Only the strain maps for 60°C are shown in this section. This is because no significant differences, qualitative or quantitative, were observed among tests performed at the three temperatures. Strain maps for the other temperatures are presented in Appendix B. Figures 4.6, 4.7 and 4.8 show the strain maps for longitudinal (ε_{yy}), transverse (ε_{xx}) and shear (ε_{xy}) components, respectively.

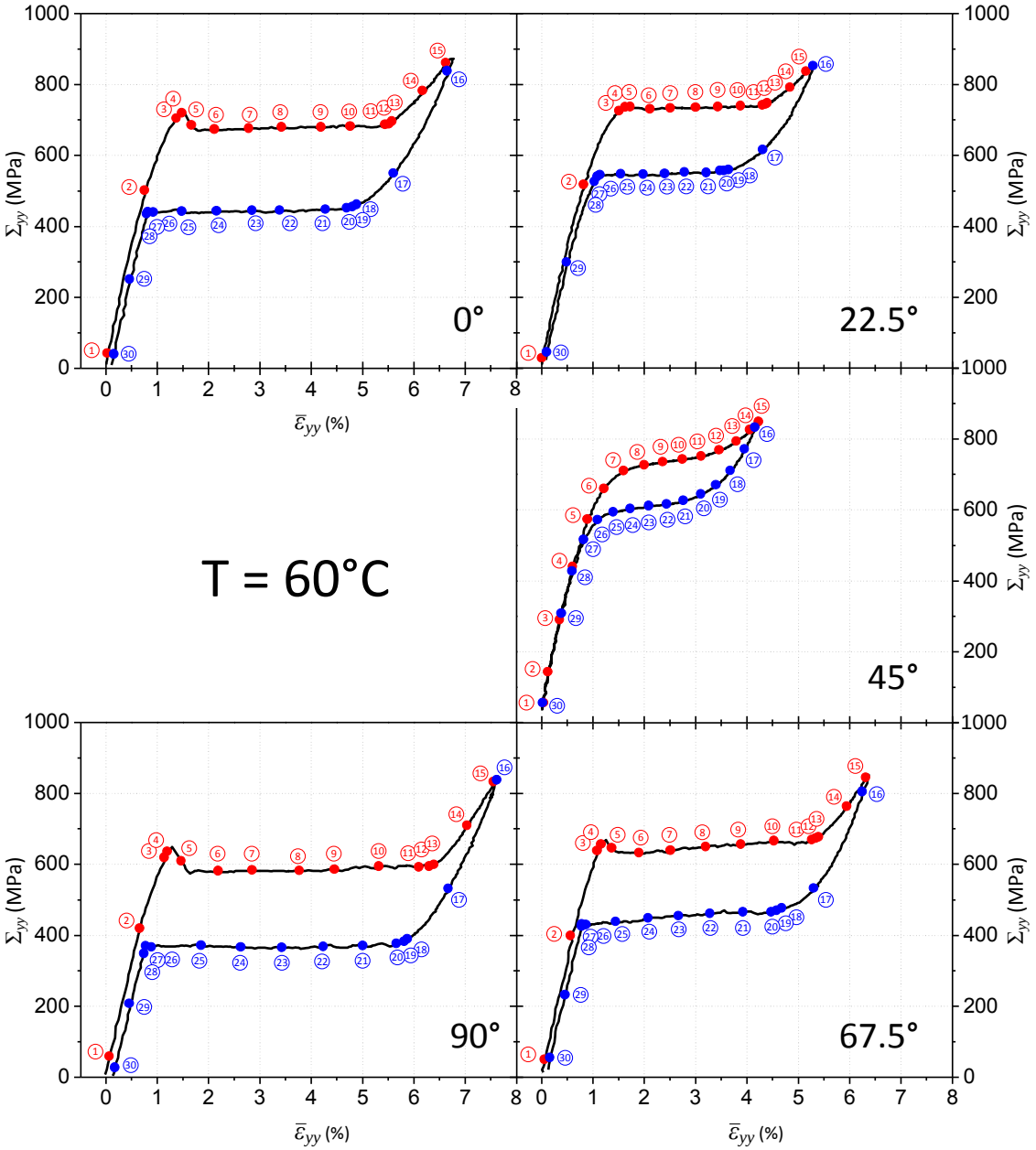

Figure 4.5: Nominal tensile stress versus averaged longitudinal strain at 60°C in the five studied directions. Red markers indicate where the strain maps were extracted during loading and blue markers during unloading.

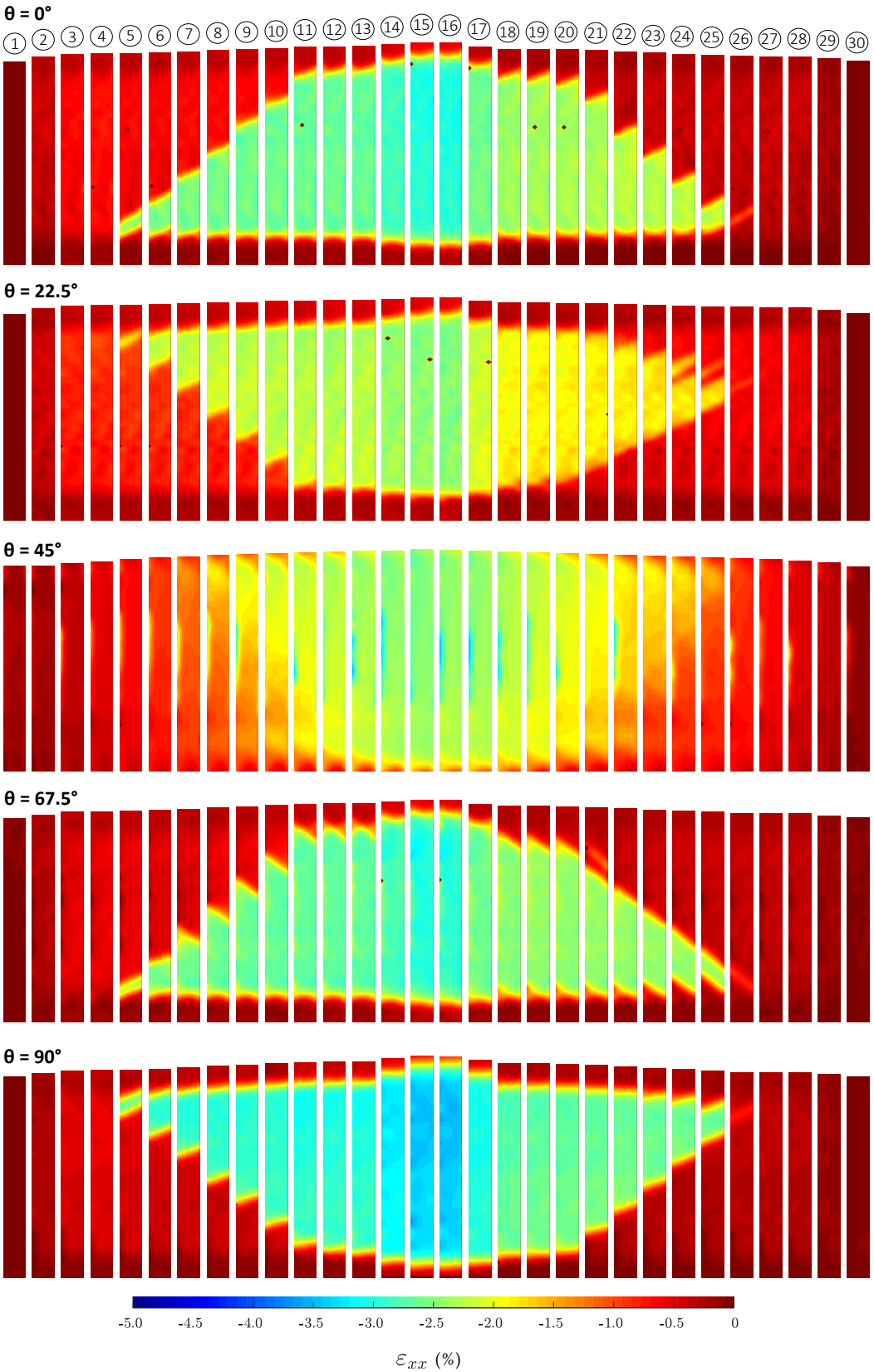

Figure 4.6: Transverse strain maps (ε_{xx}) of oriented samples under tensile load at 60°C.

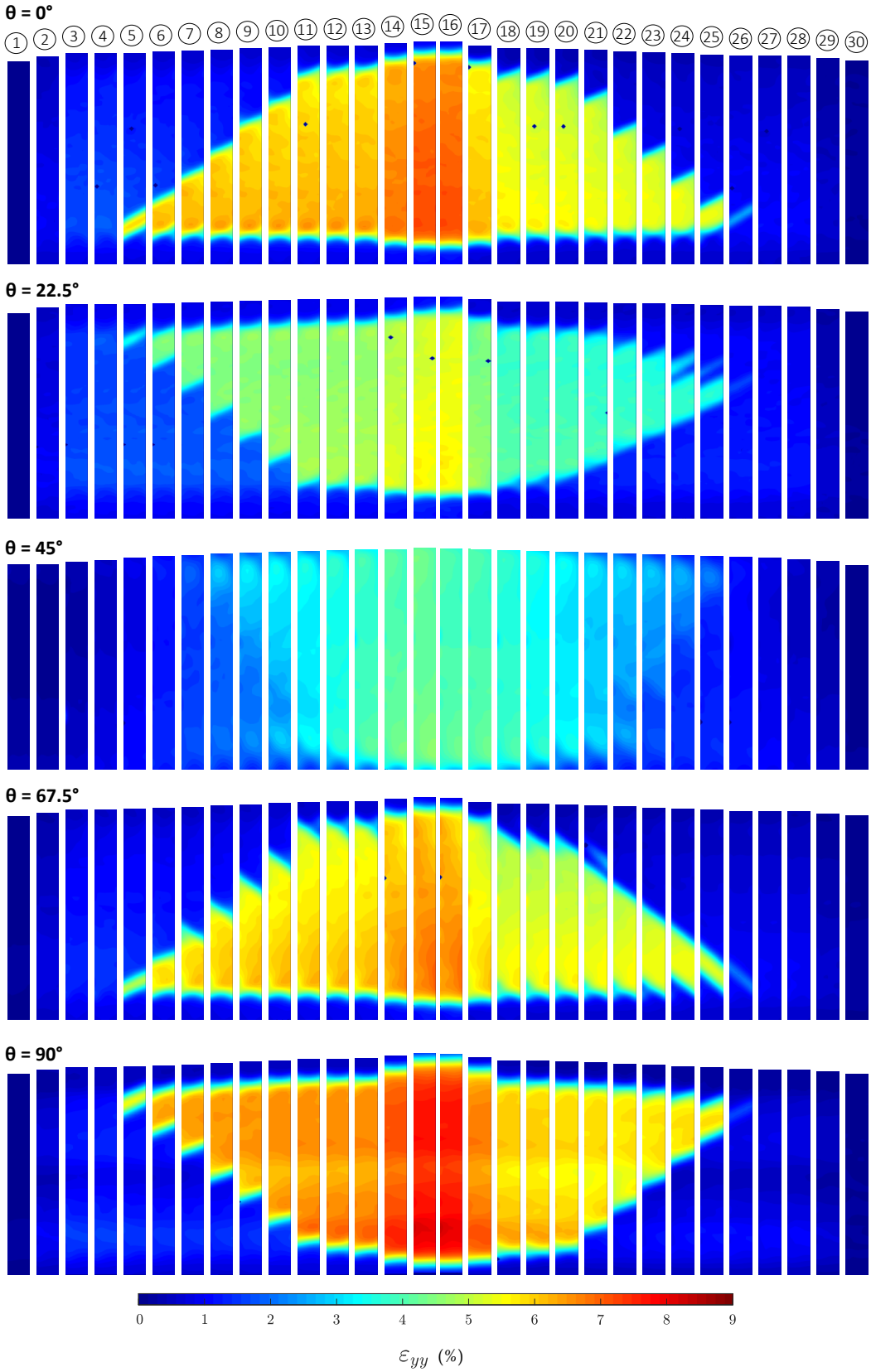

Figure 4.7: Longitudinal strain maps (ε_{yy}) of oriented samples under tensile load at 60°C.

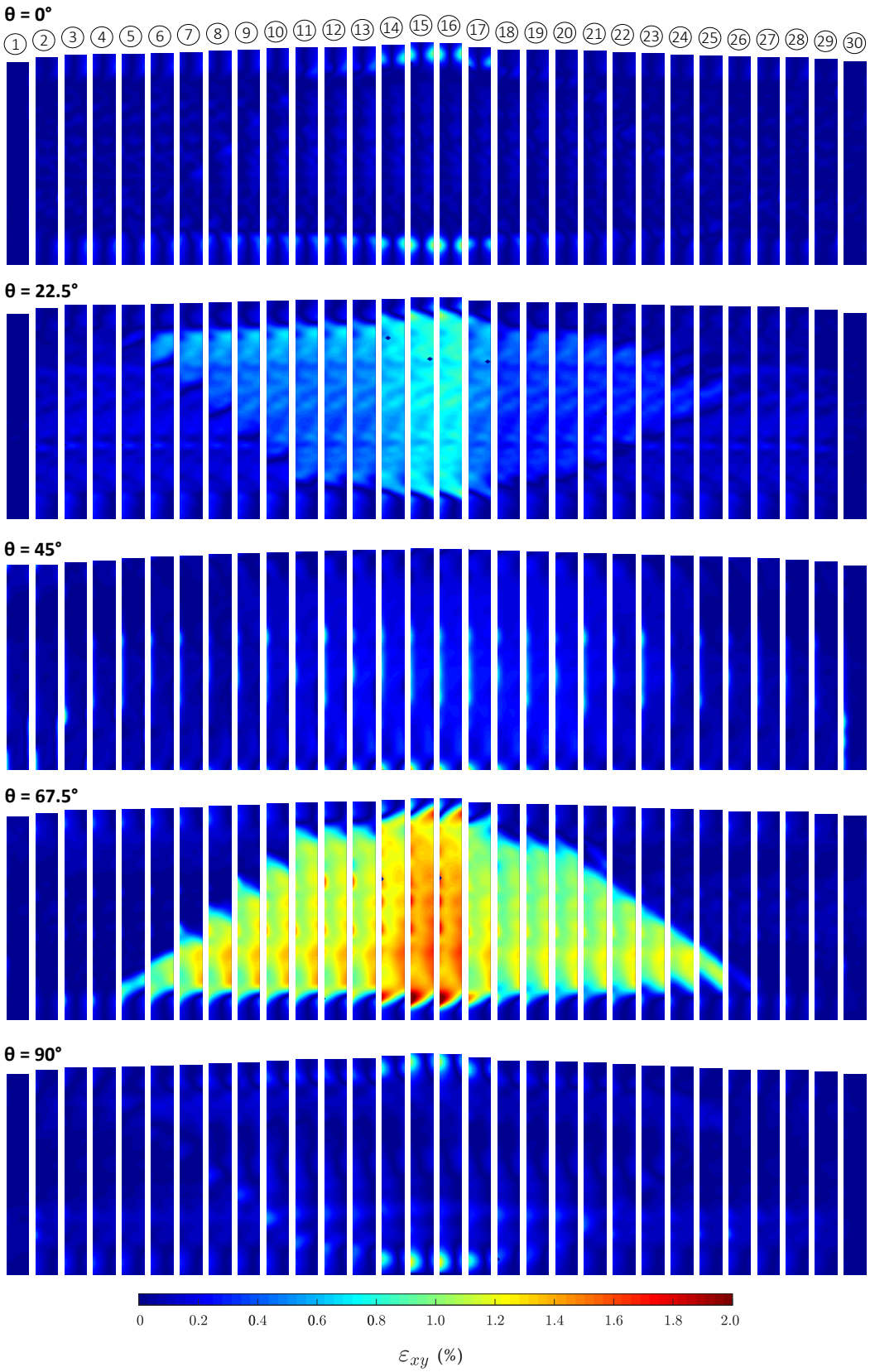

Figure 4.8: Shear strain maps (ε_{xy}) of oriented samples under tensile load at 60°C.

4.4 Discussion

4.4.1 Qualitative analysis of results

4.4.1.1 Averaged strain measurements

In the tests shown in Fig. 4.4, the maximum loading stress were taken equal to 750 MPa, 800 MPa and 850 MPa for T = 40°, 50° and 60°, respectively. This was done to take into account the Clausius-Clapeyron relation.

4.4.1.1.a Stress-strain curves

Observing the curves in Fig. 4.4a, the $\bar{\varepsilon}_{yy}$ strain values attained at the end of loading do not depend on temperature. This is also true for the other strain components, as can be seen in Figures 4.4b and 4.4c.

All studied orientations show a well defined stress plateau. The only exception is 45°, where the stress continually increases and the stress-strain curves are smooth throughout loading and unloading. The orientation dependence becomes very noticeable outside the apparent elastic zone, from $\bar{\varepsilon}_{yy} = 1\%$ in loading and below $\bar{\varepsilon}_{yy} = 0.75\%$ in unloading. The term apparent is used because in NiTi superelasticity there is evidence that the phase transformation starts as soon as loading begins (Favier et al., 2007; Gall et al., 2005; Liu and Xiang, 1998; Rajagopalan et al., 2005).

4.4.1.1.b Transverse strain and strain ratio

In Fig. 4.4b the local slopes of the curves represent the strain increment ratio (ν_{xy}), where

$$\nu_{xy} = -\frac{d\bar{\varepsilon}_{xx}}{d\bar{\varepsilon}_{yy}} \tag{4.25}$$

The evolution of ν_{xy} with strain is shown in Fig. 4.9 for tests at 60°C. Before the calculating the incremental ratios $-d\varepsilon_{xx}/d\varepsilon_{yy}$ the $\bar{\varepsilon}_{xx}$ versus $\bar{\varepsilon}_{yy}$ curves were fitted with a 9th degree polynomial to minimize the noise (see Fig 4.9a).

Figure 4.9b shows the variation of ν_{xy} with strain. The excessive variation at $\bar{\varepsilon}_{yy}$ up to 0.005 is disregarded. For the samples that present a stress plateau, ν_{xy} values are between 0.4 and 0.5. The ν_{xy} for samples at 22.5° and 67.5° seem to be slightly higher than for the samples 0° and 90°. The same type of orientation dependence was observed for loading and unloading during tests at 40°C and 50°C (see Appendix B).

The highest value of ν_{xy}, as well as the more significant variation, are achieved by the sample at 45°. This same ν_{xy} behaviour was verified in tests performed at other temperatures, as shown in Fig. 4.10. Under the assumption of incompressibility, this indicates that near $\theta = 45°$ the material of the tube under tension tends to deform more in the width direction compared to the thickness direction, while in the other orientations the opposite happens.

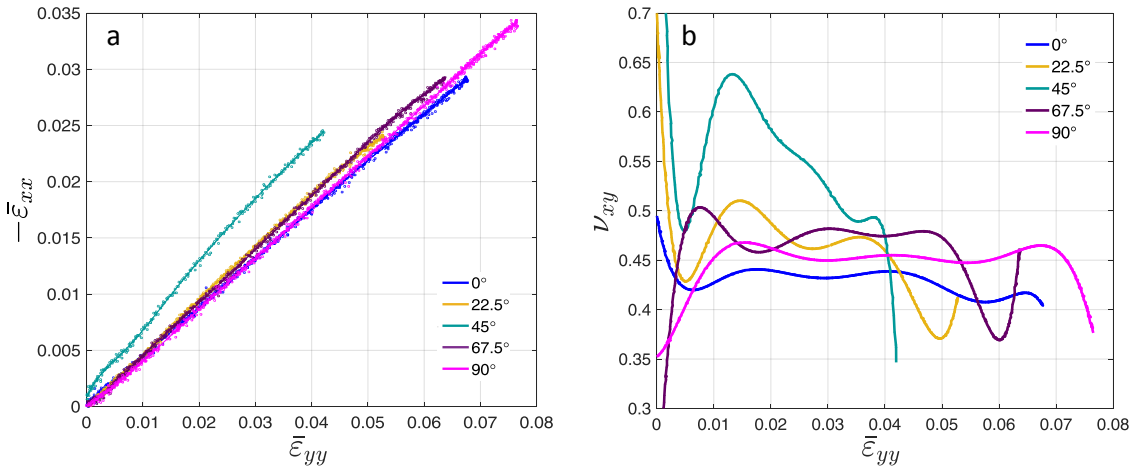

Figure 4.9: (a) Superposition of experimental $-\bar{\varepsilon}_{xx}$-$\bar{\varepsilon}_{yy}$ curves (dots) and polynomial fittings (lines). (b) Evolution of $\nu_{xy} = -d\varepsilon_{xx}/d\varepsilon_{yy}$ for tensile tests at 60°C.

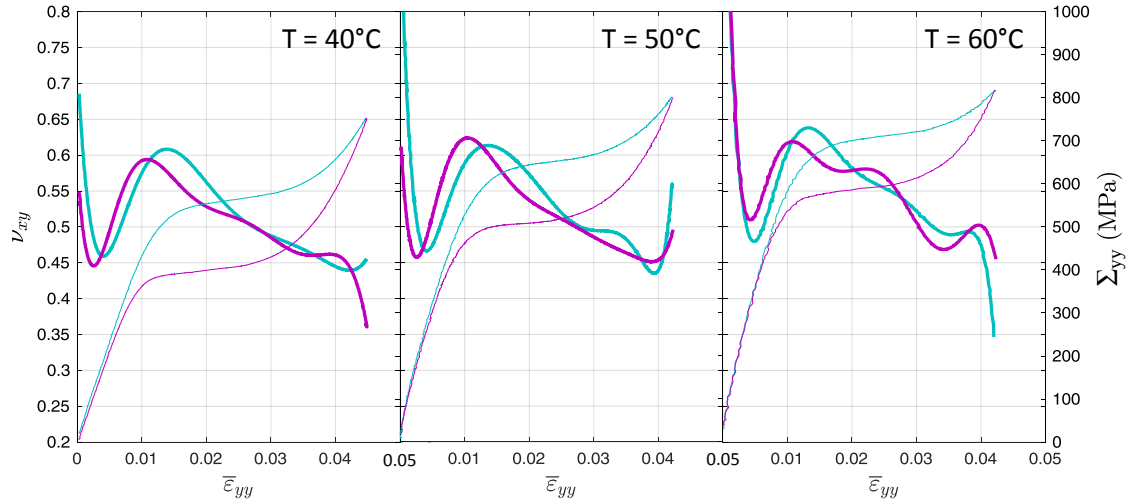

Figure 4.10: Evolution of ν_{xy} at $\theta = 45°$ for tensile tests at 40°C, 50°C and 60°C.

4.4.1.1.c Shear strain

The averaged shear strain $\bar{\varepsilon}_{xy}$ shown in Fig. 4.4c is negligible in the drawing and transverse directions (0° and 90°). In the other orientations the shear component is present but small prior to the stress plateau, after which it increases monotonically (in absolute value). This confirms that indeed the tube material has an orthotropic anisotropy with symmetry directions on the longitudinal and transverse directions, as expected after drawing operations. At a constant $\bar{\varepsilon}_{yy}$ value, the 67.5° orientation is the one experimenting the highest shear strain, followed by 22.5° and 45°.

4.4.1.2 Local strain measurement (strain maps)

Regarding the local strain behaviour, transverse (ε_{xx}, Fig. 4.6) and longitudinal (ε_{yy}, Fig. 4.7) strain maps show that all studied directions, except the 45°, experiment strain localization. For the orientations that localize, only one band is formed upon loading. This indicates that the nominal strain rate applied during tensile tests was sufficiently low to avoid self heating (Elibol and Wagner, 2015). All bands initiate at the extremities of samples, where there is stress concentration.

For some of the tests the band is unstable (see also results at 40°C and 50°C in Appendix B). The instabilities occur mostly at the band appearance, when it changes direction before stabilizing and continuing propagation. The observed instabilities are likely due to the sample geometry. Because the ratio between the sample length and width is not very high, significant in plane kinking may occur. The material tries to minimize the built in plane moment by changing the direction of the band (Jiang et al., 2017; Shaw and Kyriakides, 1997). Furthermore, it is observed in the strain maps that the band angle increases with strain, mainly in the 0° and 90° orientations. This also seems to be caused by sample geometric effects, because during unloading the band propagation is a lot more stable than during loading for almost all tests.

In the shear strain maps (ε_{xy}, Fig. 4.8) it can be seen that indeed the highest shear absolute values are attained by the transformed zone of sample at 67.5°, followed by the 22.5° and then by the 45°. In this last direction, however, the strain distribution is homogeneous in the same way as for the other strain components.

4.4.2 Strain rate

The localized necking that occurs in a tensile loading is idealized as a velocity discontinuity (Hill, 1948, 1952). In this manner, to evaluate the strain localization phenomenon strain rate ($\dot{\varepsilon}_{yy}$) maps were calculated from the ε_{yy} maps with the following equation

$$\dot{\varepsilon}_{yy}(M,t) = \frac{\varepsilon_{yy}(M,t) - \varepsilon_{yy}(M,t-\Delta t)}{\Delta t} \tag{4.26}$$

where M is a material point in the ZOI, t is the instant in which the map was taken and Δt is the time interval between two consecutive strain maps. Figure 4.11 shows these calculated strain rate maps for tests at 60°C (see the strain rate maps for the other temperatures in Appendix B) . They are presented in absolute value to enhance the contrast of the bands in the chosen scale. Nevertheless, during loading (from instants 1 to 15) the discontinuity has positive values and during unloading (from instants 16 to 30) it has negative values.

At 45° it is very clear that no strain localization occurs. When compared to the velocity discontinuities of the other orientations, the 45° is very homogeneous.

During the loading of the samples oriented at 0°, 22.5°, 67.5° and 90° a single band appears (instant 5). The instabilities observed mostly at the band appearance can be clearly seen in the strain rate maps.

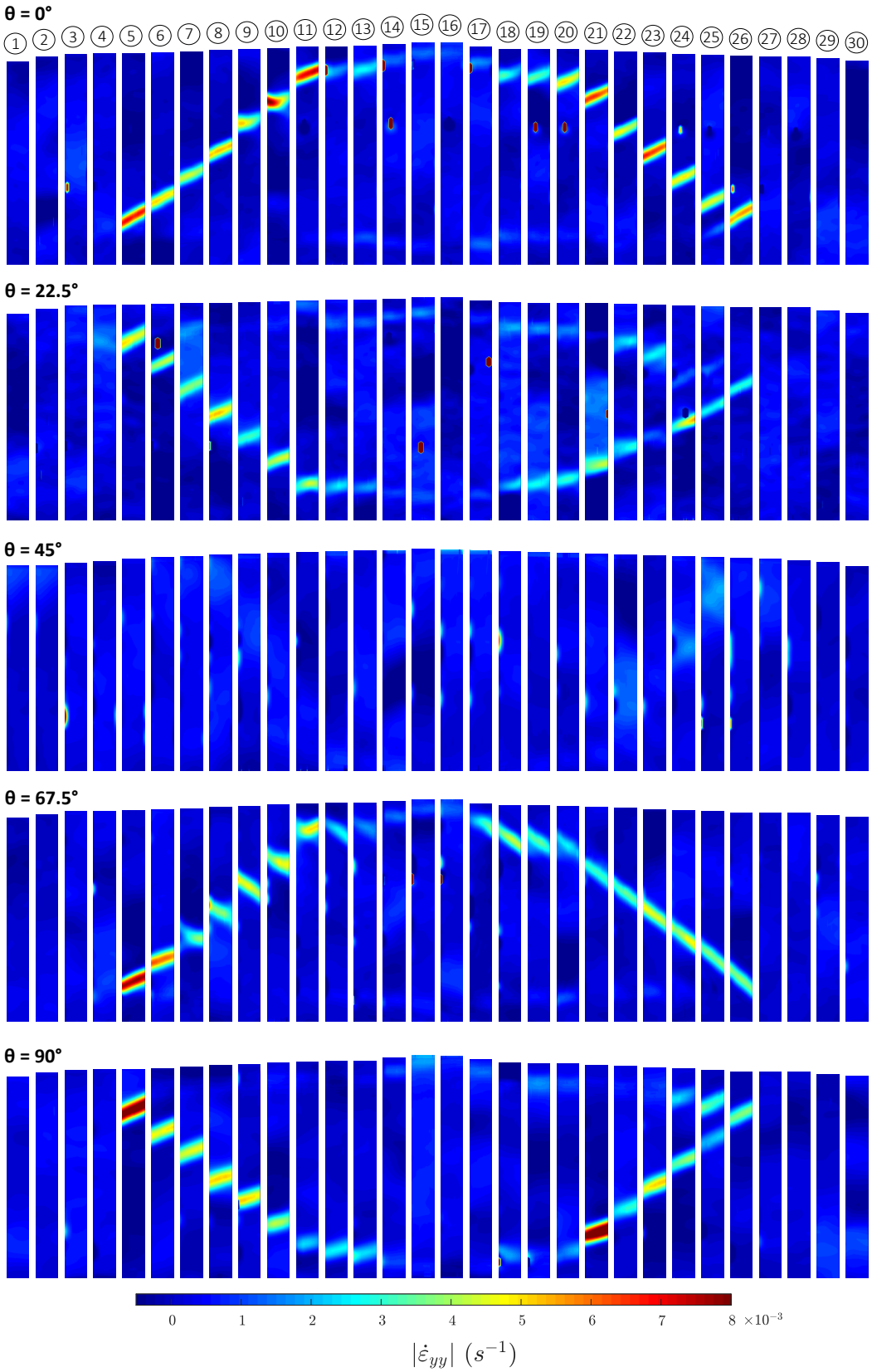

Figure 4.11: Longitudinal strain rate maps (absolute value of $\dot{\varepsilon}_{yy}$) of oriented samples under tensile load at 60°C.

4.4.3 Band angle measurement throughout loading and unloading

For the tensile orientations whose strain localize, the band angle was measured in all $\bar{\varepsilon}_{yy}$ range, during loading and unloading. Figure 4.12 shows the method used to measure the angle at each instant. The method consists in identifying the band in the $\dot{\varepsilon}_{yy}$ maps and performing a linear regression, where the linear coefficient is used to calculate the angle α between the band and the tensile orientation. Only the angles obtained from linear regressions with a coefficient of determination (R^2) higher than 95% are considered. Occasional secondary bands (appearing mostly during unloading) are disregarded in this analysis.

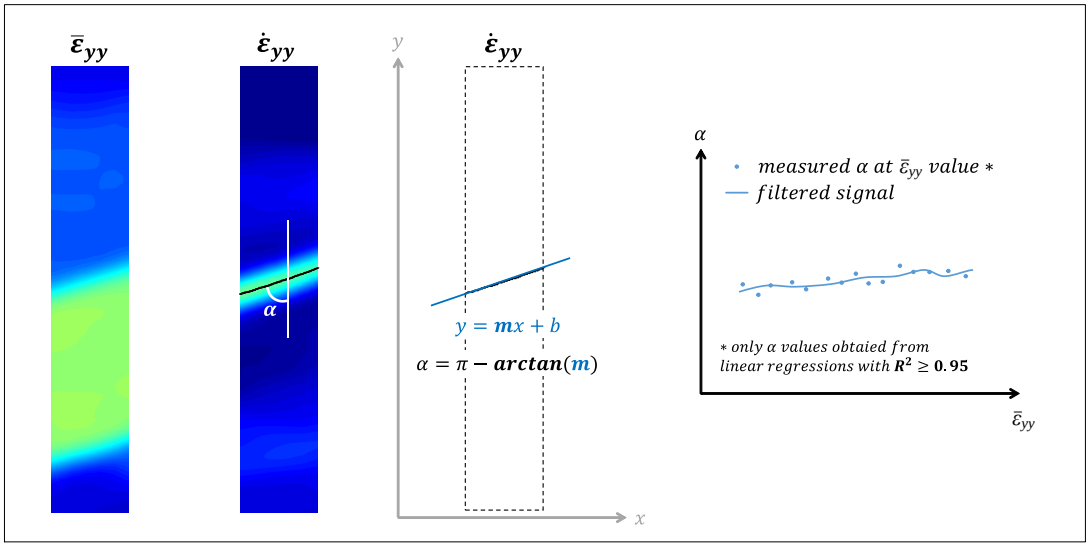

Figure 4.12: Method used to measure the angle α between the band and the tensile axis of samples.

The measured angles are presented in Fig. 4.13 for the three testing temperatures. The results show that the band angle is orientation dependent. At appearance, $\alpha(0°)$ and $\alpha(90°)$ are around 55°, which is a typical angle observed in NiTi localization bands and also is the predicted value when isotropy is assumed. Aside from the observed variations, in the other orientations the band angle is significantly smaller, appearing around values as low as $\alpha = 45°$. This is better observed during unloading, when the band is more stable.

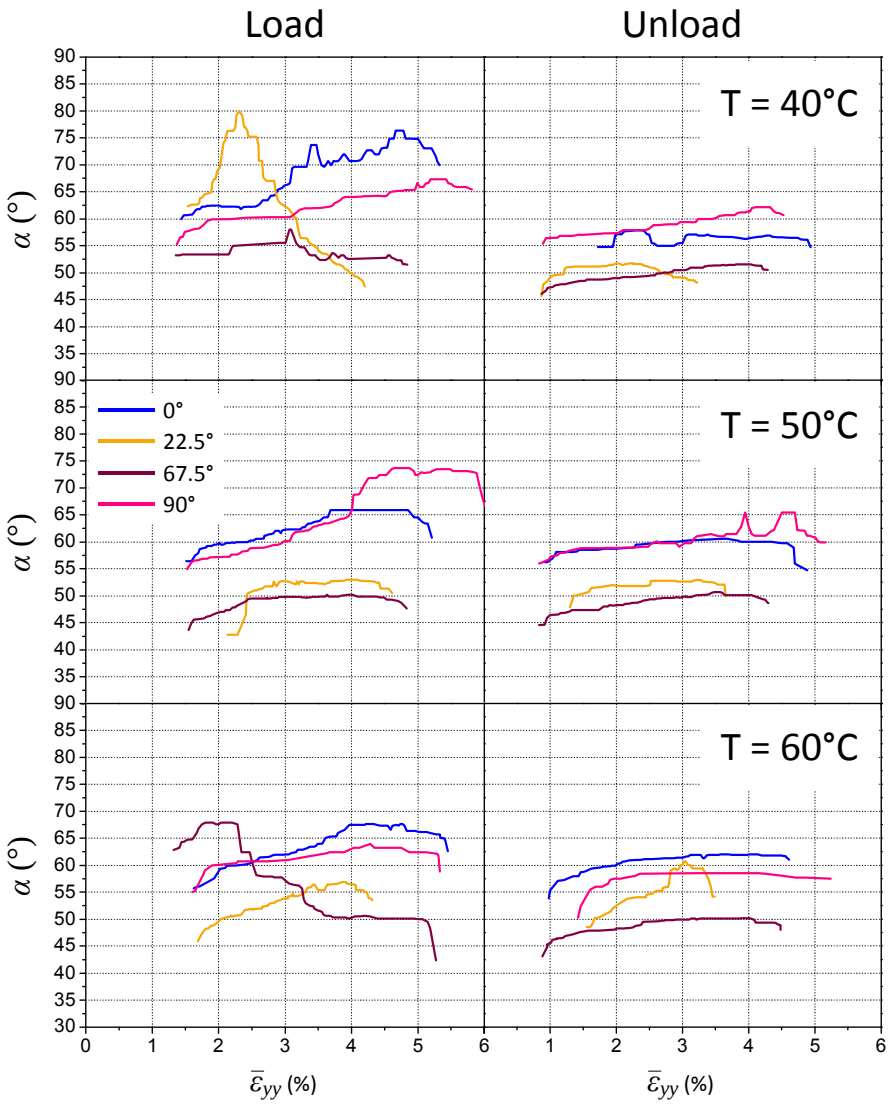

Figure 4.13: Evolution of the band angles with averaged longitudinal strain $\bar{\varepsilon}_{yy}$.

4.4.4 Band angle prediction using Hill theory

Hill plasticity theory is applied for the analysis of the band angle evolution during loading and unloading. Based on the approach presented in Section 4.2, the procedure employed is summarized as follows:

1. The r-coefficients at directions 0°, 45° and 90°, namely r_0, r_{45} and r_{90}, are calculated with Eq. 4.16 using experimental data.

2. Hill anisotropic coefficients in a plane stress state (F, G, H and N) are calculated using r_0, r_{45} and r_{90} (Eq. 4.19) and the transformation stress in the drawing direction as reference ($\sigma_Y = \sigma_{tr,0°} \rightarrow$ Eq. 4.4).

3. Once F, G, H and N are identified, the quadratic coefficients a, b and c are calculated with Eq. 4.24.

4. Finally, the band angle α and the tensile orientation θ are related through the Eq. 4.23.

4.4.4.1 Data treatment for the calculation of the r-coefficients

To assess the evolution of the band angle with strain, the r-coefficients are calculated throughout loading and unloading. Any significant variation of the r-coefficients is related with texture evolution during elongation (Savoie et al., 1995), which is an important feature that should be taken into account in numeric simulation (Aleksandrovic et al., 2009). Because of that, besides the required determination of r_0, r_{45} and r_{90}, the r-coefficients at 22.5° and 67.5° are calculated for analysis purposes.

Considering that Hill model only takes into account non-elastic deformation, elastic strain was subtracted. Equations 4.27 and 4.28 were used for longitudinal and transverse strains, respectively:

$$\varepsilon_{yy}^{in} = \bar{\varepsilon}_{yy} - (\Sigma_{yy}/E) \tag{4.27}$$

$$\varepsilon_{xx}^{in} = \bar{\varepsilon}_{xx} + \nu_{el}(\Sigma_{yy}/E) \tag{4.28}$$

where ε_{yy}^{in} and ε_{xx}^{in} are the inelastic strains in the y and x directions, respectively; Σ_{yy} is the nominal tensile stress; and E is the elastic modulus, calculated in Chapter 3 and equal to 70 GPa. ν_{el} is the elastic strain ratio (Poisson ratio). According to the strain ratio calculated in Section 4.4.1.1.b, a single value was chosen for all orientations: $\nu_{el} = 0.45$. The only exception is for $\theta = 45°$, to which the chosen value was $\nu_{el} = 0.60$.

Once inelastic strain is isolated, the ε_{yy}^{in} was normalized with the transformation strain $\Delta\varepsilon_{tr}$ of each orientation (averaged values from Fig. 3.9b). Considering a linear relation between transformation strain and deformation (Šittner et al., 2005; Stebner et al., 2015), this gives an estimation of the martensite fraction ($f_m = \varepsilon_{yy}^{in}/\Delta\varepsilon_{tr}$). Thus, the r-coefficients, and ultimately the band angle, are here shown in function of the martensite fraction.

Finally, the averaged strain rates in the longitudinal and transverse directions of samples were calculated using the data from Fig. 4.4. The result of this process is presented in Figure 4.14. It is seen that during stress plateau the averaged strain rate in the y-direction of the sample is somewhat constant, reaching around $\dot{\varepsilon}_{yy}^{in} = 4 \times 10^{-4}$ s^{-1}.

From the averaged $\dot{\varepsilon}_{xx}^{in}$ and $\dot{\varepsilon}_{yy}^{in}$ data the r-coefficients were calculated. The results are shown in Figure 4.15.

In Fig. 4.15 the fluctuation of the curves, specially at 0°, 22.5°, 67.5° and 90°, arise from the fluctuations of the strain rate curves. The variation up to $f_m = 0.05$ was removed because of excessive noise. Nevertheless, it is possible to say that the r-coefficient at 45° experiments the greatest change during both loading and unloading. When stretched in this orientation the material deforms more on the transverse direction than in the thickness direction. In the other orientations, despite the fluctuations on the curves the r-coefficients are mostly smaller or equal to unity, meaning that the material mostly thins under tensile stress. The unloading curves are similar due to the reversibility of the phase transformation.

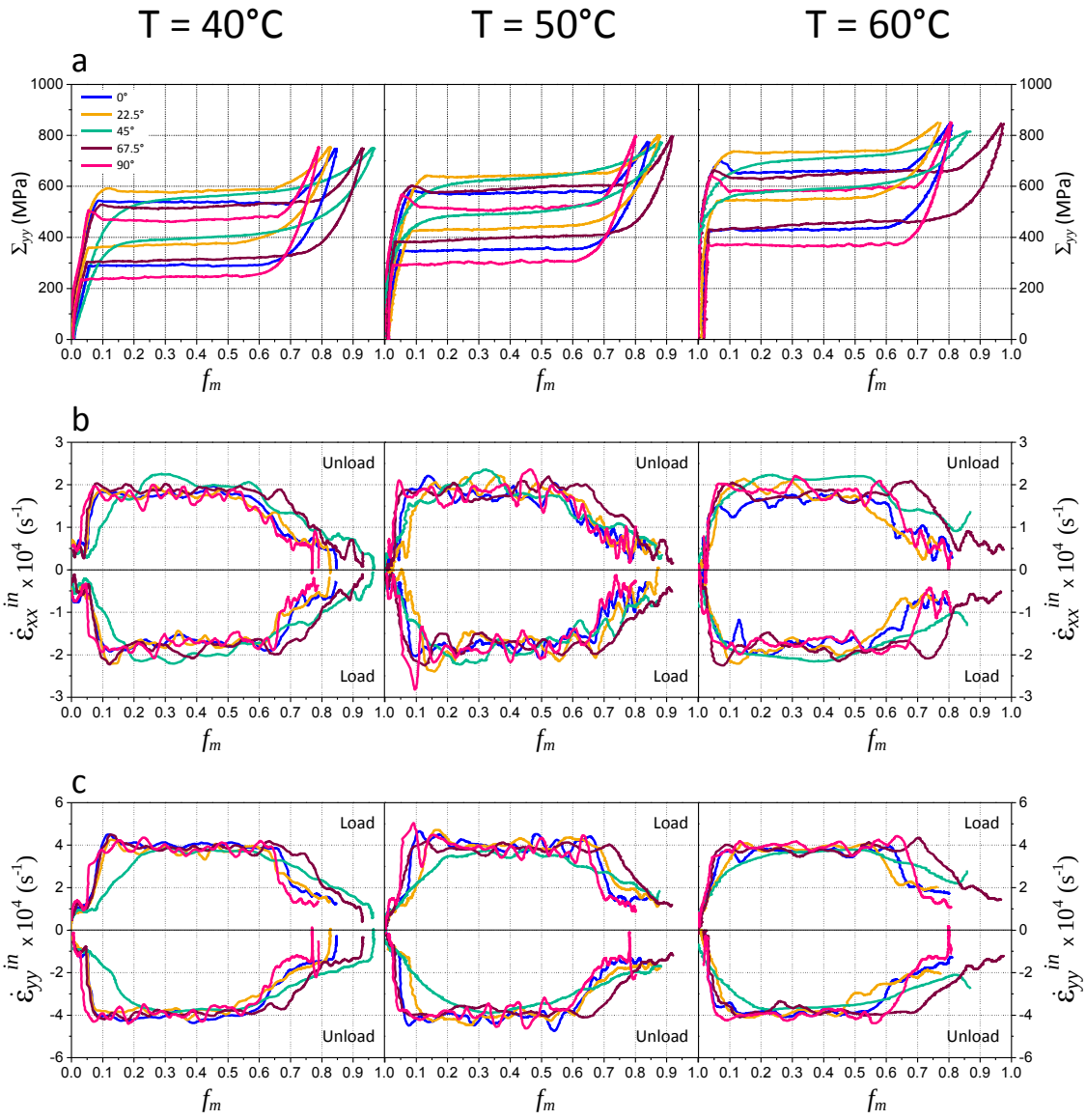

Figure 4.14: Evolution of averaged strain rates in the transverse and longitudinal directions of samples with martensite fraction.

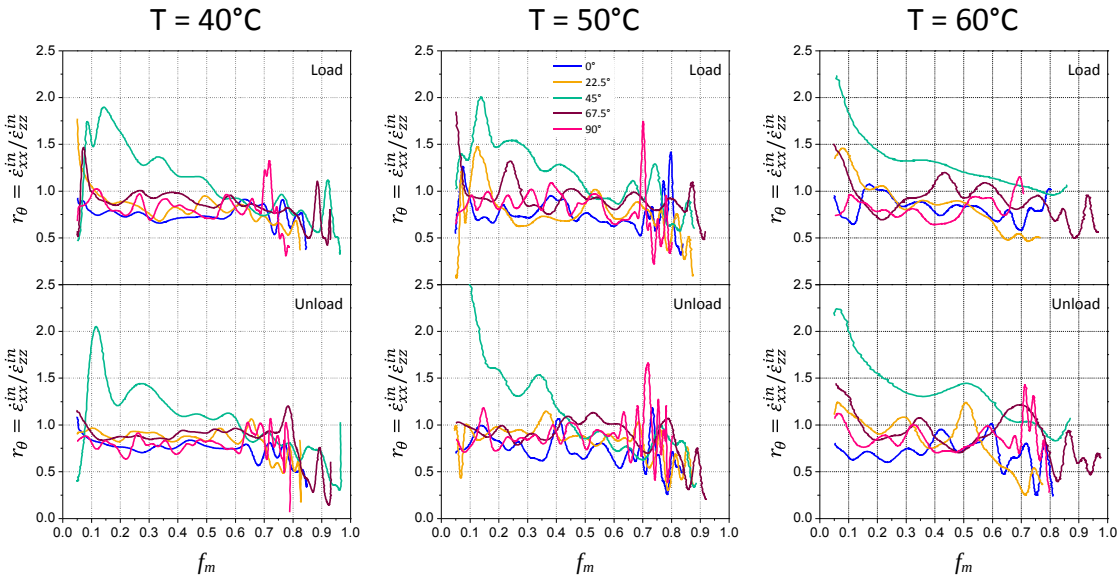

Figure 4.15: Evolution of r-coefficients with martensite fraction for loading and unloading.

4.4.4.2 Hill coefficients F, G, H and N

Hill 1948 anisotropic parameters were identified from r_0, r_{45} and r_{90} and the relation in Eq. 4.4, taking the transformation stress at 0° ($\sigma_{tr,0°}$) as reference stress σ_Y.

Figure 4.16 shows these four coefficients. Like the r-coefficients, no significant difference is seen between different test temperatures or between load and unload. Aside from some fluctuation, which arise from the variations observed in the averaged strain rate, the normal coefficients F, G and H are similar among themselves and approximately 0.5 for the entire range of f_m.

The shear coefficient N, however, decreases with increasing f_m. Around $f_m = 0.1$, $N = 2.5 = 5F = 5G = 5H$. According to Hill 1948 model, the anisotropy of the tube material is verified by the fact that $N \neq 3F = 3G = 3H$. This ratio is reached around $f_m = 0.6$, $f_m = 0.55$ and $f_m = 0.7$ for 40°C, 50°C and 60°C, respectively. From this point, the predominantly detwinned martensite formed under tension behave similarly in all orientations.

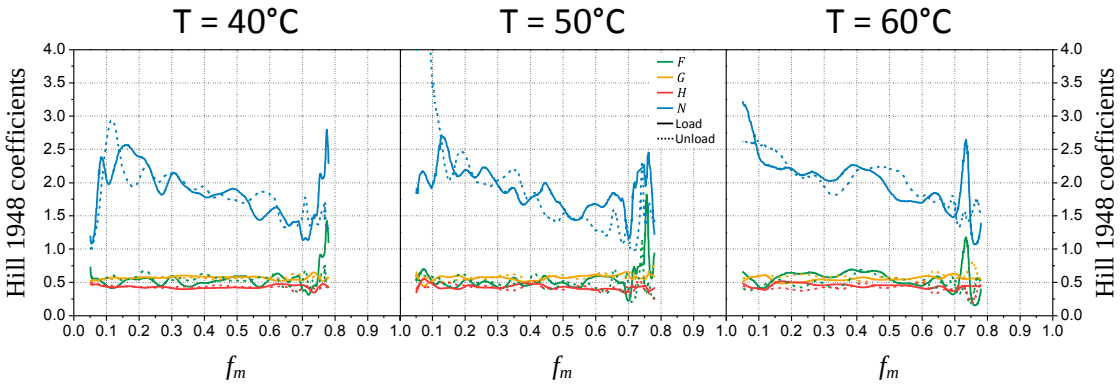

Figure 4.16: Hill 1948 anisotropic coefficients in function of martensite fraction.

4.4.4.2.a Transformation stress prediction and suitability of Hill 1948 criterion

The suitability of the anisotropic criterion is evaluated by its ability to predict the transformation stresses in the plane of the flattened NiTi tube. The prediction of $\sigma_{tr}(\theta)$ is performed inserting Hill anisotropic parameters in Eq. 4.13. The reference stress is taken in the drawing direction ($\sigma_Y = \sigma_{tr,0°}$).

According to results in Fig. 4.16, $F = G = H = 0.5$ and $2.5 < N < 1.5$, approximately. Three values of N were chosen to illustrate the effect of the shear parameter on the orientation dependence of $\sigma_{tr}(\theta)$. The effect can be observed in Fig. 4.17. When $N = 1.5$ there is no orientation dependence. As N increases, the stress in the directions involving shear becomes higher than the stress in the orthogonal directions (0° and 90°). The higher N is, the more orientation dependent $\sigma_{tr}(\theta)$ becomes.

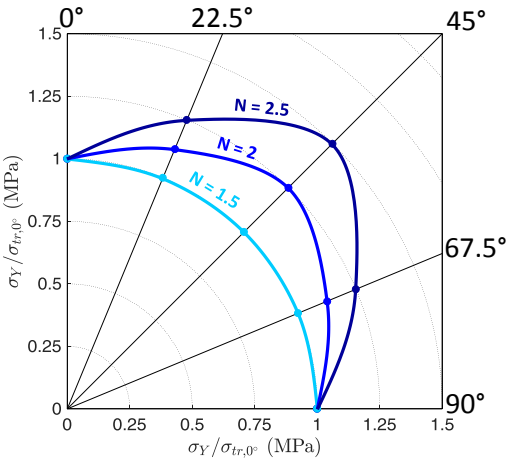

Figure 4.17: Effect of N on the orientation dependence of calculated transformation stress.

As defined in Chapter 3, the transformation stresses are taken at $f_m = 0.5$. Figure 4.18 compares the experimental transformation stresses to the predicted stresses at this martensite fraction.

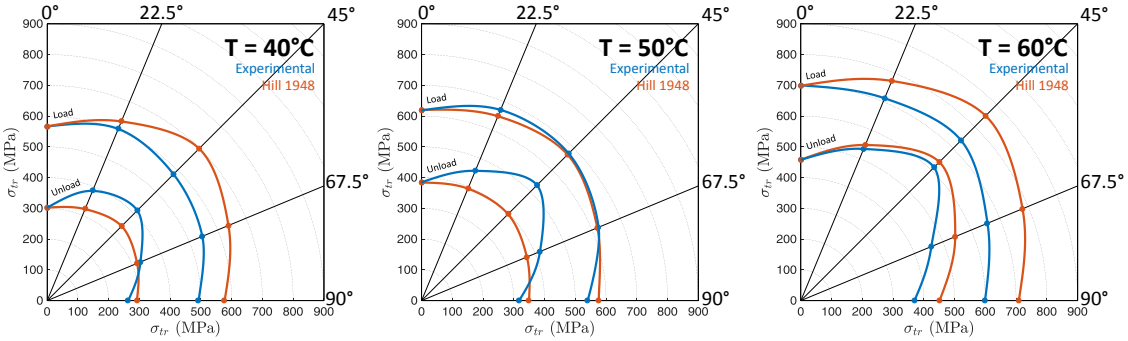

Figure 4.18: Comparison between transformation stresses measured experimentally and predicted by Hill 1948 yield criterion at $f_m = 0.5$.

Overall, the accuracy of the stress prediction is not very high for most tests (experimental and predicted stress values do not coincide), but the orientation dependence (the

form of the σ_{tr}-θ curve) is reasonably well predicted for some cases. Assuming an associative flow rule, the capacity of the yield function to predict the band angle is directly related to its capacity to predict the transformation stresses. Due to this observation, it is expected that Hill 1948 parameters will be able to predict well the orientation dependence of the band angles. However, the calculated band angle values might not agree with experiments at all martensite fractions.

4.4.4.3 Band angle (α)

With Hill anisotropic coefficients inserted in Eq. 4.24 the quadratic coefficients a, b and c are calculated and Eq. 4.23 can be solved for different values of θ. Figure 4.19 shows the band predictions.

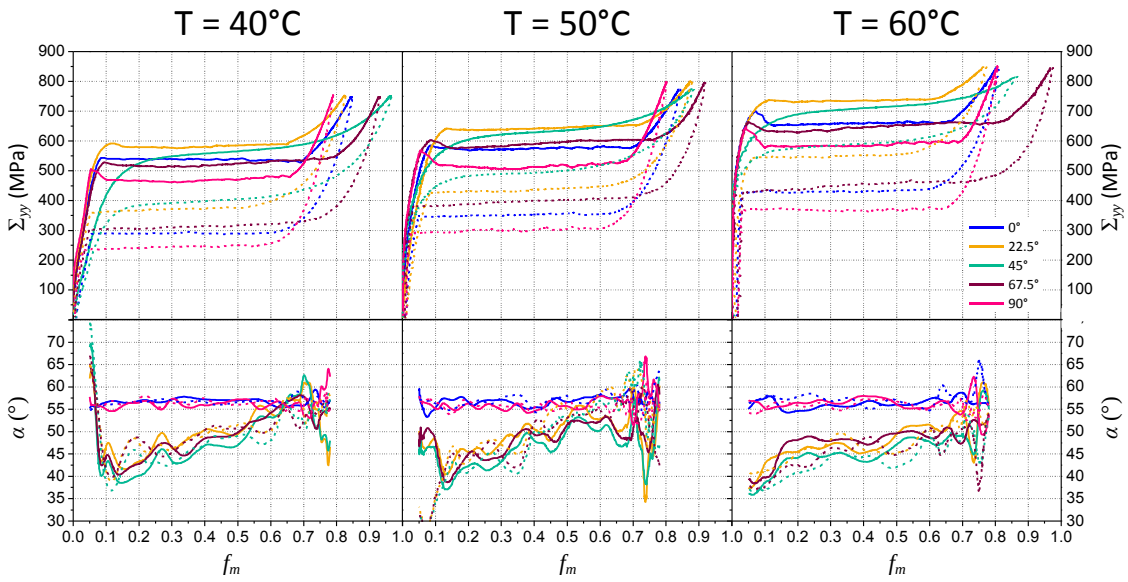

Figure 4.19: Band angle in function of martensite fraction for all orientations.

In the longitudinal and transverse directions, corresponding to 0° and 90°, α is approximately 55°. The predicted α in other orientations behave similarly among themselves, rising from $\approx 40°$ until $\approx 50°$ at the end of loading.

According to Eq. 4.24, the band angle in the two principal directions ($\theta = 0°$ and $\theta = 90°$) α is controlled uniquely by H because $a = H$, $b = 0$ and $c = a$. Since H is practically independent of the martensite fraction, so is α for these θ values. For other θ values shear strain is present and all four anisotropic parameters play a role in the estimation of α. It is seen in Fig. 4.20 that α follows the evolution of N, increasing as N decreases with martensite fraction.

Figure 4.20 compares the evolution of α measured from the strain maps and the ones predicted by Hill model. The comparison is performed for the unloading, where the experimental angles are more stable. The predicted values agree fairly well for the three temperatures at small martensite fractions (at a constant f_m value).

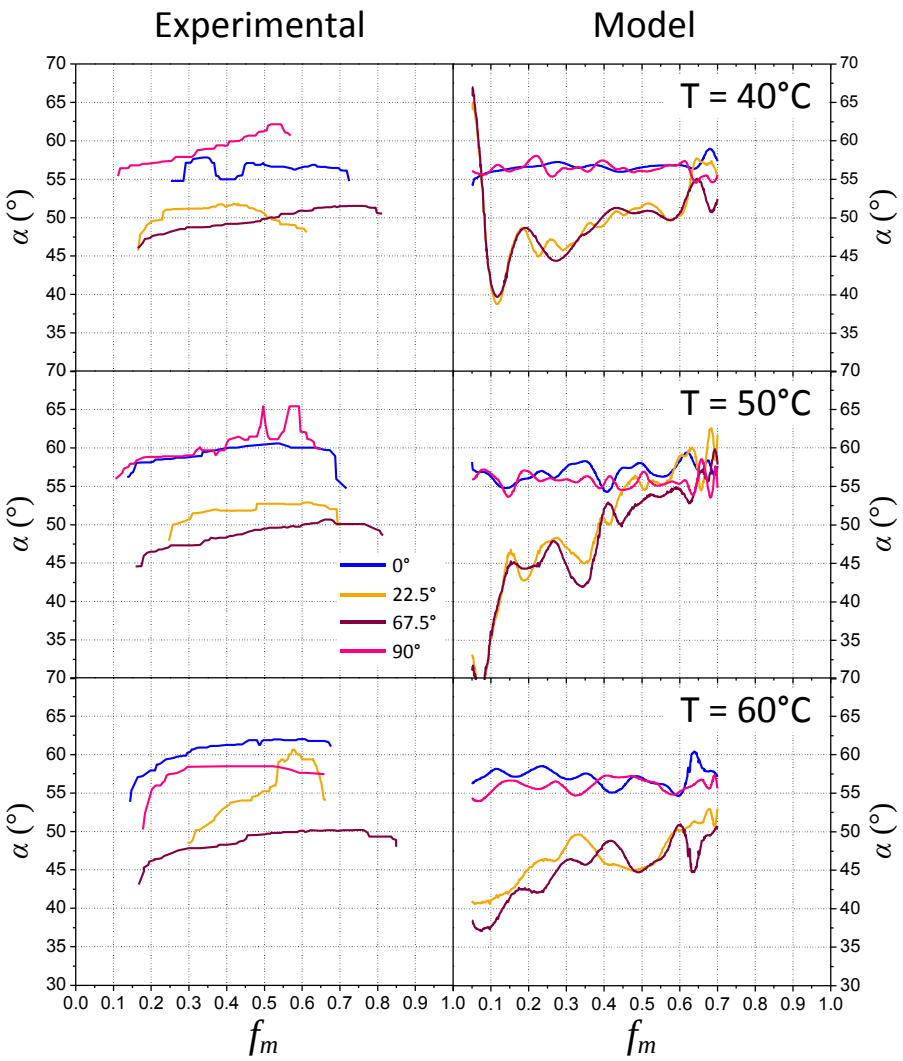

Figure 4.20: Comparison between band angle measured from strain maps and predicted by Hill strain localization model (unload).

4.5 Conclusion

The analysis of the strain distribution in the oriented tensile samples allowed to access some interesting aspects of the tube anisotropy. The experimental observations can be summarized as follows:

1. Strain localization occurred in all directions, except at $\theta = 45°$ from the tube drawing direction. This orientation seems to work as an approximate symmetry direction for the orientation dependence of the strain localization phenomenon.

2. In some cases, as soon as the band appears it starts changing the inclination, probably in an attempt to minimize the in-plane bending. The propagation of the band is a lot more stable during unloading.

3. The band angles along the orthotropic directions ($\theta = 0°$ and $\theta = 90°$) reached the highest values among orientations, around $55° - 60°$. Following a decreasing trend, the band angles at $\theta = 22.5°$ reach $\approx 53°$ when the band is stable. At last, $\theta = 67.5°$ present band angles as low as $45° - 50°$.

4. The absence of strain localization at $\theta = 45°$ allows to verify the evolution of strain increment ratios r-coefficients and ν_{xy} with martensite fraction. Both reach substantially higher values in this orientation.

From the experimental data, the band angle evolution was predicted using Hill theory of zero extension rate. Hill 1948 anisotropic function was used in the procedure of band angle prediction.

The evolution of Hill 1948 anisotropic parameters with martensite fraction show that for martensite fractions higher than at least 0.5 the tensile behaviour of the material, mostly composed of detwinned martensite, is similar in all orientations.

Furthermore, the zero extension rate theory is an effective means for accessing the band angles from averaged tensile stress-strain data at different martensite fractions. The predictions are in reasonable good agreement with experimental measurements. Allying the zero extension rate theory with Hill 1948 anisotropic function allowed to successfully simulate the orientation dependence of the band angle for the studied tensile directions in the tube.

GENERAL CONCLUSION AND PERSPECTIVES

This thesis work was an investigation about the anisotropy of a superelastic thin walled tube applied in the fabrication of self-expandable stents. The study addressed two issues:

- the effect of anisotropy on thermomechanical properties, such as transformation strain, transformation stresses and Clausius-Clapeyron coefficient;
- and the effect of anisotropy on the strain localization phenomenon during tensile tests.

For this, an experimental campaign was performed. Stress-strain curves and strain maps were obtained from tensile samples cut at five orientations in the plane of a flattened NiTi tube. The temperature dependence was also studied.

Thermomechanical properties

The bibliographical chapter showed that the tensile behaviour of textured polycrystalline NiTi is generally encompassed by the tensile behaviour of NiTi single crystals in the [100] and [111] directions. These two cases show opposite behaviour. The literature review also shows that in a NiTi tube the grains are distributed so that the [111] and [100] directions are best aligned with the drawing direction (0°) and with 45°, respectively (Barney et al., 2011).

In the present work, the tensile stress-strain curves showed that the studied properties are very orientation dependent. The effect of anisotropy causes an approximate symmetry with respect to 45°. The transverse direction (90°) is slightly softer than the drawing direction but their overall behaviour is similar. Furthermore, the stress-strain curves at 45° are the only that do not present a stress plateau.

The transverse direction reaches transformation strains that are more than twice higher than at 45°. The Clausius-Clapeyron coefficient, an important property accounting for the thermomechanical coupling of SMA, reaches a 50% increase between these two orientations. The transformation stress reaches a 40% increase.

The orientation dependence of stress hysteresis (difference between forward and reverse transformation stresses) is also strong and temperature dependent. This was analysed in detail with a thermodynamic approach based on the Gibbs free energy (Wollants et al., 1993). It was concluded that the classic Clausius-Clapeyron equation disregards an important contribution: the temperature dependence of irreversible energies. According to the analysis, this contribution is the responsible for the difference between the Clausius-Clapeyron coefficient of forward and reverse transformations.

The link between the temperature dependence of irreversible energy and the difference between Clausius-Clapeyron coefficients of forward and reverse transformations should be further investigated. The effect of NiTi alloy composition and the presence of precipitates could be examined to test different types of temperature dependence. Furthermore, the identified orientation and temperature dependencies are relevant for the calibration and validation of constitutive equations.

For future work it can be useful to characterize and analyze the thermomechanical behavior of the tube in other stress states like shear and compression. Because of the small thickness dimension of the tube, the compression characterization can be performed using bending tests and subtracting the tension component. Once experimentally characterized, it is possible to model the anisotropic behavior of the NiTi tube to go towards the optimization of the design and manufacturing process of self extensible stents.

Strain localization phenomenon

The bibliographical chapter also discussed how the strain distribution during phase transformation is closely related with the alignment of grains in polycrystalline materials. Texture investigations addressing the tension-compression asymmetry in NiTi alloys illustrate this relation (Barney et al., 2011; Mao et al., 2010). The differences between the behaviour of [111] and [100] directions are also perceived in the propagation mode of phase transformation (Creuziger et al., 2008).

Of all the studied orientations in the thin walled NiTi tube, the 45° direction was the only one that showed no strain localization. This was confirmed by the homogeneous strain rate maps calculated for this orientation.

For the samples that show strain localization, a more detailed analysis concerning the transformation band was performed. No significant difference is detected in the morphology of the band among orientations. The angle between the band and the tensile direction, however, is orientation dependent. It reaches higher values in the tensile tests along the drawing and transverse directions, followed by 22.5° and then by 67.5°. This orientation dependence was more evident during unloading, when the band angle was more stable.

The orientation dependence of the band angle and its evolution with martensite fraction was further analysed with a plasticity approach for localized necking developed by Hill (1948, 1952, 1950). The predicted band angles are in reasonably good agreement with experimental measurements. The predictions resulted in band angles that are less orientation dependent as the martensite fraction increases.

A suggestion for future work is to identify a flow rule more adapted to the behavior of the NiTi tube to study the localization phenomenon in states of stress different from the tension.

BIBLIOGRAPHY

Adharapurapu, R. R., F. Jiang, J. F. Bingert, and K. S. Vecchio (2010). "Influence of cold work and texture on the high-strain-rate response of Nitinol". In: *Materials Science and Engineering: A* 527.20, pp. 5255–5267.

Aleksandrovic, S., M. Stefanovic, D. Adamovic, and V. Lazic (2009). "Variation of normal anisotropy ratio r during plastic forming". In: *Strojniski Vestnik/Journal of Mechanical Engineering* 55.6, pp. 392–399.

Alonso, T. (2015). "Caracterisation par essais DMA et optimisation du comportement thermomecanique de fils de NiTi - Application a une aiguille medicale deformable". PhD thesis. Université Grenoble Alpes.

Ananthan, V. S. and E. O. Hall (1991). "Macroscopic aspects of Lüders band deformation in mild steel". In: *Acta Metallurgica Et Materialia* 39.12, pp. 3153–3160.

Aretz, H. (2007). "Numerical analysis of diffuse and localized necking in orthotropic sheet metals". In: *International journal of plasticity* 23, pp. 798–840.

Aun, D. P., M. Houmard, M. Mermoux, L. Latu-Romain, J. C. Joud, G. Berthomé, and V. T. L. Buono (2016a). "Development of a flexible nanocomposite TiO2 film as a protective coating for bioapplications of superelastic NiTi alloys". In: *Applied Surface Science* 375, pp. 42–49.

Aun, D. P., I. F. D. C. Peixoto, M. Houmard, and V. T. L. Buono (2016b). "Enhancement of NiTi superelastic endodontic instruments by TiO2 coating". In: *Materials Science and Engineering C* 68, pp. 675–680.

Banabic, D. (2010). "Plastic Behaviour of Sheet Metal". In: *Sheet Metal Forming Processes*, p. 301. arXiv: `arXiv:1011.1669v3`.

Bao, C., M. Francois, and L. Le Joncour (2016). "A Closer Look at the Diffuse and Localised Necking of A Metallic Thin Sheet: Evolution of the Two Bands Pattern". In: *Strain* 52.3, pp. 244–260.

Barata da Rocha, A., F. Barlat, and J. M. Jalinier (1985). "Prediction of the Forming Limit Diagrams of Anisotropic Sheets in Linear and Non-linear Loading". In: *Materials Science and Engineering* 68, pp. 151–164.

Barney, M. M., D Xu, S. W. Robertson, V Schroeder, R. O. Ritchie, a. R. Pelton, and A Mehta (2011). "Impact of thermomechanical texture on the superelastic response of Nitinol implants." In: *Journal of the mechanical behavior of biomedical materials* 4.7, pp. 1431–9.

Bechle, N. J. and S. Kyriakides (2016). "Evolution of localization in pseudoelastic NiTi tubes under biaxial stress states". In: *International Journal of Plasticity* 82, pp. 1–31.

Bechle, N. J. and S. Kyriakides (2014). "Localization in NiTi tubes under bending". In: *International Journal of Solids and Structures* 51.5, pp. 967–980.

Benafan, O, S. A. P. Ii, R. D. Noebe, D. W. Brown, and B Clausen (2013). "An in situ neutron diffraction study of shape setting shape memory NiTi". In: *Acta Materialia* 61.10, pp. 3585–3599.

Bonsignore, C (2004). "A Decade of Evolution in Stent Design". In: *Proceedings of the International Conference on Shape memory and Superelastic Technologies*. Ed. by A. R. Pelton and T. W. Duerig. Pacific Grove, California, USA.

Brill, T. M., S Mittelbach, W Assmus, M Mullner, and B Luthi (1991). "Elastic properties of NiTi". In: *Journal of Physics: Condensed Matter* 3.48, pp. 9621–9627.

Brinson, L. C., I. Schmidt, and R. Lammering (2004). "Stress-induced transformation behavior of a polycrystalline NiTi shape memory alloy : micro and macromechanical investigations via in situ optical microscopy". In: *Journal of the Mechanics and Physics of Solids* 52, pp. 1549–1571.

Cazacu, O., B. Plunkett, and F. Barlat (2006). "Orthotropic yield criterion for hexagonal closed packed metals". In: *International Journal of Plasticity* 22.7, pp. 1171–1194.

Chen, L., W. Wen, and H. Cui (2013). "Generalization of Hill's yield criterion to tension-compression asymmetry materials". In: *Science China Technological Sciences* 56.1, pp. 89–97.

Cottrell, A. H. and B. A. Bilby (1949). "Dislocation theory of yielding and strain ageing of iron". In: *Proceedings of the Physical Society. Section A* 62.1, pp. 49–62. arXiv: `arXiv:1011.1669v3`.

Creuziger, A., L. J. Bartol, K. Gall, and W. C. Crone (2008). "Fracture in single crystal NiTi". In: *Journal of the Mechanics and Physics of Solids* 56.9, pp. 2896–2905.

Delobelle, V. (2012). "Contribuitions à l'étude thermomécanique des alliages à memoire de forme NiTi et à la réalisation par soudage e matériaux architecturés NiTi". PhD thesis. Université de Grenoble.

Dennis, R. and J. Tu (2008). "Development of a localized heat treatment system for shape memory alloy wires using an ytterbium fiber laser". In: *Journal of Materials Processing Technology* 199.1-3, pp. 245–255.

Duerig, T, A Pelton, and D Stöckel (1999). "An overview of nitinol medical applications". In: *Materials Science and Engineering: A* 273-275, pp. 149–160.

Duerig, T. W., K. N. Melton, D Stöckel, and C. M. Wayman (1990). *Engineering Aspects of Shape Memory Alloys*. Vol. 1. Butterworth-Heinemann, pp. 3–20.

Elibol, C. and M. F. Wagner (2015). "Strain rate effects on the localization of the stress-induced martensitic transformation in pseudoelastic NiTi under uniaxial tension, compression and compression-shear". In: *Materials Science and Engineering A* 643, pp. 194–202.

Favier, D and L. Orgéas (1998). "Stress-induced transformation of a NiTi alloy in isothermal shear, tension and compression". In: *Acta Materialia* 46.15, pp. 5579–5591.

Favier, D., H. Louche, P. Schlosser, L. Orgéas, P. Vacher, and L. Debove (2007). "Homogeneous and heterogeneous deformation mechanisms in an austenitic polycrystalline Ti-50.8 at.% Ni thin tube under tension. Investigation via temperature and strain fields measurements". In: *Acta Materialia* 55.16, pp. 5310–5322.

Favier, D., Y. Liu, L. Orgéas, A. Sandel, L. Debove, and P. Comte-Gaz (2006). "Influence of thermomechanical processing on the superelastic properties of a Ni-rich Nitinol shape memory alloy". In: *Materials Science and Engineering A* 429.1-2, pp. 130–136.

Feng, P and Q. P. Sun (2006). "Experimental investigation on macroscopic domain formation and evolution in polycrystalline NiTi microtubing under mechanical force". In: *Journal of the Mechanics and Physics of Solids* 54.8, pp. 1568–1603.

Gall, K., H. Sehitoglu, Y. I. Chumlyakov, and I. V. Kireeva (1999). "Tension-compression asymmetry of the stress-strain response in aged single crystal and polycrystalline NiTi". In: *Acta Materialia* 47.4, pp. 1203–1217.

Gall, K., J. Tyber, V. Brice, C. P. Frick, H. J. Maier, and N. Morgan (2005). "Tensile deformation of NiTi wires". In: *Journal of Biomedical Materials Research - Part A* 75.4, pp. 810–823.

Gall, K., H. Sehitoglu, Y. I. Chumlyakov, Y. L. Zuev, and I. Karaman (1998). "The role of coherent precipitates in martensitic transformations in single crystal and polycrystalline Ti-50.8at%Ni". In: *Scripta Materialia* 39.6, pp. 699–705.

Gao, S and S Yi (2003). "Experimental study on the anisotropic behavior of textured NiTi pseudoelastic shape memory alloys". In: *Materials Science And Engineering A* 362, pp. 107–111.

Gurao, N. P. and S. Suwas (2013). "Deformation behaviour at macro- and nano-length scales: The development of orientation gradients". In: *Materials Letters* 99, pp. 81–85.

Hallai, J. F. and S. Kyriakides (2013). "Underlying material response for Lüders-like instabilities". In: *International Journal of Plasticity* 47, pp. 1–12.

Hamilton, R. F., H Sehitoglu, Y. I. Chumlyakov, and H. Maier (2004). "Stress dependence of the hysteresis in single crystal NiTi alloys". In: *Acta Materialia* 52, pp. 3383–3402.

Hill, R. (1948). "A theory of the yielding and plastic flow of anisotropic metals". In: *Proceedings of the Royal Society of London A* 193.1033, pp. 281–297.

— (1952). "On discontinuous reference plastic states, with special to localized necking in thin sheets". In: *Journal of the Mechanics and Physics of Solids* 1, pp. 19–30.

— (1950). "Plastic anisotropy". In: *The mathematical theory of plasticity*. Trowbridge: Redwood Books Ltd. Chap. XII, p. 355.

Huang, J., P. Dong, W. Hao, T. Wang, Y. Xia, G. Da, and Y. Fan (2014). "Biocompatibility of TiO2 and TiO2/heparin coatings on NiTi alloy". In: *Applied Surface Science* 313, pp. 172–182.

Iadicola, M. A. and J. A. Shaw (2004). "Rate and thermal sensitivities of unstable transformation behavior in a shape memory alloy". In: *International Journal of Plasticity* 20.4-5, pp. 577–605.

Inoue, H., N. Miwa, and N. Inakazu (1996). "Texture and shape memory strain in TiNi alloy sheets". In: *Acta Materialia* 44.12, pp. 4825–4834.

Jani, J. M., M. Leary, A. Subic, and M. A. Gibson (2014). "A review of shape memory alloy research, applications and opportunities". In: *Materials & Design* 56, pp. 1078–1113.

Jiang, D., S. Kyriakides, C. M. Landis, and K. Kazinakis (2017). "Modeling of propagation of phase transformation fronts in NiTi under uniaxial tension". In: *European Journal of Mechanics, A/Solids* 64, pp. 131–142.

Kato, H. and K. Sasaki (2013). "Transformation-induced plasticity as the origin of serrated flow in an NiTi shape memory alloy". In: *International Journal of Plasticity* 50, pp. 37–48.

Khan, A. S. and S. Huang (1995). *Continuum theory of plasticity*. Westfield, NJ: John Wiley & Sons, Inc., p. 421.

Kim, K. and S. Daly (2013). "The effect of texture on stress-induced martensite formation in nickel–titanium". In: *Smart Materials and Structures* 22.7, p. 075012.

Kleine, K. F. and K. G. Watkins (2003). "Fiber laser for micro-cutting of metals". In: *Photonics West*. January. San jose, CA, USA, p. 184.

Krishnan, S. A., A. Baranwal, A. Moitra, G. Sasikala, S. K. Albert, A. K. Bhaduri, G. A. Harmain, T. Jayakumar, and E. R. Kumar (2014). "Assessment of deformation field during high strain rate tensile tests of RAFM steel using DIC technique". In: *Procedia Engineering* 86, pp. 131–138.

Lagoudas, D. C. (2008). *Shape Memory Alloys: Modeling and Engineering Applications*, p. 435. arXiv: `arXiv:1011.1669v3`.

Laplanche, G., T. Birk, S. Schneider, J. Frenzel, and G. Eggeler (2017). "Effect of temperature and texture on the reorientation of martensite variants in NiTi shape memory alloys". In: *Acta Materialia* 127, pp. 143–152.

Leo, P, T. W. Shield, and P Bruno (1993). "Transient Heat Transfer Effects on the Pseudoelastic Behavior of Shape Memory Wires". In: *Acta Metallurgica et Materialia* 41.8, pp. 2477–2485.

Linardon, C, D Favier, G Chagnon, and B Gruez (2014). "A conical mandrel tube drawing test designed to assess failure criteria". In: *Journal of Materials Processing Tech.* 214.2, pp. 347–357.

Linardon, C. (2014). "Precision tube drawing for biomedical applications : Theoretical, Numerical and Experimental study Precision Tube Drawing for Biomedical Applications : Theoretical, Numerical and Experimental Study". PhD thesis.

Liu, L., D. B. Li, Y. F. Tong, and Y. F. Zhu (2016). "Fiber laser micromachining of thin NiTi tubes for shape memory vascular stents". In: *Applied Physics A: Materials Science and Processing* 122.7, pp. 1–9.

Liu, X., Y. Wang, D. Yang, and M. Qi (2008). "The effect of ageing treatment on shape-setting and superelasticity of a nitinol stent". In: *Materials Characterization* 59.4, pp. 402–406.

Liu, Y., Z. Xie, J. Van Humbeeck, and L. Delaey (1999). "Effect of texture orientation on the martensite deformation of NiTi shape memory alloy sheet". In: *Acta Materialia* 47.2, pp. 645–660.

Liu, Y. and H. Xiang (1998). "Apparent modulus of elasticity of near-equiatomic NiTi". In: *Journal of Alloys and Compounds* 270, pp. 154–159.

Liu, Y. and H. Yang (2007). "Strain dependence of the Clausius–Clapeyron relation for thermoelastic martensitic transformations in NiTi". In: *Smart Materials and Structures* 16.1, S22–S27.

Liu, Y. (2015). "The superelastic anisotropy in a NiTi shape memory alloy thin sheet". In: *Acta Materialia*.

Mao, S. C., X. D. Han, Z. Zhang, and M. H. Wu (2007). "The nano- and mesoscopic cooperative collective mechanisms of inhomogenous elastic-plastic transitions in polycrystalline TiNi shape memory alloys". In: *Journal of Applied Physics* 101.10.

Mao, S., J. Luo, Z. Zhang, M. Wu, Y. Liu, and X. Han (2010). "EBSD studies of the stress-induced B2–B19 martensitic transformation in NiTi tubes under uniaxial tension and compression". In: *Acta Materialia* 58.9, pp. 3357–3366.

Meng, H., J. Liao, Y. Zhou, and Q. Zhang (2009). "Laser micro-processing of cardiovascular stent with fiber laser cutting system". In: *Optics and Laser Technology* 41.3, pp. 300–302.

Meschel, S., J. Pavlu, and P. Nash (2011). "The thermochemical behavior of some binary shape memory alloys by high temperature direct synthesis calorimetry". In: *Journal of Alloys and Compounds* 509.17, pp. 5256–5262.

Miyazaki, S. and K. Otsuka (1986). "Deformation and Transition Behavior Associated with the R-Phase in Ti-Ni Alloys". In: *Metallurgical Transaction A* 17.January, pp. 53–63.

Miyazaki, S., Y. Ohmi, K. Otsuka, and Y. Suzuki (1982). "Characteristics of deformation and transformation pseudoelasticity in Ti-Ni alloys". In: *Le Journal de Physique Colloques* 43.C4, pp. 255–260.

Miyazaki, S., S. Kimura, K. Otsuka, and Y. Suzuki (1984). "The habit plane and transformation strains associated with the martensitic transformation in Ti-Ni single crystals". In: *Scripta Metallurgica* 18.9, pp. 883–888.

Miyazaki, S., K. Otsuka, and Y. Suzuki (1981). "Tranformation pseudoelasticity and deformation behavior in a Ti-50.6at%Ni alloy". In: *Scripta Metallurgica* 15.4, pp. 287–292.

Ortín, J. and A. Planes (1988). "Thermodynamic analysis of thermal measurements in thermoelastic martensitic transformations". In: *Acta Metallurgica* 36.8, pp. 1873–1889.

— (1991). "Thermodynamics and Hysteresis Behaviour of Thermoelastic Martensitic Transformations". In: *Le Journal de Physique IV* 01.C4, pp. 13–23.

— (1989). "Thermodynamics of Thermoelastic Martensitic Transformations". In: *Acta Metallurgica* 37.5, pp. 1433–1441.

Otsuka, K. and X. Ren (2005). "Physical metallurgy of Ti–Ni-based shape memory alloys". In: *Progress in Materials Science* 50.5, pp. 511–678.

Otsuka, K. and K. Shimizu (1986). "Pseudoelasticity and shape memory effects in alloys". In: *International Metals Reviews* 31.1, pp. 93–114.

Otsuka, K. and C. M. Wayman (1998). *Shape Memory Materials*. Ed. by K. Otsuka and C. M. Wayman, p. 284.

Otubo, J., O. Rigo, a.a. Coelho, C. Neto, and P. Mei (2008). "The influence of carbon and oxygen content on the martensitic transformation temperatures and enthalpies of NiTi shape memory alloy". In: *Materials Science and Engineering: A* 481-482, pp. 639–642.

Palengat, M, G Chagnon, D Favier, H Louche, C Linardon, and C Plaideau (2013). "Cold drawing of 316L stainless steel thin-walled tubes : Experiments and finite element analysis". In: *International Journal of Mechanical Sciences* 70, pp. 69–78.

Pelton, A. R., B. Clausen, and A. P. Stebner (2015). "In Situ Neutron Diffraction Studies of Increasing Tension Strains of Superelastic Nitinol". In: *Shape Memory and Superelasticity* 1.3, pp. 375–386.

Pfeifer, R., D. Herzog, M. Hustedt, and S. Barcikowski (2010). "Pulsed Nd:YAG laser cutting of NiTi shape memory alloys—Influence of process parameters". In: *Journal of Materials Processing Technology* 210.14, pp. 1918–1925.

Pieczyska, E. A., S. P. Gadaj, W. K. Nowacki, and H. Tobushi (2006). "Phase-Transformation Fronts Evolution for Stress- and Strain-Controlled Tension Tests in TiNi Shape Memory Alloy". In: *Experimental Mechanics* 46.4, pp. 531–542.

Plunkett, B., O. Cazacu, and F. Barlat (2008). "Orthotropic yield criteria for description of the anisotropy in tension and compression of sheet metals". In: *International Journal of Plasticity* 24.5, pp. 847–866.

Polatidis, E., N. Zotov, E. Bischoff, and E. J. Mittemeijer (2015). "The effect of cyclic tensile loading on the stress-induced transformation mechanism in superelastic NiTi alloys: An in-situ X-ray diffraction study". In: *Scripta Materialia* 100, pp. 59–62.

Poncin, P and J Proft (2003). "Stent Tubing: Understanding the Desired Attributes". In: *In: Proceedings of ASM Conference on Materials Processes for Medical Devices*. September, pp. 253–259.

Rajagopalan, S., A. L. Little, M. A. Bourke, and R. Vaidyanathan (2005). "Elastic modulus of shape-memory NiTi from in situ neutron diffraction during macroscopic loading, instrumented indentation, and extensometry". In: *Applied Physics Letters* 86.8, pp. 1–3.

Reedlunn, B., C. B. Churchill, E. E. Nelson, J. a. Shaw, and S. H. Daly (2014). "Tension, compression, and bending of superelastic shape memory alloy tubes". In: *Journal of the Mechanics and Physics of Solids* 63.1, pp. 506–537.

Robertson, S. W., V. Imbeni, H. R. Wenk, and R. O. Ritchie (2005). "Crystallographic texture for tube and plate of the superelastic/shape- memory alloy Nitinol used for endovascular stents". In: *Journal of Biomedical Materials Research - Part A* 72.2, pp. 190–199.

Robertson, S. W., X. Y. Gong, and R. O. Ritchie (2006). "Effect of product form and heat treatment on the crystallographic texture of austenitic Nitinol". In: *Journal of Materials Science* 41, pp. 621–630.

Ryhänen, J., E. Niemi, W. Serlo, E. Niemela, P. Sandvik, H. Pernu, and T. Salo (1997). "Biocompatibility of nickel-titanium shape memory metal and its corrosion behavior in human cell cultures". In: *Journal of Biomedical Materials Research* 35.4, pp. 451–457.

Ryhänen, J., M. Kallioinen, J. Tuukkanen, J. Junila, E. Niemelä, P. Sandvik, and W. Serlo (1998). "In vivo biocompatibility evaluation of nickel-titanium shape memory metal alloy: Muscle and perineural tissue responses and encapsule membrane thickness". In: *Journal of Biomedical Materials Research* 41.3, pp. 481–488.

Savoie, J., J. J. Jonas, S. R. Macewen, and R. Perrin (1995). "Evolution of r-Value During the Tensile Deformation of Aluminium". In: *Textures and Microstructures* 23.3, pp. 149–171.

Schlosser, P. (2008). "Influence des aspects mécaniques et thermiques sur les mécanismes de déformation d'alliages NiTi Influence of thermal and mechanical aspects on deformation behaviour of NiTi alloys". PhD thesis. Université Joseph Fourier Grenoble.

Sedmak, P., J. Pilch, L. Heller, J. Kopecek, J. Wright, P. Sedlak, M. Frost, and P. Sittner (2016a). "Grain-resolved analysis of localized deformation in nickel-titanium wire under tensile load". In: *Science* 353, pp. 559–562.

— (2016b). "Grain-resolved analysis of localized deformation in nickel-titanium wire under tensile load". In: *Science* 353, pp. 2–28.

Sehitoglu, H., R. Anderson, I. Karaman, K. Gall, and Y. Chumlyakov (2001). "Cyclic deformation behavior of single crystal NiTi". In: *Materials Science and Engineering A* 314.1-2, pp. 67–74.

Shaw, J. and S. Kyriakides (1998). "Initiation and propagation of localized deformation in elasto-plastic strips under uniaxial tension". In: *International Journal of Plasticity* 13.10, pp. 837–871.

Shaw, J. and S. Kyriakides (1997). "On the nucleation and propagation of phase transformation fronts in a NiTi alloy". In: *Acta Materialia* 45.2, pp. 683–700.

Shaw, J. A. and S. Kyriakides (1995). "Thermomechanical aspects of NiTi". In: *Journal of the Mechanics and Physics of Solids* 43.8, pp. 1243–1281.

Šittner, P. and V. Novák (2000). "Anisotropy of martensitic transformations in modeling of shape memory alloy polycrystals". In: *International Journal of Plasticity* 16, pp. 1243–1268.

Šittner, P., Y. Liu, and V Novak (2005). "On the origin of Lüders-like deformation of NiTi shape memory alloys". In: *Journal of the Mechanics and Physics of Solids* 53.8, pp. 1719–1746.

Šittner, P., M. Landa, P. Lukáš, and V. Novák (2006). "R-phase transformation phenomena in thermomechanically loaded NiTi polycrystals". In: *Mechanics of Materials* 38.5-6, pp. 475–492.

Sotomayor, A. D. A. and E. J. Herrera (1994). "Permanent elimination of the yield-point phenomenon in AISI 430 stainless steel by skin-pass rolling". In: *Journal of Materials Science* 29.22, pp. 5833–5838.

Sowerby, R. and W. Johnson (1975). "A Review of Texture and Anisotropy in Relation to Metal Forming R." In: *Materials Science and Engineering* 20.1, pp. 101–111.

Stebner, A. P., H. M. Paranjape, B. Clausen, L. C. Brinson, and A. R. Pelton (2015). "In Situ Neutron Diffraction Studies of Large Monotonic Deformations of Superelastic Nitinol". In: *Shape Memory and Superelasticity* 1.2, pp. 252–267.

Stoeckel, D. (1995). "The Shape Memory Effect - Phenomenon, Alloys, and Applications". In: *Shape Memory Alloys for Power Systems EPRI*, pp. 1–13.

Sun, Q. P. and Z. Q. Li (2002). "Phase transformation in superelastic NiTi polycrystalline micro-tubes under tension and torsion - From localization to homogeneous deformation". In: *International Journal of Solids and Structures* 39.13-14, pp. 3797–3809.

Suwas, S. and R. K. Ray (2014). "Representation of Texture". In: *Crystallographic Texture of Materials*. Engineering Materials and Processes. London: Springer London. Chap. 2, p. 260.

Sylwestrowicz, W and E. O. Hall (1951). "The Deformation and Ageing of Mild Steel". In: *Proceedings of the Physical Society of London Section B* 64.381, pp. 747–753.

Wagner, M. F. and W Windl (2008). "Lattice stability , elastic constants and macroscopic moduli of NiTi martensites from first principles". In: *Acta Materialia* 56, pp. 6232–6245.

Wakashima, K. and T. Mori (1972). "Application of continuum dislocation theory to geometry of Lüders front". In: *International Journal of Solids and Structures* 8.8, pp. 1043–1050.

Wollants, P, J. R. Roos, and L Delaey (1993). "Thermally and stress-induced thermoelastic martensitic transformations in the reference frame of equilibrium thermodynamics". In: *Progress in Materials Science* 37, pp. 227–288.

Yu, C., G. Kang, and Q. Kan (2015). "A micromechanical constitutive model for anisotropic cyclic deformation of super-elastic NiTi shape memory alloy single crystals". In: *Journal of the Mechanics and Physics of Solids* 82, pp. 97–136.

Zhang, C., C. Yang, D. Ding, S. Qian, and J. Wu (2005). "Characteristics of Ti-Ni-Pd shape memory alloy thin films". In: *Materials Characterization* 55.4-5, pp. 340–344.

Zheng, L., Y. He, and Z. Moumni (2016). "Effects of Lüders-like bands on NiTi fatigue behaviors". In: *International Journal of Solids and Structures* 83, pp. 28–44.

Zheng, Y., F. Jiang, L. Li, H. Yang, and Y. Liu (2008). "Effect of ageing treatment on the transformation behaviour of Ti–50.9at.% Ni alloy". In: *Acta Materialia* 56.4, pp. 736–745.

Zotov, N., M. Pfund, E. Polatidis, A. F. Mark, and E. J. Mittemeijer (2017). "Change of transformation mechanism during pseudoelastic cycling of NiTi shape memory alloys". In: *Materials Science and Engineering A* 682.September 2016, pp. 178–191.

APPENDIX

A

CRYSTALLOGRAPHIC TEXTURE

Texture in a polycrystalline material is the existence of a preferred orientation of grains. Regarding the degree to which a material is textured, two extreme cases can be acknowledged, as schematically shown in Fig. A.1.

One extreme of this scale is the case of absolute lack of texture, where grains are randomly oriented. Under this circumstance the material is said to have a perfect isotropic behaviour. At the other extremity is the case of single crystals, which are fully oriented in one direction and thus have an anisotropic behaviour. Naturally, polycrystalline engineering materials are not in these extremities, but may rather be weakly, moderately or strongly textured, depending on the percentage of grains exhibiting a preferred orientation.

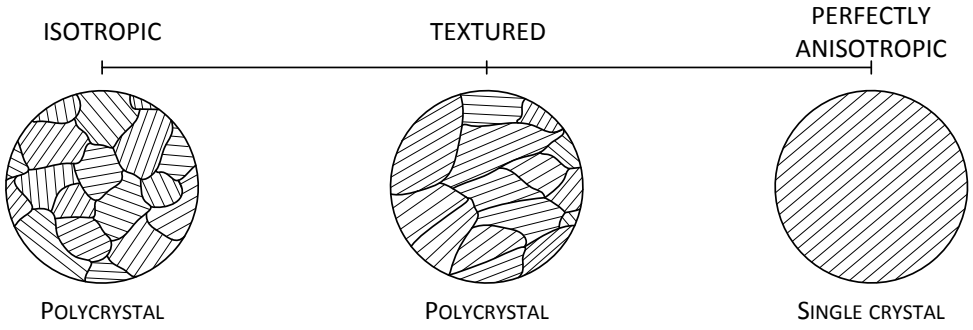

Figure A.1: Extreme cases of grain orientation distribution, from a polycrystalline material with no preferred orientation to a single crystal with its fully oriented structure. Between both lies the textured case.

A.1 Reference frame for texture definition

Because texture represents an orientation it must be related to some reference frame. The adopted reference frame is often that of the sample. This reference frame consists of an orthogonal Cartesian set of axes formed by the three main directions of the sample.

It is called material coordinate system. For rolled materials, these directions are called rolling direction (RD), transversal direction (TD) and normal direction (ND) (see Fig. A.2a). In cylindrical samples, like tubes, these directions can also be called drawing, circumferential and radial directions.

The crystal coordinate system is given in terms of Miller indices. In cubic unit cells these indices are represented by three integer numbers. Planes and directions are represented by (hkl) and $[uvw]$, respectively. To refer to a family of planes which are equivalent to (hkl) by lattice symmetry, the notation $\{hkl\}$ is used. In the same manner, a family of directions which by symmetry are equivalent to $[uvw]$ is denoted $\langle uvw \rangle$.

Texture is defined as the relationship between these two coordinate systems. In this manner, an **unambiguous representation** of texture is achieved by (i) identifying which crystal plane (hkl) is parallel to the rolling plane of the sample and (ii) determining which crystal direction $[uvw]$ is parallel to the sample rolling direction (see Fig. A.2b). Then, a texture is denoted by $\{hkl\}\langle uvw \rangle$ or $(hkl)[uvw]$.

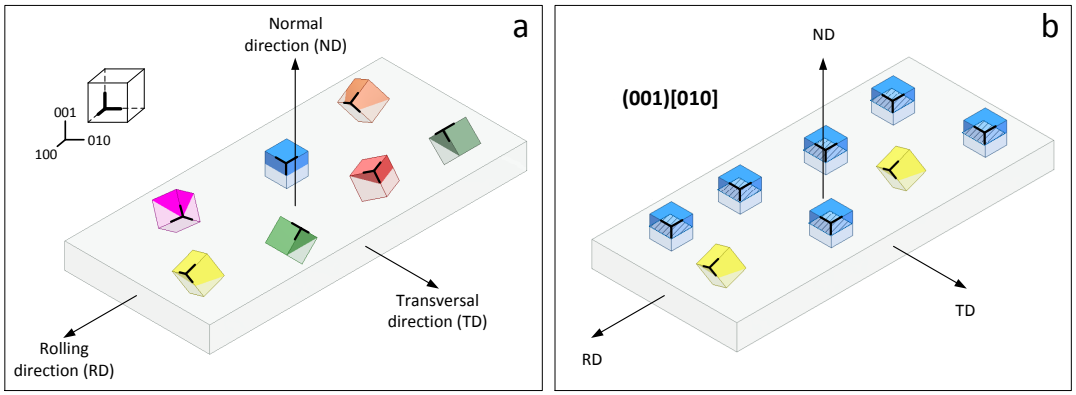

Figure A.2: (a) Orthogonal coordinate system of a rolled sample (reference frame for texture definition) and its crystals (defined by Miller indices). (b) Texture defined by the crystal plane which is parallel to the sample rolling plane, (001) and by the crystal direction which is parallel to sample rolling direction, [010].

A.2 Texture representation

There are two main representations of texture: pole figures and orientation distribution functions (ODF) (Suwas and Ray, 2014).

A.2.1 Texture pole figure

A texture pole figure is a two-dimensional stereographic projection (angle-true) of the crystals in a sample. Figure A.3a illustrates schematically the concept: in the center of a 3D unit sphere is placed a sample of polycrystalline material. The crystal plane normals are projected onto the surface of the unit sphere. Then, one of the hemispheres is projected in a 2D surface. The pole figure consists of this circular projection. In this

illustration the sample of a rolled sheet is placed at the center of the unit sphere. Its pole figure consists in the circular projection sitting on a plane parallel to the sheet rolling plane, where the sample RD, TD an ND are represented as three poles.

If the poles of many crystals are uniformly distributed in the projection, it means that crystals are randomly oriented and thus the material is not textured (Fig. A.3b). While the sample reference frame is fixed, the projection plane can be changed to represent the crystallographic planes of interest. For example, in Fig. A.3c there is a pole figure

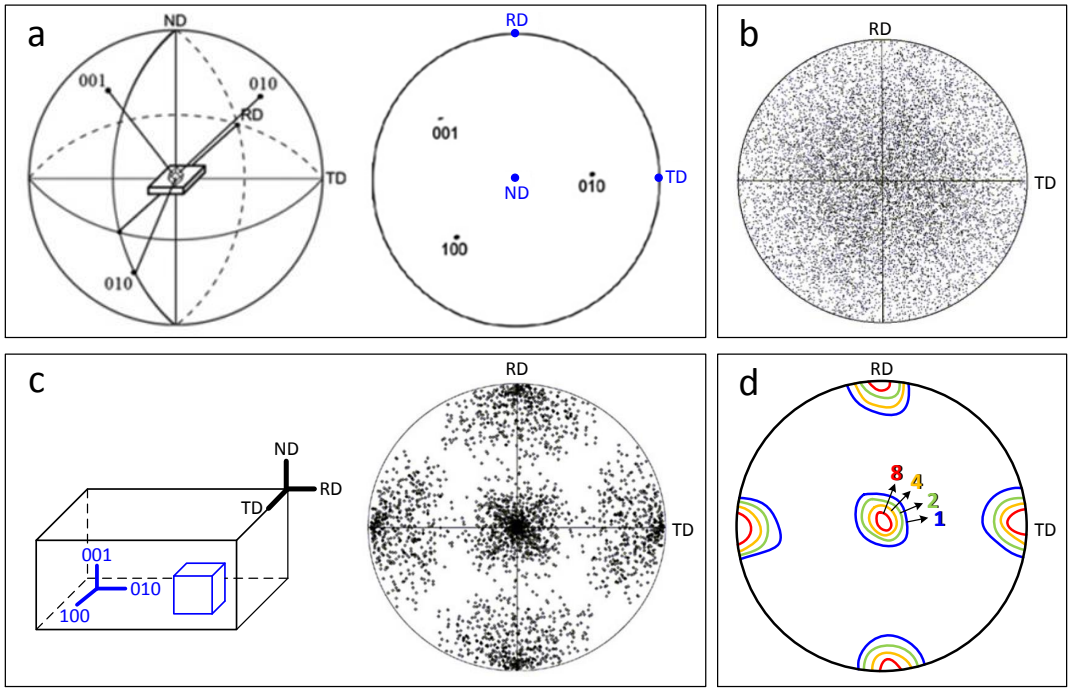

Figure A.3: (a) Stereographic projection of the three main planes of a rolled sample and the three main planes of a cubic crystal inside the sample. (b) Pole figure of a sample with randomly oriented crystals. (c) Poles of {100} oriented cubic crystals projected in a pole figure. (d) Pole figure with contour lines of {100} cubic crystals.

correspondent to the {100} crystallographic planes projected into the sample reference frame. The projections are clustered around some positions, meaning that the material is textured. In the case of Fig. A.3c it can be easily identified that the crystals main directions are aligned with the sample RD, TD and ND and that the denoted texture is $\{100\}\langle 100\rangle$.

It is also common in pole figure representation to use contour lines instead of individual projection points, as in Fig. A.3d. These contour lines represent the **texture index** (T_x). Where $T_x = 0$ no crystal in that particular direction was identified; where $T_x = 1$ the number of crystals in that direction is considered to be random and thus no texture exists in that particular orientation; and where $T_x > 1$ there are enough crystals in that direction to consider the material textured in that particular orientation. The greater T_x is, the more intense is the texture.

Another way of representing texture is to use **inverse pole figures** (IPF), in which the roles of the sample and crystal coordinate systems are inverted. That is, the distri-

bution of the directions of sample planes is drawn in relation to the crystal coordinate system. Figure A.4 shows some example of IPF. Its reading and interpretation is very straightforward and for that reason IPF are very popular.

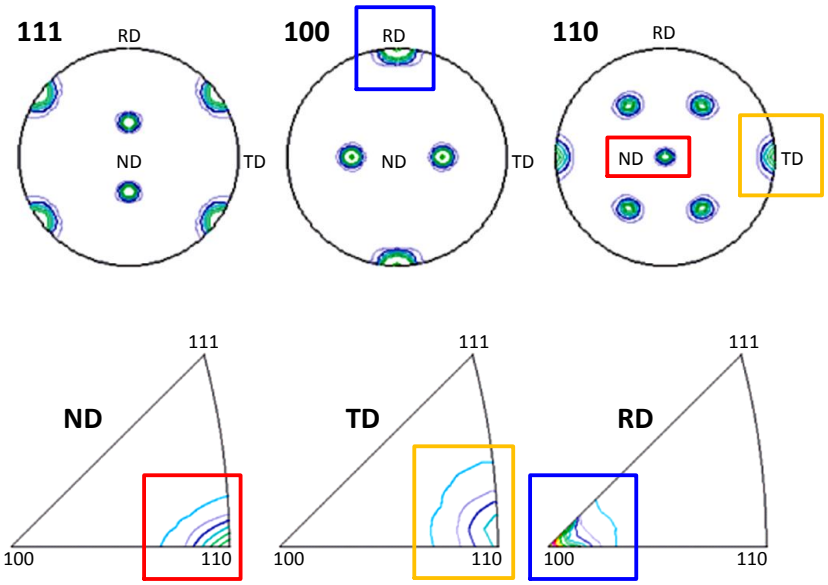

Figure A.4: Correspondent pole figures and inverse pole figures. The coloured rectangles shows the equivalence between the two representations.

A.2.2 Orientation distribution function (ODF)

However, pole figures, and therefore inverse pole figures, are limited representations. This is because only two dimensions can be described in the stereographic projection and thus they do not provide a complete quantitative information. To remedy this, another form of texture representation can be used: an **orientation distribution function** (ODF). According to Suwas and Ray (2014), an ODF "is a mathematical function that describes the frequency of occurrence of particular crystal orientations in a three-dimensional Euler space whose coordinates are defined by three Euler angles".

The Euler space, used to present ODFs, is a cubic volume where each point inside the cube represents a $(hkl)[uvw]$ pair. This space is composed of the Euler angles ϕ, φ_1 and φ_2 varying from 0° to 90°. Figure A.5a shows an example of a complete Euler space and a calculated ODF. However, ODF are generally shown in slices at periodic φ_2 values, as in Fig. A.5b. Also, when confronting textures among different materials, it is often chosen a single φ_2 representative value to perform the comparison.

Moreover, ODFs are calculated from experimental measurements and by means of the evolution of calculation methods, less and less experimental data are necessary to obtain reliable and reproducible ODFs.

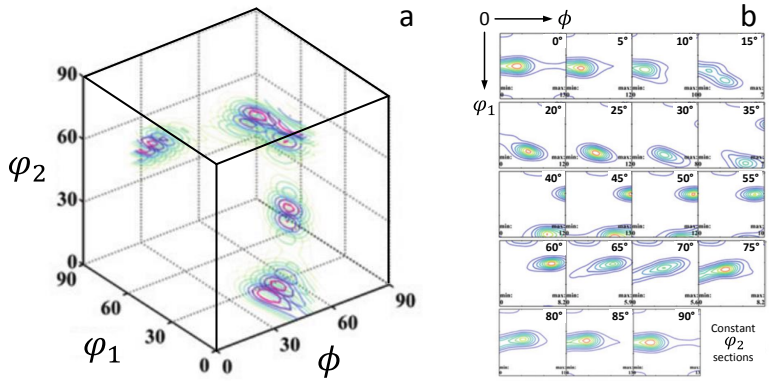

Figure A.5: (a) Euler space showing a calculated ODF. (b) Typical Euler space representation with φ_2 slices at each 5°.

A.3 Techniques for texture measurement

Experimental techniques to obtain crystallographic orientation from a great number of grains are all based on wave diffraction. More specifically, these techniques are based on the theory of Bragg diffraction, which is used to obtain information about periodic structures such as crystallographic planes. Either light (X-ray) or mass (neutron or electron) waves can be used, each one more or less adapted for different conditions.

X-ray diffraction is a relatively cheap technique that allows measurements at ambient conditions or at high/low temperatures and thus it is very popular. However, it is limited to surface analysis, reaching penetration depths of the order 10^{-2} - 10^{-1} mm.

Neutron diffraction also allows to perform measurements under specific ambient conditions with the advantage of having more penetration (10^{1} - 10^{2} mm), giving information about bulk samples. It is a very expensive and more exclusive technique, though, since fewer neutron sources are available in the world.

Electron diffraction is a very reactive technique, performed mainly with Transmission Electron Microscopy (TEM). It requires very thin samples and is useful for accessing the orientation of single crystals, but has little penetration (10^{-3} mm). Also, the Electron Backscatter Diffraction (EBSD) is a technique based on Scanning Electron Microscopy (SEM). This technique provides orientation maps of samples that are very intuitive to read. Figure A.6 shows examples of two common representations of texture obtained from electron diffraction measurements.

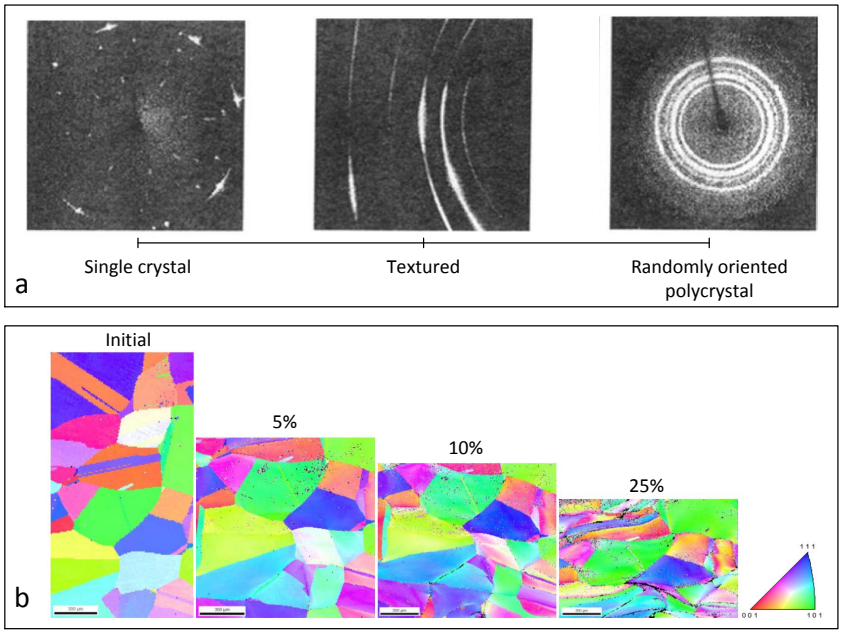

Figure A.6: (a) Examples of different degrees of crystallographic orientation captured by transmission electron microscopy (TEM). (b) Orientation maps obtained with electron backscatter diffraction (EBSD) technique (From Gurao and Suwas, 2013).

APPENDIX

B

STRAIN MAPS OF TESTS AT 40°C AND 50°C

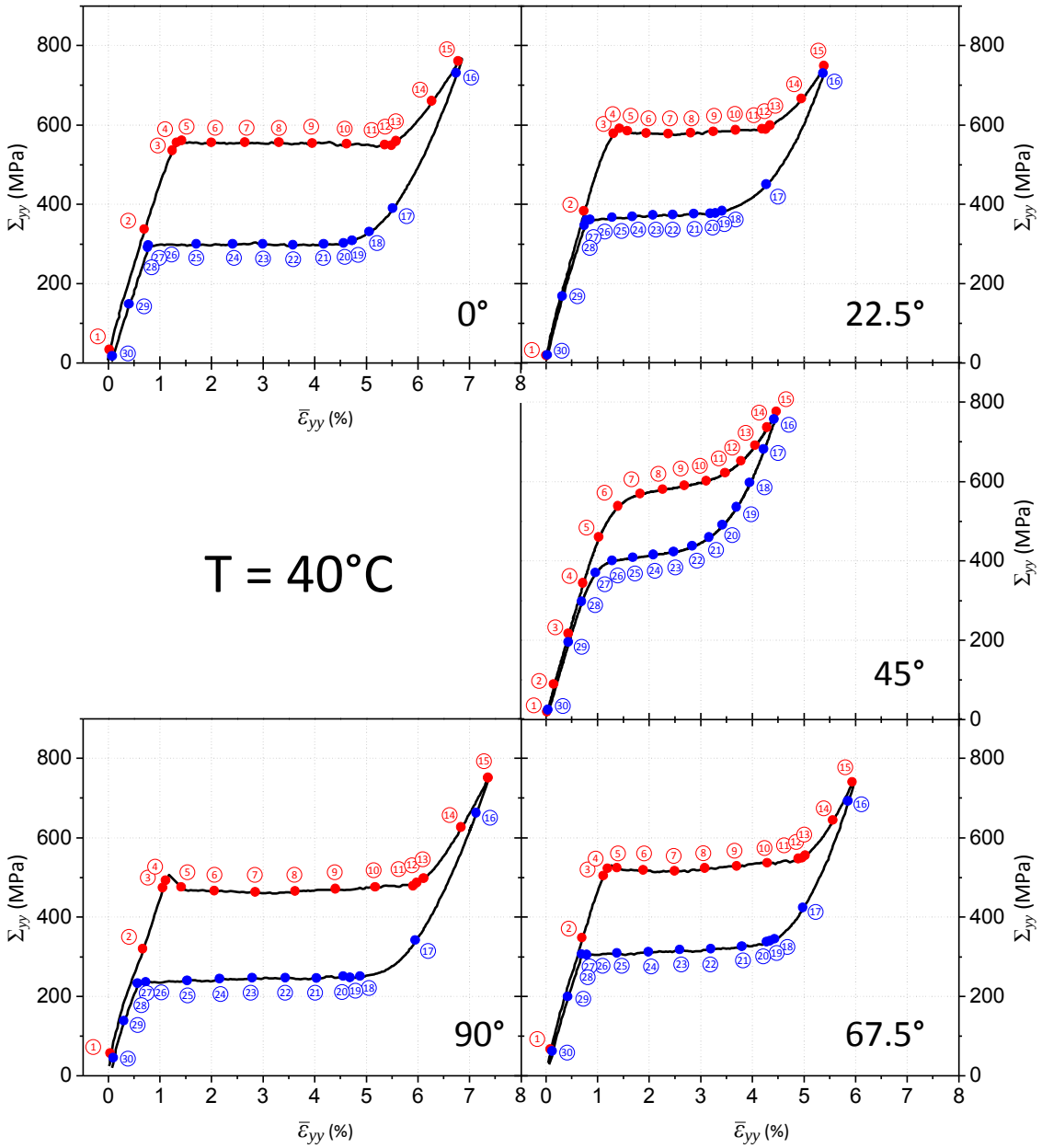

Figure B.1: Nominal tensile stress versus averaged longitudinal strain at 40°C in the five studied directions. Red markers indicate where the strain maps were extracted during loading and blue markers during unloading.

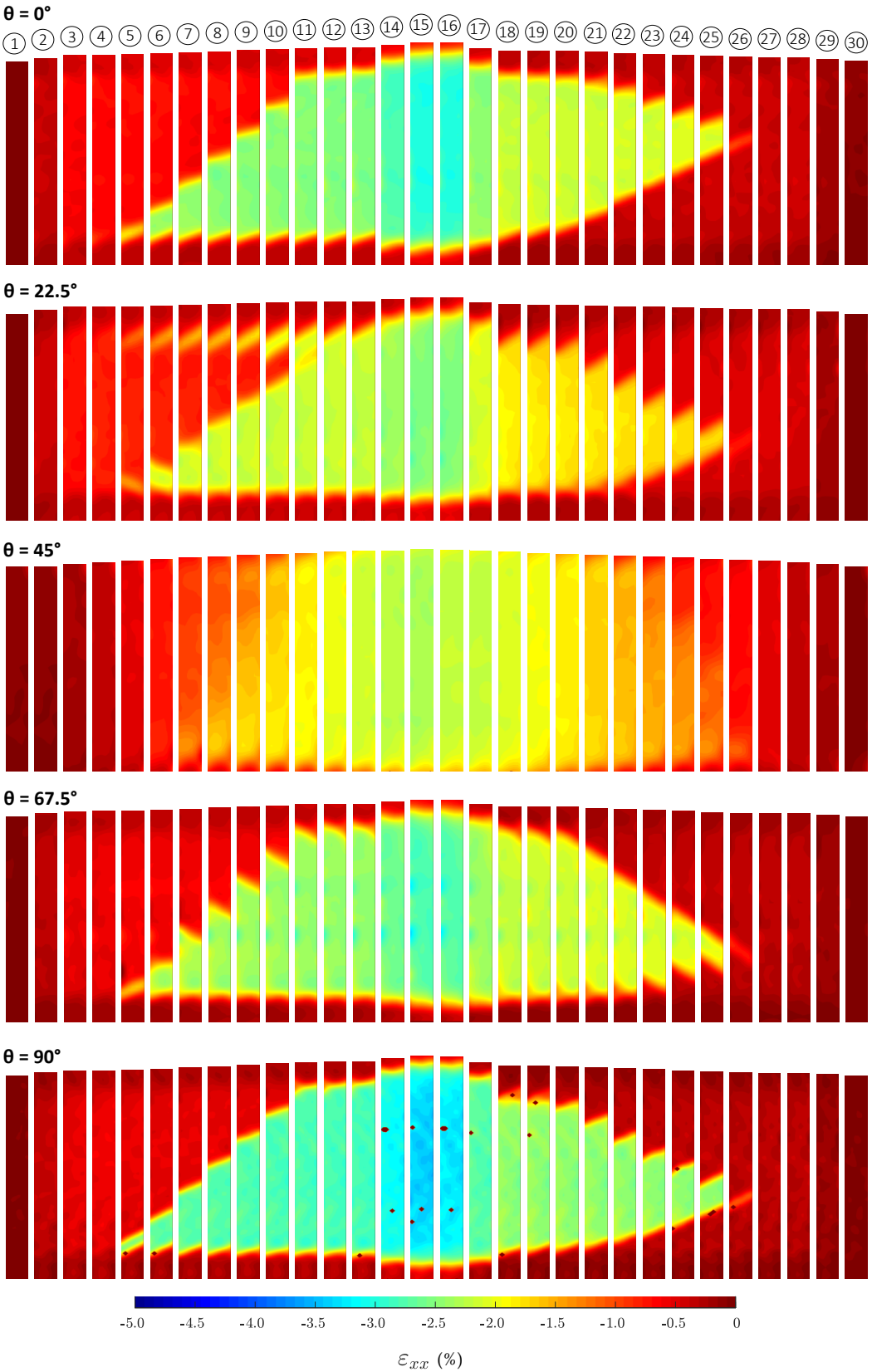

Figure B.2: Transverse strain maps (ε_{xx}) of oriented samples under tensile load at 40°C.

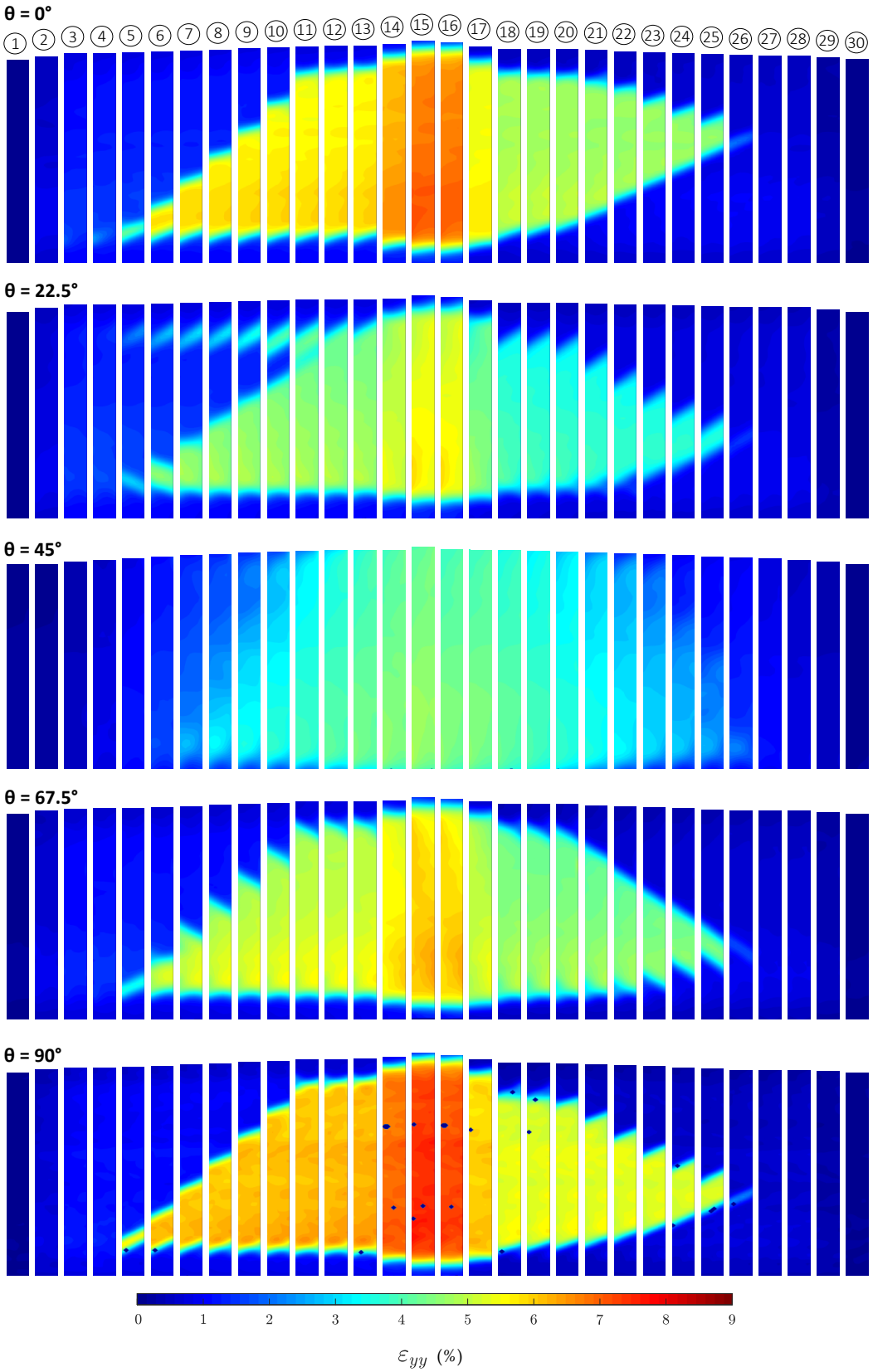

Figure B.3: Longitudinal strain maps (ε_{yy}) of oriented samples under tensile load at 40°C.

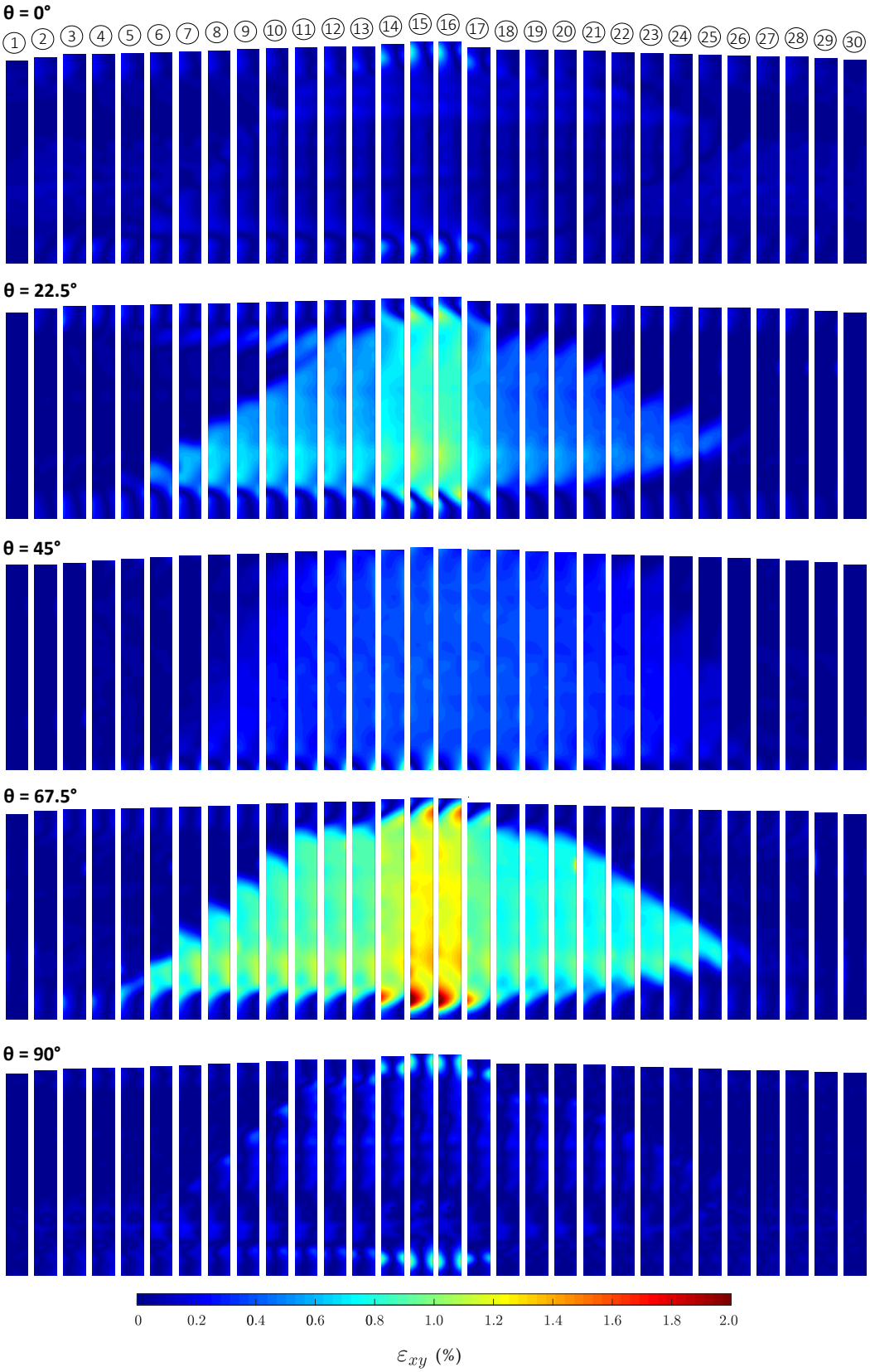

Figure B.4: Shear strain maps (ε_{xy}) of oriented samples under tensile load at 40°C.

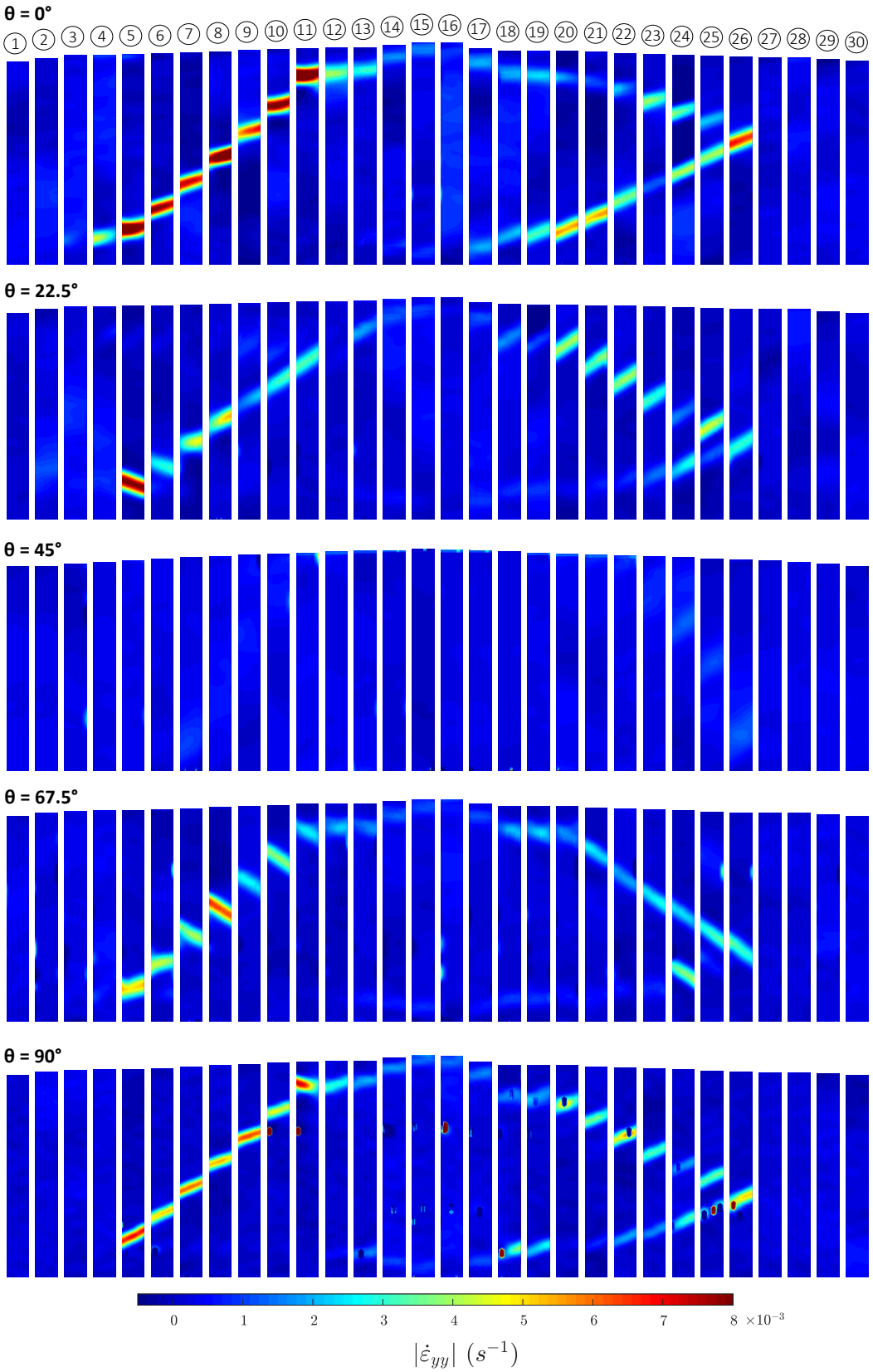

Figure B.5: Longitudinal strain rate maps ($|\dot{\varepsilon}_{yy}|$) of oriented samples under tensile load at 40°C.

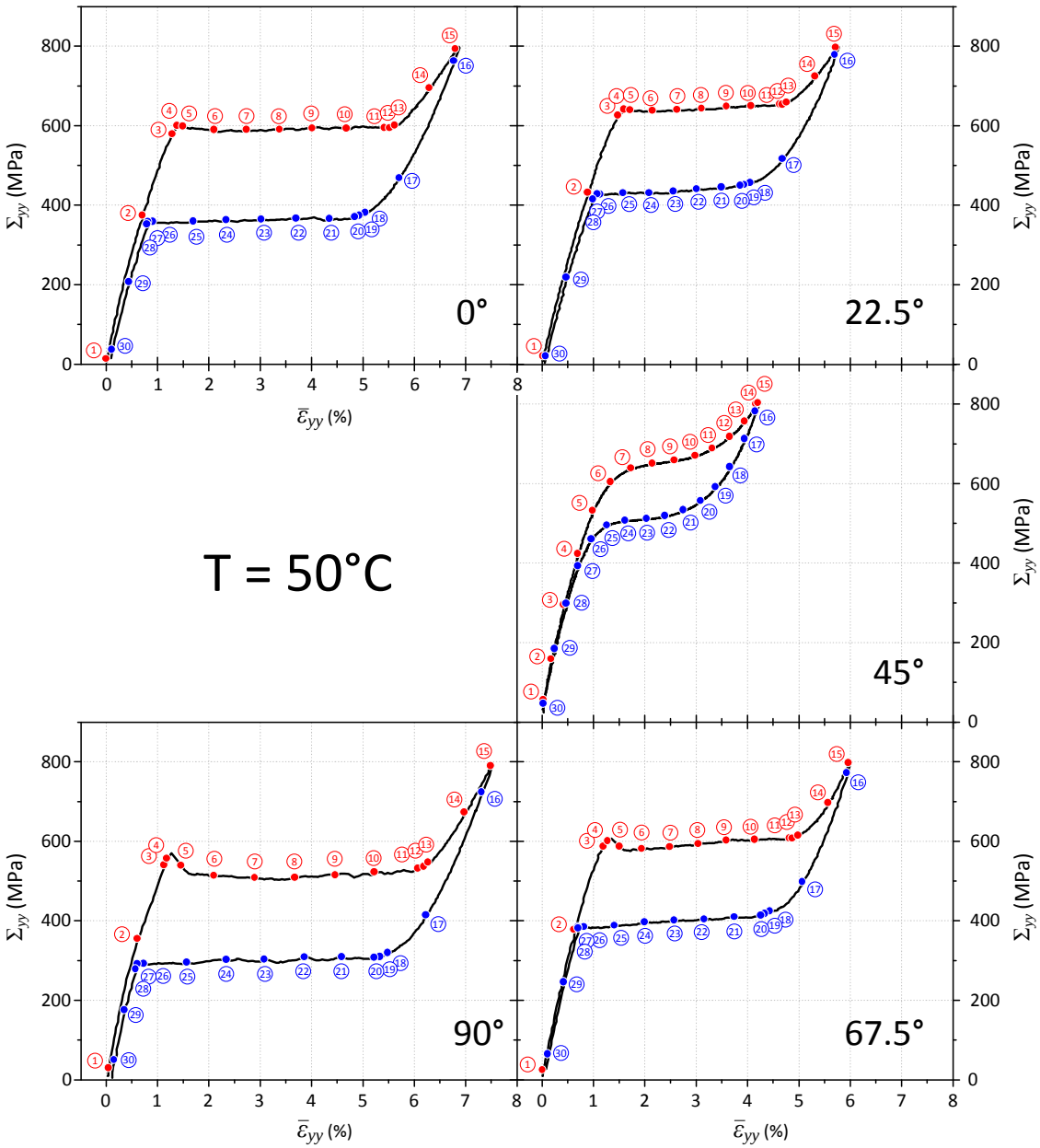

Figure B.6: Nominal tensile stress versus averaged longitudinal strain at 50°C in the five studied directions. Red markers indicate where the strain maps were extracted during loading and blue markers during unloading.

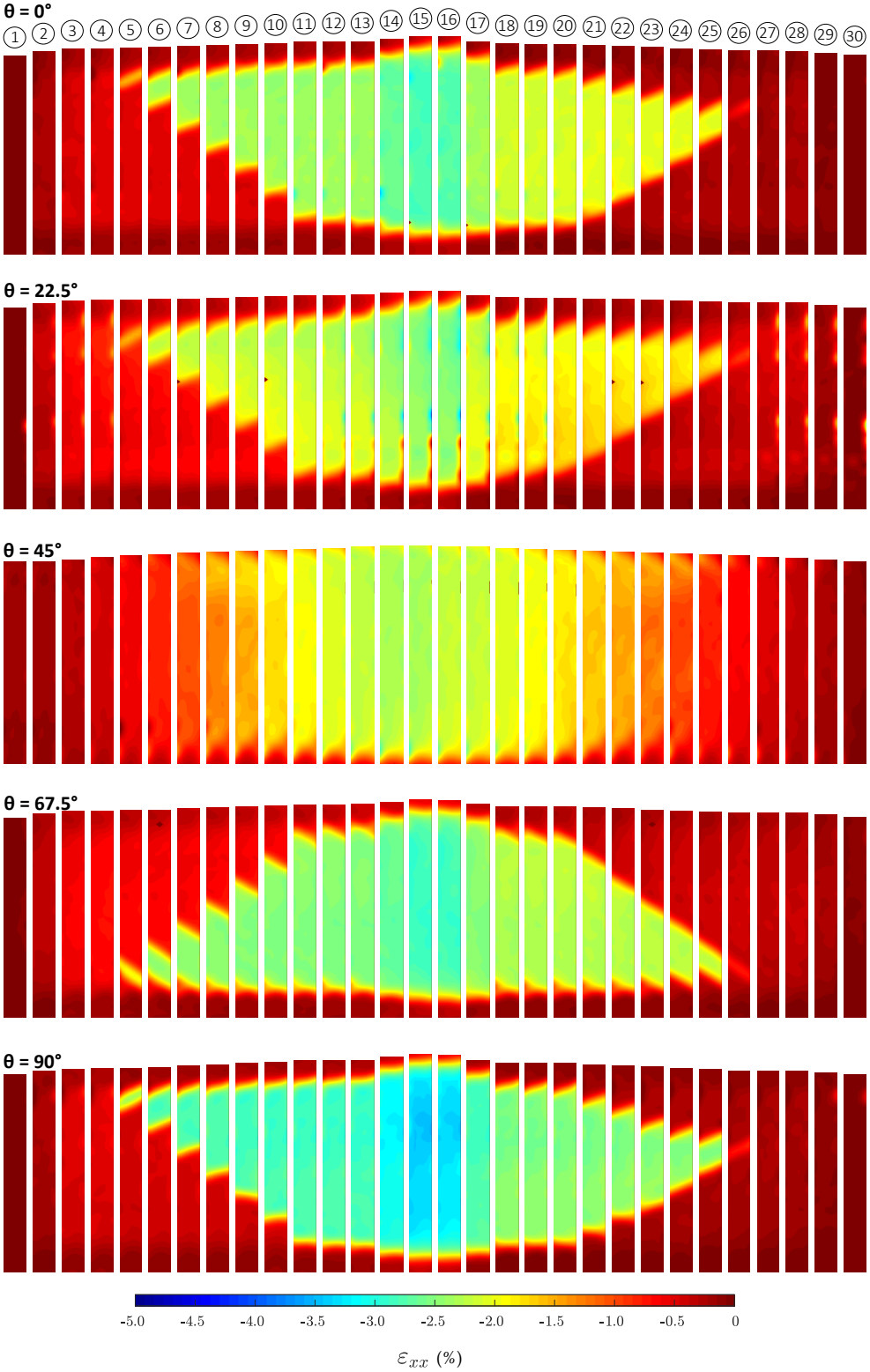

Figure B.7: Transverse strain maps (ε_{xx}) of oriented samples under tensile load at 50°C.

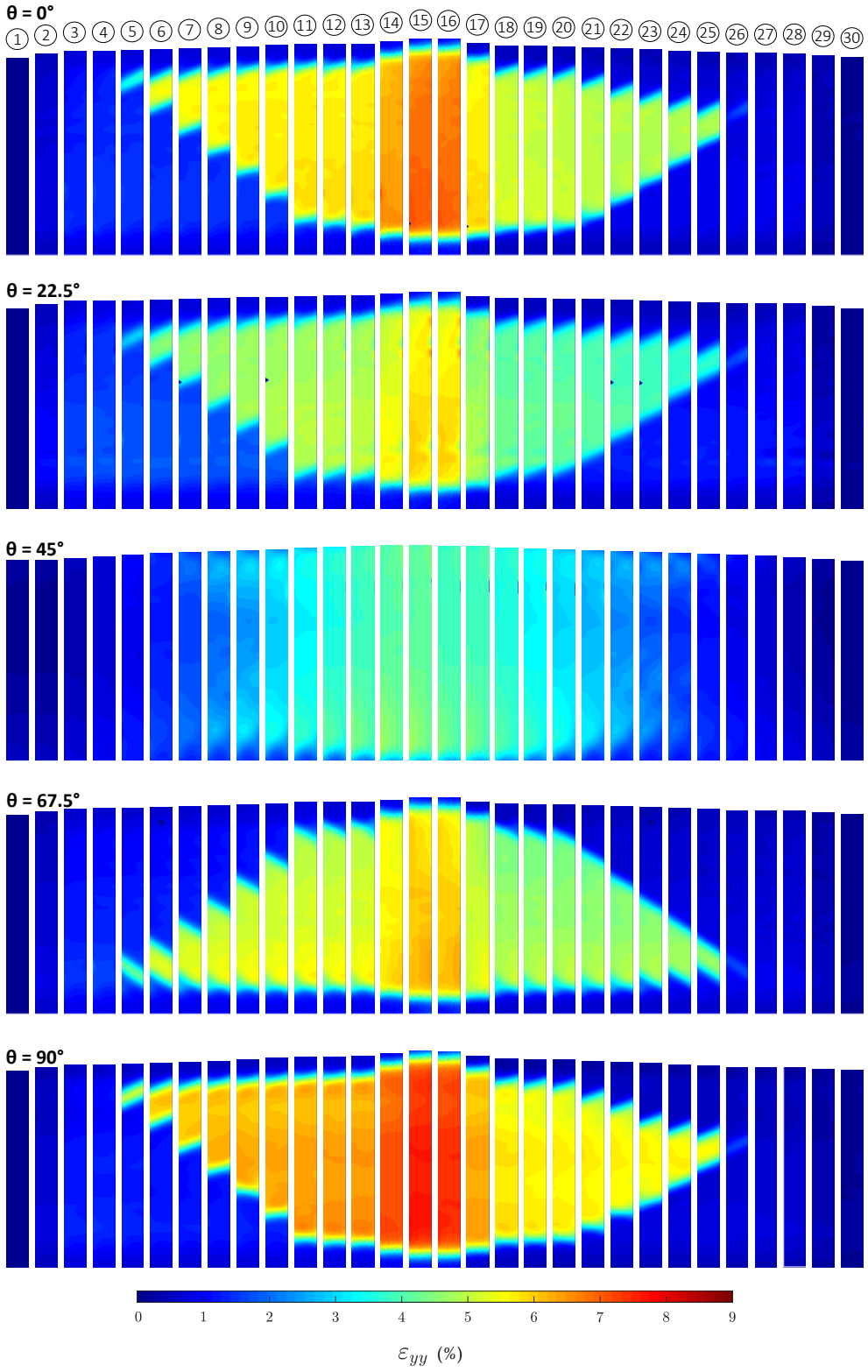

Figure B.8: Longitudinal strain maps (ε_{yy}) of oriented samples under tensile load at 50°C.

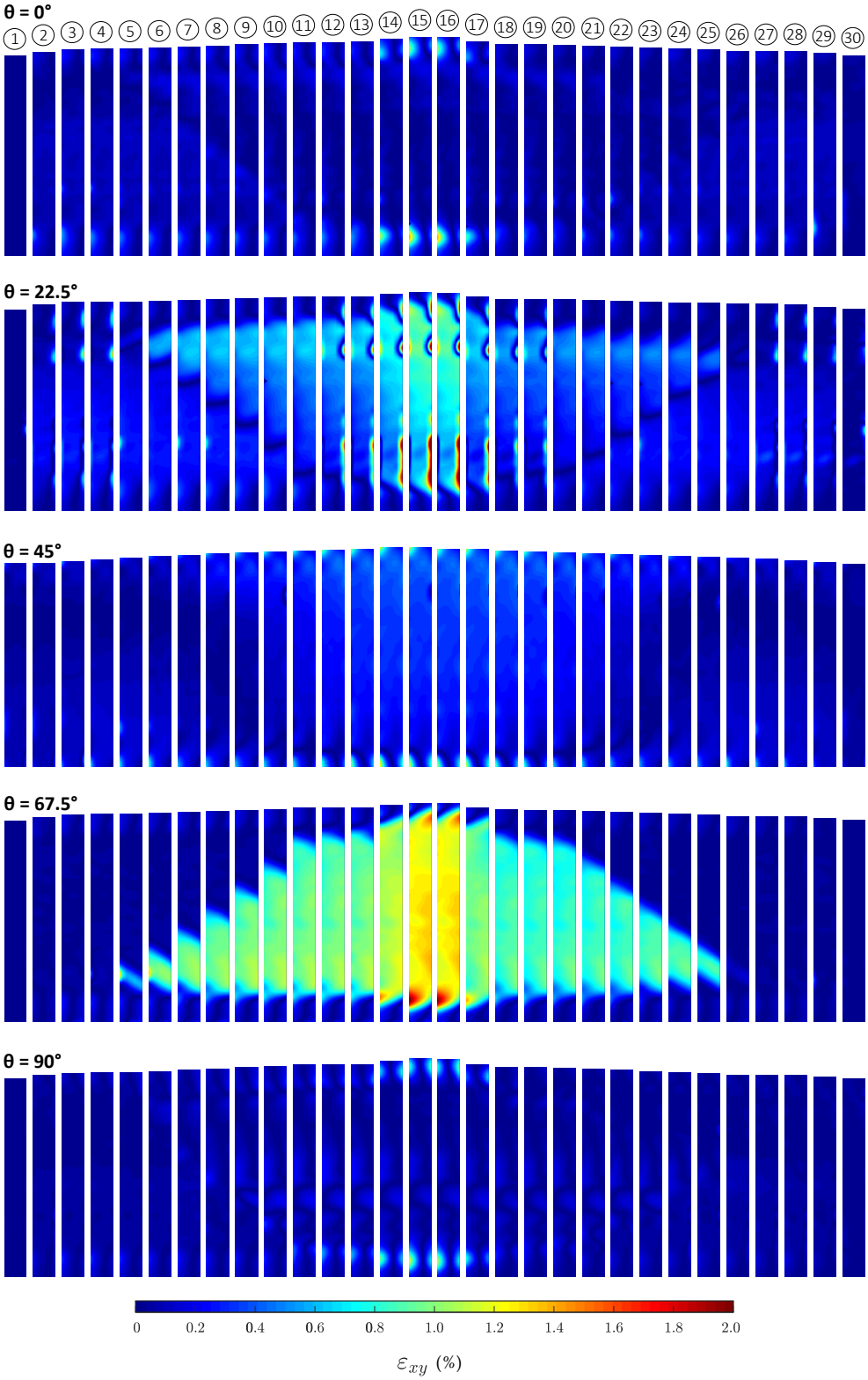

Figure B.9: Shear strain maps (ε_{xy}) of oriented samples under tensile load at 50°C.

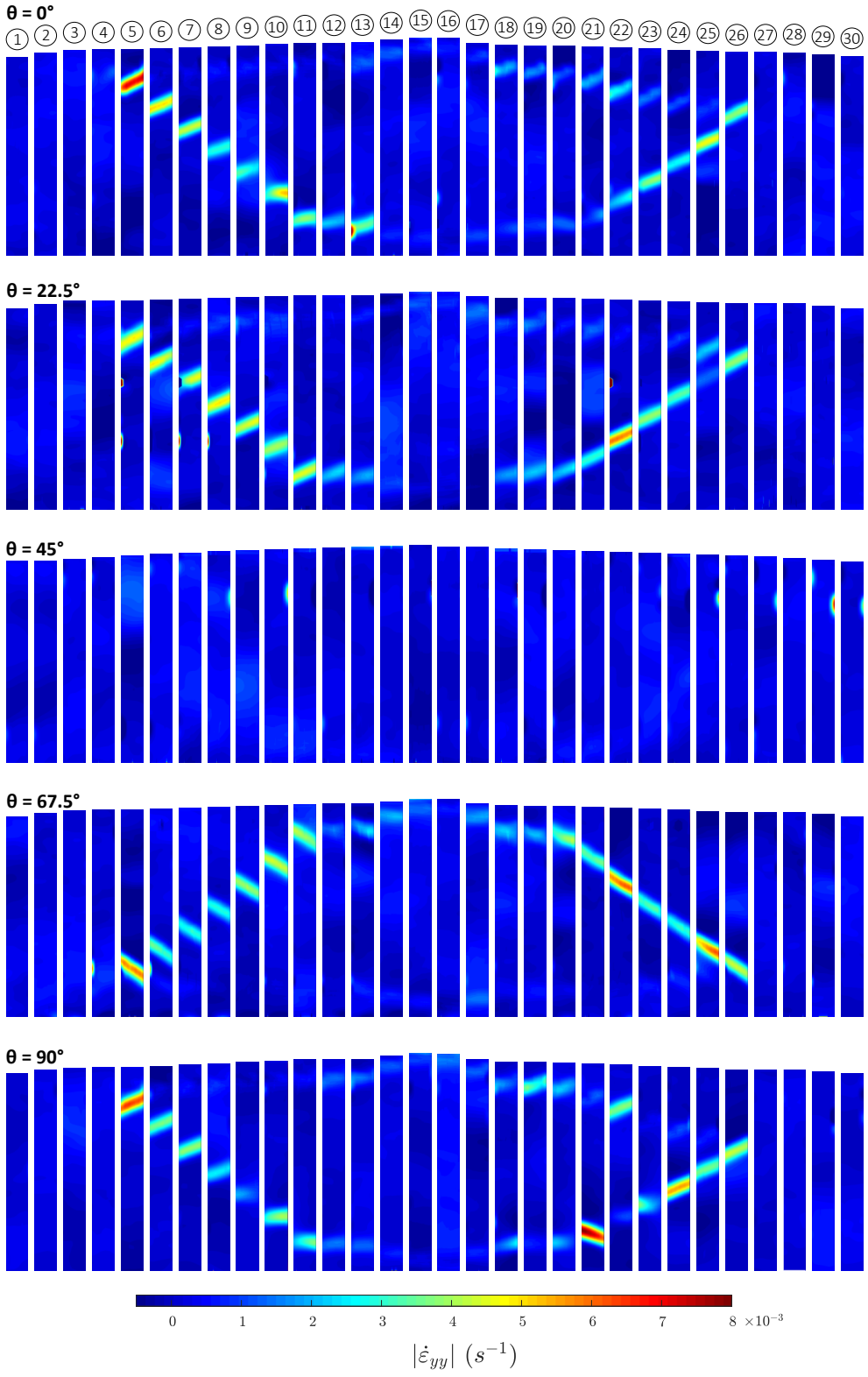

Figure B.10: Longitudinal strain rate maps ($|\dot{\varepsilon}_{yy}|$) of oriented samples under tensile load at 50°C.